Validating Modeled Climate Variations Using Geodetic Monitoring Data

Dissertation

To obtain the academic degree

Doctor rerum naturalium (Dr. rer. nat.)

Submitted to the Department of Earth Science

of Freie Universität Berlin

by

Christof Petrick

Berlin, 2013

1st Reviewer: Prof. Dr. Katja Matthes
2nd Reviewer: Prof. Dr. Maik Thomas

Date of Defence: July 2nd, 2013

Abstract

On the Earth, the atmosphere, ocean, and land interact with each other. For example, an atmospheric pressure system directly influences the Sea Surface Heights (SSHs) in a barometric sense; the associated wind transfers momentum from the atmosphere into the ocean, which alters the ocean currents affecting again the SSHs. The integrated effects of all motion components directly influence the angular momentum of the Earth, while the integrated effect of all mass variations alters the Earth's inertia. Both can excite the Earth Orientation Parameters (EOPs), which are observed very precisely.

In this study, we use the Community Earth System Model (CESM) to simulate mass and motion variations within a coupled climate system. The modeled mass and motion variations of all subcomponents are used to compute the total excitation functions, which then are compared to very precise global EOP observations, provided by the International Earth Rotation and Reference Systems Service (IERS). For further reference, the modeled excitation functions of the subcomponents are compared to operational excitations, provided by the German Research Centre for Geosciences (GFZ). This analysis allows an evaluation of the global model behavior and of the subcomponents. The model output further allows to identify regions of particularly high influence on the excitations as well as regions of especially strong dynamical coupling.

Four CESM experiments were performed, one reference experiment featuring solely natural variations, while the others separate the influence of (I) a coupled ocean component; (II) the quasi-biennial oscillation (QBO) and (III) anthropogenic forcings, e.g. greenhouse gas (GHG) emissions and ozone depleting substances (ODS). The modeled excitation functions are in good agreement with the reference data sets, but reveal an overestimation of the modeled atmospheric mass component in the North Pacific for annual to interannual timescales. This directly translates into an overestimation of the first excitation function χ_1. Analyzing variations among the CESM experiments reveals (I) the complete absence of interannual subtropical tropospheric jet variability when using a climatological ocean; (II) a significantly increased atmospheric mass variation in the arctic region in the absence of a QBO; and (III) hardly any modeled effect of the global dynamics with respect to anthropogenic forcings.

Finally, the North Pacific - a region with particularly strong atmosphere-ocean coupling - is investigated and the findings supporting the hypothesis of wind driven ocean mass variations. The identified significant wind patterns explain the modeled ocean mass variations and can be directly projected onto ERA-Interim data in order to estimate the independent GRACE observations. The here presented relation between the ERA-Interim winds and the GRACE gravity field observations supporting the following two conclusions: First ERA-Interim winds can be used to further refine GRACE observations. Secondly, GRACE observations can be used, for example by means of assimilation, in order to improve atmospheric models.

Kurzfassung

Die Atmosphäre, der Ozean und das Land sind durch hochdynamische Prozesse miteinander verbunden. Wie in einem Goethe-Barometer beeinflusst beispielsweise der Atmosphärendruck auch die Ozeanwassersäule. Darüber hinaus beeinflussen die atmosphärischen Winde die Ozeanströmung und transportieren verdunstete Wassermassen, die beispielsweise über Land abregnen. Die Summe aller dynamischen Effekte (Winde und Strömungen) beeinflusst den globalen Drehimpuls, während die Summe aller Massenverlagerungen die Massenträgheit der Erde beeinflusst. Veränderungen im Drehimpuls oder Trägheitstensor regen die Erdorientierungsparamter an.

In dieser Studie werden Massen- und Bewegungsveränderungen im gekoppelten Erdsystem für die Atmosphäre, den Ozean sowie für die Kontinentale Hydrologie simuliert und validiert. Hierfür werden die Ergebnisse aus dem gekoppelten Erdsystemmodell CESM (Community Earth System Model) mit geodätischen Beobachtungen der Erdrotation verglichen, welche vom International Earth Rotation and Reference Systems Service (IERS) zur Verfügung gestellt werden. Des Weiteren werden die modellierten Anregungen der einzelnen Komponenten (Atmosphäre, Ozean, Land) mit den vom Deutschen GeoforschungsZentrum (GFZ) zur Verfügung gestellten Anregungen verglichen. Gemeinsam kann so neben der globalen Analyse auch ein Gütemaß der integralen Eigenschaften, der modellierten Subkomponenten, abgeschätzt werden. Eine weitere Analyse der modellierten Daten identifiziert die besonders einflussreichen Regionen sowie Bereiche besonders starker Kopplung.

Zur Analyse der modellierten Klimavariation wurden vier CESM Experimente durchgeführt. Das Referenzexperiment berücksichtigt ausschließlich natürliche Variationen. Ein weiteres wird ohne gekoppelten Ozean angetrieben. Das dritte Experiment wird ohne korrigierte QBO (Quasi Biennial Oscillation) Winde simuliert, während beim vierten Experiment anthropogene Einflüsse wie Treibhausgase und ozonzerstörende Substanzen berücksichtigt werden. Grundsätzlich stimmen die modellierten Anregungsfunktionen mit den Beobachtungen und den operationellen Daten überein. Unterschiede finden sich vor allem im Jahresgang der modellierten Atmosphärenmassenkomponente im Nord Pazifik, welche sich direkt in eine Überschätzung der ersten Anregungsfunktion überträgt. Der Vergleich der vier CESM Experimente zeigt:ohne Berücksichtigung einer realistischen Ozeankomponente lassen sich keine vernünftigen Aussagen über die interannualen Variationen der zonalen Winde treffen. Außerdem beeinflusst die QBO das Bodendrucksignal in der Arktis. Des Weiteren zeigt sich kein signifikanter anthropogener Effekt auf die globalen Anregungsfunktionen.

Die detaillierte Analyse der Atmosphären-Ozean Kopplung im Nordpazifik bestätigt die Hypothese von windgetriebenen Ozean-Massenvariationen auf Modellebene. Die Projektion

der modellierten Ergebnisse auf ERA-Interim Daten ermöglicht eine Abschätzung der unabhängig von GRACE beobachteten Massenvariationen. Dieser hier gezeigte Zusammenhang zwischen Schwerefeldbeobachtungen und den atmosphärischen Winden veranschaulicht den gegenseitigen Nutzen beider Datensätze füreinander: GRACE-Beobachtungen können unter Berücksichtigung der Reanalyse-Windfelder weiter verbessert werden. Außerdem können GRACE-Daten in Atmosphärenmodelle assimiliert werden.

Contents

Chapter 1

Introduction

The Earth as we experience it, is highly dynamic in every possible aspect. From early childhood on we see the wind chasing huge clouds and we find little children blowing out candles. We see water piling in the bathtub, reacting to the slightest motion and we see enormous rivers entering the ocean. We find the sun drying our throat and scorching the countryside. As a child we observe the Earth trying to understand and link the little pieces within our reach and imagination; we as these little children have grown in understanding and comprehension.

We now can see the Earth separated into atmosphere and ocean; we observe ice sheets and the Earth's interior; we measure and collect any information all to meet the ultimate goal of trying to understand action and reaction. In the context of climate research, the associated spatial scale ranges from regional to global while the temporal scale stretches from days to centuries.

In order to understand the geophysical processes acting on and within the Earth, it is essential to understand the mass transport within the whole Earth system. The total weight of the Earth is approximated with 6×10^{24} kg (Groten, 2004); most of this mass is related to the Earth interior consisting of core, mantle and crust. Within a human lifetime the mass variations of the Earth's interior are rather small. In contrast, the variations within the atmosphere and hydrosphere are more vivid. The total mass of the global hydrosphere is about 3 orders of magnitude smaller and approximated with 1.4×10^{21} kg (Yoder, 1995). Another three orders of magnitude smaller we find the atmosphere with a total mass of about 5.1×10^{18} kg (Trenberth and Guillemot, 1994). Despite these relatively small shares, the atmosphere and hydrosphere are essential for the description of the global mass transport on all timescales. This work will focus solely on processes that describe mass transport within the atmosphere and hydrosphere, while long term processes related to mass variations of the Earth's interior are not considered.

In order to describe the Earth system, geodetic observations are crucial. There are three major branches of geodetic monitoring data: one describes the Earth geometry, e.g. the Sea Surface Height (SSH) or continental uplift; the second one describes the Earth gravity field,

e.g. the geoid; and the third one describes the Earth rotation, e.g. length of day or polar motion. Essentially all geodetic measurements observe the same Earth, meaning the very same geophysical processes, solely the perspective changes. For example an atmospheric high pressure system is inverse barometrically compensated over the ocean (Wunsch and Stammer, 1997) leaving the total mass of this region and thus the geoid equal for spaceborne observations as performed by the Gravity Recovery Climate Experiment (GRACE[1]). However, the associated geometry (SSH) changes, which can be observed by satellite altimetry missions such as TOPEX/POSEIDON (T/P[2]). In general, all mass variations alter besides the geoid, also the inertia of the Earth, which then affects the Earth rotation. However, the Earth rotation additionally depends on the relative angular momentum (Munk and MacDonald, 1960; Moritz and Mueller, 1988), meaning the integrated effect of atmospheric winds and oceanic currents. In the last decades, satellite measurements offered a new quality of geodetic observations with unprecedented accuracy and global coverage (e.g. GRACE, T/P). These precise geodetic observations rendered significant mass transport within and across all subsystems featuring, for example, small variations of the geoid on a large spatial scale (Tapley et al., 2004a; Sasgen et al., 2010). The combined analysis of simultaneous geodetic measurements allows the computation of unobserved variables (e.g. steric sea level variations, Lombard et al. (2007)), and consequently the separation of the underlying processes (e.g. thermal expansion versus eustatic sea level rise).

However, these analyses are limited, as are the geodetic observations. This is true in terms of spatial and temporal resolution as well as regarding the observable variables themselves. Here, the second essential key for describing the Earth system comes into play: the modeling and simulation of geophysical processes. Historically, different scientific communities developed and maintained stand-alone models describing for example the atmosphere, the ocean, the cryosphere, the continental hydrosphere or the Earth's interior (Edwards, 2011). However, as indicated above, observations show that theses subsystems communicate and interact with each other meaning momentum, mass and energy are transferred between all subsystems. Consequently, all analyses solely based on stand-alone models are limited because geodetic observations naturally represent a realistic coupling. This highlighted the need for consistently coupled models, preserving mass, energy and momentum. The current state of modeling science offers consistently coupled climate models including the atmosphere, the ocean, the cryosphere and continental hydrosphere (Taylor et al., 2009, 2012). However, processes of the Earth's interior, which are particularly important on decadal and longer timescales, are not yet included in most of the coupled climate models.

[1] http://www.gfz-potsdam.de/grace
[2] https://sealevel.jpl.nasa.gov/missions/

A significant benefit of all modeling studies is that they are not limited to one realization but offer the possibility of performing sensitivity studies. In this context, basically all modeled parameters can be altered or fixed in order to investigate the sensitivity of the modeled Earth system to this specific parameter. This has been done in order to quantify the influence of, for example, natural variations (Matthes et al., 2010) as well as anthropogenic ones (Meehl et al., 2012).

Improvements on either the modeling or observational side will lead to improvements of the complementary component. For example modeling a more realistic ocean improves the observed geoid (Chambers and Bonin, 2012). A more precise geoid allows the validation of the modeled mass transport (Werth, 2010) and consequently an improvement of the associated model (Sasgen et al., 2012; Rau and Rogozhina, 2013). The potential of observed Earth rotation data constraining and evaluating atmospheric models is investigated by Neef and Matthes (2012). The remaining deficiencies identified between modeling and observation help interpreting the generated data and the associated errors. All the above mentioned examples of the beneficial symbiosis between geodetic monitoring data and the modeling community are examples of stand-alone models. As of now, the validation of coupled climate models upon geodetic monitoring data is sparse, which is partly due to the novelty of coupled climate models.

Regarding the Earth rotation, Schuh et al. (2003) identified six major scientific goals for the Earth rotation community, including the investigation of: a) the Earth rotation in a consistently coupled model; b) the Earth rotation as an indicator for climate variability; c) possible contributions of observed Earth rotation data to a global geodetic observation system. Despite the publication of these goals already a decade ago, a) remains unanswered, while b) and c) leave plenty of room for more sophisticated discussions. The work at hand will contribute to all three goals by analyzing the excitation of a consistently coupled climate model and comparing it to the observed Earth rotation. Further, the question whether and if so, to what extent the Earth rotation allows a consistent validation of the integrated behavior of the coupled climate model and its subcomponents is discussed. In this context, coupled climate models help to understand the interaction between all subsystems, especially between the atmosphere, the ocean and the continental hydrosphere. This opens the question whether geodetic observations in combination with coupled climate models allow the identification of regions of particularly strong coupling.

An extensive analysis of the capability of geodetic measurements to describe the global mass transport was carried out in the framework of the priority program SPP 1257 "Mass distribution and Mass Transport in the Earth System" (Ilk et al., 2005; Kusche et al., 2012), which was established by the German Research Association DFG. The herein facilitated geodetic observations include gravity (e.g. geoid) and geometry (e.g. SSH). Earth rotation was consid-

ered as neighboring field and thus not part of the main focus. In general, the project focused on mass transport related to ocean dynamics, ice mass and processes of the Earth's interior. The authors explicitly do not expect gravity field observations being able to improve atmospheric or climatological models. The work presented here analyzes observed Earth orientation data in concert with observed gravity variations and various experiments of a coupled climate model. The question arises whether this combination allows to identify potential improvements based on e.g. gravity field observations, for atmospheric or climatological models. In the context of climate modeling the question arises, whether it is possible to separate natural from anthropogenic variations, which then can be attributed to specific geodetic observations.

In order to answer the above raised questions, a set of four climate system experiments is performed under varying boundary conditions, using the Community Earth System Model (CESM), which includes interactively coupled components for the atmosphere, ocean, continental hydrosphere and sea ice. A reference experiment features only natural variations; a second one includes anthropogenic variations; the third is modeled without an interactive ocean; and the last one without a quasi-biennial oscillation (QBO).

Subsequently, the variations of the angular momentum budget is investigated for all experiments and all subsystems separately and compared to geodetic the observed parameters. Analyzing the spatial patterns that excite variations in the angular momentum leads to coupled phenomena that are for example triggered in the atmosphere and then propagate into the ocean. A very prominently modeled example of atmosphere-ocean interaction is validated upon GRACE observations and ERA-Interim reanalysis data.

The work is structured as follows: Chapter 2 discusses theoretical aspects of the Earth rotation and atmosphere-ocean interactions. Additionally, the used data and all applied methods for analyzing our results are described. Chapter 3 describes the applied models and experiments. Chapter 4 consists of a prestudy discussing the general need of coupled climate models. Annual and interannual variations of the modeled angular momentum budget are presented and compared to observations in Chapter 5. Oceanic mass variations triggered by the prevailing surface winds in the North Pacific are discussed in Chapter 6. The last chapter summarizes and discusses all results and additionally provides an outlook.

Chapter 2

Theory, Data and Processing

2.1 The Rotation of the Earth

2.1.1 Introduction

Empirically, the Earth is rotating constantly around its rotation axis towards the East, where the sun rises. If observed from the North Star Polaris, the rotation is counter clockwise. However, in the presence of highly precise geodetic measurements, the Earth rotation is observed to be variable in terms of rotation speed and also regarding the orientation of the rotation axis. This is basically related to two sources: (1) external and (2) internal ones.

External factors acting on the Earth's total momentum can either be related to an impact of an external body, or to gravitational attraction of other bodies, such as the Sun, the Moon, other planets and basically any object that moves relative to an Earth fixed reference frame. External torques, especially related to the lunisolar effects cause the Earth to precess and nutate. In the following all external factors will not be discussed and thus are set to zero.

Reducing all external factors, the total angular momentum of the Earth stays constant. This, however, does not mean that the Earth rotation stays constant. The reverse is true. The Earth rotation is highly dynamic, which is mainly related to momentum transfer between the solid Earth and all fluidal components, such as the atmosphere, ocean and continental hydrosphere. The fluidal system of the Earth can alter the solid Earth rotation in two ways: (1) dynamical effects (e.g., changes in the wind field); and (2) mass variation (e.g., atmospheric mass, such as a high pressure system, moving on the Earth surface). The first one directly affects the angular momentum, which is proportional to the velocity for a certain distance to the rotational axis. Thus variations in the wind speed change the angular momentum budget of the atmosphere, which is then compensated by the other components in favor of conservation of the total angular momentum. The second effect (mass variations) alters the Earth's tensor of inertia. For example, moving mass from the pole towards the equator, increases the Earth's

moment of inertia, slowing its rotation, which lengthens the day. Consequently any dynamical process on the Earth influences its rotational vector. However, one can only observe the integrated effects of all dynamical processes. Some of these internal effects excite the Earth in such a way that it starts to wobble at discrete frequencies. In general natural frequencies depend solely on the inner structure and condition of the investigated body, which in this case means on the highly complex internal structure of the Earth itself. Most prominent among the natural or free wobbles is the Chandler wobble with a frequency of about 433 days.

The following subsections summarize the key steps of deriving the linearized Earth rotational excitation functions starting form the Eulerian equation of motion. The here presented derivative follows the approach of Gross (2007), who summarized the work of Smith and Dahlen (1981) and Wahr (1982, 1983). Other approaches are given for example by Barnes et al. (1983) or Eubanks (1993).

2.1.2 Theory

Euler's second law defines the temporal derivative of the angular momentum $L(t)$ of any rotating body equal to the sum of all externally applied torques $\tau(t)$. From the point of view of this rotating object with respect to inertial space the Eulerian equations of motion is defined as (Munk and MacDonald, 1960; Lambeck, 1980; Moritz and Mueller, 1988)

$$\frac{\partial L(t)}{\partial t} + \omega(t) \times L(t) = \tau(t), \tag{2.1}$$

where $\omega(t)$ is the angular velocity of the rotating body. As described in the introduction, variations in the total angular momentum result either from variations in the mass distribution, which alter the tensor of inertia $I(t)$ or can be related to relative motion $h(t)$ within the rotating frame. The total angular momentum is defined as $L(t) = h(t) + I(t)\omega(t)$ and can be substituted into equation 2.1, giving the Liouville equation

$$\frac{\partial}{\partial t}[h(t) + I(t)] + \omega(t) \times [h(t) + I(t)] = \tau(t). \tag{2.2}$$

Considering this rotating body to be a rigid Earth leaves the atmosphere, ocean and continental hydrosphere as the influential factors for variations of the total inertia or relative angular momentum. Regarding the whole Earth, the perturbing effects are very small and can be linearized. Variations in the mass distribution of the Earth alter the moment of inertia according to

$$I(t) = \underbrace{\begin{bmatrix} A & 0 & 0 \\ 0 & B & 0 \\ 0 & 0 & C \end{bmatrix}}_{\text{unperturbed inertia}} + \underbrace{\begin{bmatrix} \Delta I_{xx}(t) & \Delta I_{xy}(t) & \Delta I_{xz}(t) \\ \Delta I_{yx}(t) & \Delta I_{yy}(t) & \Delta I_{yz}(t) \\ \Delta I_{zx}(t) & \Delta I_{zy}(t) & \Delta I_{zz}(t) \end{bmatrix}}_{\text{perturbation}}, \tag{2.3}$$

where the first part of the matrix denotes the initial state, with A, B and C being the main principal components of the Earth's inertia. The second part represents the perturbations of the total inertia, which is related to mass transport, e.g. variations in the atmospheric pressure; ocean bottom pressure; or continental water storage. All mass variations have an effect on the Earth inertia and with it on the orientation of the rotation axis. The linearized description of the perturbed rotation axis is:

$$\omega(t) = \underbrace{\Omega \begin{bmatrix} 0 \\ 0 \\ 1 \end{bmatrix}}_{\text{rotation axis}} + \underbrace{\Omega \begin{bmatrix} m_x(t) \\ m_y(t) \\ m_z(t) \end{bmatrix}}_{\text{perturbation}} . \tag{2.4}$$

The first part again represents the unperturbed rotation Ω around the $\hat{z}$ axis. The second part denotes the anomalous rotation, where $m_x(t)$ and $m_y(t)$ represent deviations of the rotating pole within the rotating (terrestrial) reference frame, which is also known as polar motion. The $m_z(t)$ component represents variations in the rotating speed itself.

Inserting equations 2.3 and 2.4 into the Liouville equation 2.2 yields coupled differential equations for the polar motion terms and a separated one for the third component. The system of equations relaxes substantially by assuming: (1) mass displacements and the related momentum of inertia variations are small compared to the total rotating inertia ($\Delta I_{ij}(t) \ll C$); (2) the motion components and the related relative angular momentum is small compared to rotating inertia times the angular velocity of the Earth ($h_i(t) \ll \Omega C$); (3) variations in the rotating axis are small compared to the initial rotation ($m_i(t) \ll 1$); (4) the Earth is an axisymmetric body, meaning that the first two principal moments of inertia are equal ($A' = (A + B)/2$); and (5) external torques related to e.g. precession and nutation are neglected ($\tau = 0$). Considering now solely first order terms leads to the following differential equations:

$$\frac{A'}{\Omega(C - A')} \frac{\partial m_x(t)}{\partial t} + m_y(t) = \phi_{ra,y}(t) - \frac{1}{\Omega} \frac{\partial \phi_{ra,x}(t)}{\partial t} \tag{2.5}$$

$$\frac{A'}{\Omega(C - A')} \frac{\partial m_y(t)}{\partial t} - m_x(t) = -\phi_{ra,x}(t) - \frac{1}{\Omega} \frac{\partial \phi_{ra,y}(t)}{\partial t} \tag{2.6}$$

$$\frac{1}{\Omega} \frac{\partial m_z(t)}{\partial t} = -\frac{1}{\Omega} \frac{\partial \phi_{ra,z}(t)}{\partial t} \tag{2.7}$$

where the functions $\phi_{ra,i}(t)$ are so-called excitation functions and are defined according to

$$\phi_{ra,x}(t) = \frac{1}{C - A'} \left(\Delta I_{xz}(t) + \frac{1}{\Omega} h_x(t) \right) \tag{2.8}$$

$$\phi_{ra,y}(t) = \frac{1}{C - A'} \left(\Delta I_{yz}(t) + \frac{1}{\Omega} h_y(t) \right) \tag{2.9}$$

$$\phi_{ra,z}(t) = \frac{1}{C} \left(\Delta I_{zz}(t) + \frac{1}{\Omega} h_z(t) \right). \tag{2.10}$$

The excitation functions 2.8 to 2.10 together with the set of differential equations 2.5 to 2.7 relate mass and motion variations on the rigid Earth to the observable Earth Orientation Parameters (EOPs). However, it is clear that the Earth is not rigid but deformable. Additionally, the Earth's interior is not homogeneous but features a crust, mantle and a core. This differentiation raises the question of how to define a body fixed reference frame exactly. Tisserand (1891) suggested to fix it on the mantle in order to neglect crustal and mantle motion. Consequently, the influence of the core requires further investigation. Smith and Dahlen (1981) defined the influence of the core motion on the relative angular momentum of the rigid axisymmetric mantle. Further, they applied the findings of Dahlen (1976), who included the Earth rotational deformation and its response to the passive ocean, in order to simulate a theoretical Chandler wobble for an elastic axisymmetric Earth with a fluidal core and an equilibrium ocean. They find the modeled period about 7.4 days short of the observations and relate this error to falsified modeling of the mantle unelasticity. In the absence of a better mantle model, the observed Chandler frequency is included as further factor in the coupled differential equations.

Considering all the above mentioned features, the new excitation functions are:

$$\chi_1(t) = \frac{\alpha_1}{C - A'} \left(\alpha_2 \delta I_{13}(t) + \frac{1}{\Omega} h_1(t) \right) \tag{2.11}$$

$$\chi_2(t) = \frac{\alpha_1}{C - A'} \left(\alpha_2 \delta I_{23}(t) + \frac{1}{\Omega} h_2(t) \right) \tag{2.12}$$

$$\chi_3(t) = \frac{\alpha_3}{C} \left(\alpha_4 \delta I_{33}(t) + \frac{1}{\Omega} h_3(t) \right), \tag{2.13}$$

where χ_1 and χ_2 represent the polar motion or equatorial and χ_3 the axial excitation. The constants α_i describe rotational deformation, loading and decoupling of the core and are given in the appendix in table 7.1. The coefficients used in this work are in agreement with Dobslaw et al. (2010), because the herein computed Earth rotation excitations are compared to their data. The coefficients are the same as the ones given by Gross (2007), except for a slight deviation in α_1. However, these values are under continuous discussion (Chen and Shen, 2010).

Equations 2.11 and 2.12 define the polar motion excitation in radians, which is converted to milliarcseconds (mas) by multiplying with $\frac{1000*360\circ*60'*60''}{2*\pi}$. Accordingly, equation 2.13, which represents changes in the length of day (ΔLOD), is converted to milliseconds (ms) by multiplying with $\frac{1000*2*\pi}{\Omega}$.

The computation of the small perturbations of the Earth inertia is performed according to:

$$\delta I_{i3}(\mathbf{r},t) = R^2 \times W_i^I(\mathbf{r}) \times M(\mathbf{r},t), \tag{2.14}$$

and variations in the relative angular momentum according to

$$h_i(\mathbf{r},t) = R \times [W_i^u(\mathbf{r}) \times u(\mathbf{r},t) + W_i^v(\mathbf{r}) \times v(\mathbf{r},t)] \times M(\mathbf{r},t). \tag{2.15}$$

Here, R is the Earth radius, $W_i^j(\mathbf{r})$ is the weighting function that depends on the positioning vector **r**, and $M(\mathbf{r},t)$ represents the mass components, which are variable in time (t) and space (**r**). The motion components u(**r,t**) and v(**r,t**) are positively defined in easterly and northerly direction. Table 7.1 summarizes all related geodetic parameters.

The weighting functions are defined according to:

$$W^I(\phi,\lambda) = \cos(\phi) \begin{pmatrix} -\sin(\phi)\cos(\lambda) \\ -\sin(\phi)\sin(\lambda) \\ \cos(\phi) \end{pmatrix} \tag{2.16}$$

$$W^u(\phi,\lambda) = \begin{pmatrix} -\sin(\phi)\cos(\lambda) \\ -\sin(\phi)\sin(\lambda) \\ \cos(\phi) \end{pmatrix} \tag{2.17}$$

$$W^v(\phi,\lambda) = \begin{pmatrix} \sin(\lambda) \\ -\cos(\lambda) \\ 0 \end{pmatrix}. \tag{2.18}$$

Note that the weighting functions depend only on longitude ϕ and latitude λ, while the mass and motion components may additionally depend on a vertical component. For a better understanding of the weighting functions, Figure 2.1 (a-c) visualizes $W^I(\phi,\lambda)$ for all three components of the Earth rotation. The interpretation of this figure is: positive mass anomalies on a positive weighted area (red) and negative mass anomalies on negative weighted areas (blue) will have a positive effect on δI and vice versa.

Weighting functions $W^u(\phi,\lambda)$ and $W^v(\phi,\lambda)$ are visualized in Figure 2.1 (d-f) as a vector field. Here, the interpretation is that motion anomalies in direction of the vector field will have positive effects on h_i, while motion against the field causes negative h_i anomalies.

Integrating $\delta I_{i3}(\mathbf{r},t)$ and $h_i(\mathbf{r},t)$ over all spatial elements **r**, yields the desired functions $\delta I_{i3}(t)$ and $h_i(t)$, which can be inserted into equations 2.11 to 2.13. The integration for this study is performed by simple area weighted summation over the spatial domain.

The excitation functions discussed within this work are computed for a set of different model experiments performed with the Community Earth System Model (CESM, described in

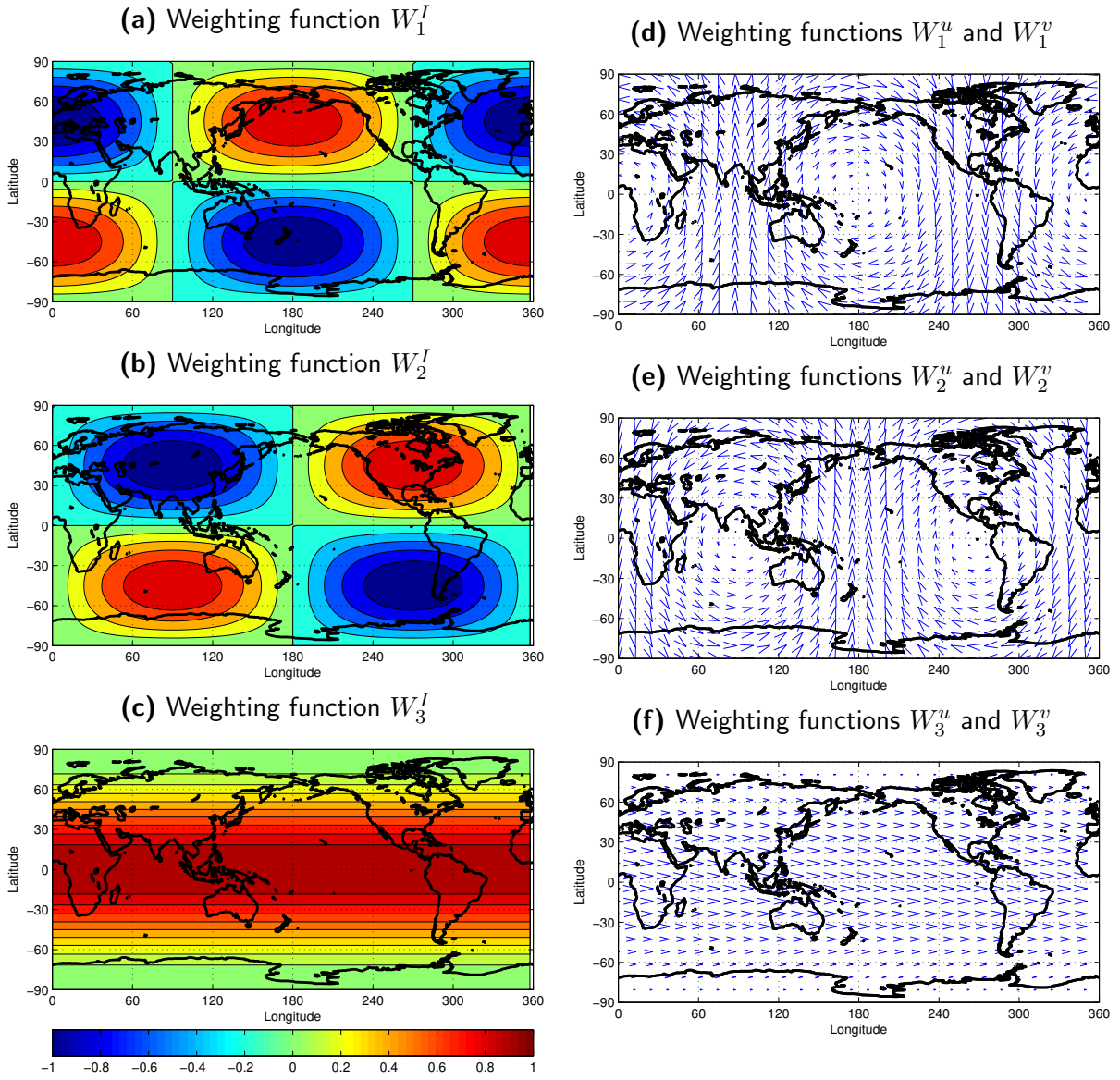

Figure 2.1: Weighting functions of the Earth Rotational Excitation for the mass (a-c) and motion (d-f) components. Positive mass anomalies on red areas, as well as negative ones on blue areas (a-c) have a positive effect on the associated excitation. Moving mass along the vector field (d-f) has a positive effect on the relative excitation.

all detail in section 3.2.1). The Atmosphere Angular Momentum (AAM) is computed between the surface pressure and 5.1×10^{-6} hPa ($\approx$ 140 km). The Ocean Angular Momentum (OAM) is computed for the entire ocean, from the ocean bottom to the ocean surface. The Hydrosphere Angular Momentum (HAM) is computed only for the mass term (cf. eq. 2.14), since the motion term is at least three orders of magnitude smaller and thus can be neglected (Dobslaw et al., 2010).

For simplicity reasons the contribution of the atmosphere mass (IA) and motion (hA) will be called "surface pressure" and "wind", respectively; while the contribution of the ocean

mass (IO) and ocean motion (hO) will be called "bottom pressure" and "current". The contributions of the continental hydrosphere (IL) will be called continental water. Appended to the acronyms (IA_i, hA_i, IO_i, hO_i, IL_i) is usually a number between 1 and 3, indicating the rotational axis.

2.1.3 Maps of Earth Rotational Excitation Functions

Beyond the excitation functions 2.11 to 2.13, we also discuss maps of excitation functions. This is done in order to investigate, which regions are particularly important for a certain excitation signal.

The excitation maps are computed according to equations 2.14 and 2.15, where only the vertical coordinate is integrated. Separating into mass and motion terms, the excitation maps are defined as:

$$\chi(\phi,\lambda,t)^I_{1,2} = \frac{\alpha_1\alpha_2}{C-A}\delta I(\phi,\lambda,t)_{1,2} \tag{2.19}$$

$$\chi(\phi,\lambda,t)^h_{1,2} = \frac{\alpha_1}{\Omega(C-A)}h(\phi,\lambda,t)_{1,2} \tag{2.20}$$

$$\chi(\phi,\lambda,t)^I_{3} = \frac{\alpha_3\alpha_4}{C}\delta I(\phi,\lambda,t)_{3} \tag{2.21}$$

$$\chi(\phi,\lambda,t)^h_{3} = \frac{\alpha_3}{\Omega C}h(\phi,\lambda,t)_{3}. \tag{2.22}$$

Here, $\chi(\phi,\lambda,t)^I_j$ and $\chi(\phi,\lambda,t)^h_j$ represent solely the vertical integrated excitation functions for the mass and motion terms, respectively. Integrating both functions over the sphere yields the time series of the excitation functions $\chi_i(t)$.

The previous section is the theoretical basement for all upcoming analyses regarding the Earth rotational excitation. This includes the modeled global excitation, which can be compared to observations, as well as the contributions of all modeled subsystems. Additionally, the excitation maps will allow to identify regions of particular strong excitation for all subcomponents separately. In order to analyze whether these excitations interact with each other, the upcoming section describes Sverdrup's Theory, which links changes in the ocean mass with variations of the prevailing atmospheric wind pattern.

2.2 Sverdrup's Theory

Stewart (2008) provides a comprehensive derivation of the momentum equations of a fluid mass under the influence of external forces. He mentions four important forces acting on the ocean: the pressure gradient, Coriolis force, gravity and friction, such that the total derivative of the fluid motion $\vec{v}$, under the assumption of constant density and incompressible flow is:

$$\frac{D\vec{v}}{Dt} = \frac{\partial \vec{v}}{\partial t} + \vec{v}\nabla\vec{v} = -\frac{1}{\rho}\underbrace{\nabla p}_{Pressure} \underbrace{-2\Omega \times \vec{v}}_{Coriolis} + \underbrace{g}_{Gravity} + \underbrace{F_r}_{Friction} . \tag{2.23}$$

Based on this momentum equation (also known as the Navier-Stokes equation), Sverdrup derived his theory, relating atmospheric winds to ocean mass transport. First he relaxed this equation by applying several assumptions:

Material derivative $\frac{D\vec{v}}{Dt}$ describes the temporal rate of change of a fluid $\vec{v}(x,t)$, that depends on time and location. Sverdrup assumed this to be zero, which means a stationary flow (no temporal variations: $\frac{\partial \vec{v}}{\partial t} \approx 0$) with negligible non-linear terms (no convective acceleration: $\vec{v}\nabla\vec{v} \approx 0$). Thus the whole left side of equation 2.23 is zero.

Pressure gradient The influence of the pressure gradient is totally accounted for in Sverdrup's theory.

Coriolis In Sverdrup's theory the Coriolis force is accounted for under the assumption of $w \ll u, v$, or in words: negligible small vertical mass movement, compared to the horizontal motion. This way $2\Omega w \cos\phi \approx 0$ can be neglected for the x component of $\Omega \times \vec{v}$ in equation 2.23.

Gravity Sverdrup considers the horizontal momentum equations, disregarding horizontal and radial gravity variations.

Friction Molecular friction is neglected for the ocean. The ocean turbulence, however, is treated as friction, in such a way, that the eddy viscosity is defined in analogy to the molecular viscosity. Therefore the assumption is that the eddy viscosity actually describes the ocean turbulence.

Using the above mentioned assumptions relaxes equation 2.23 for the horizontal terms to:

$$\frac{\partial p}{\partial x} = \quad f\rho v + \frac{\partial}{\partial z}\left(A_z \frac{\partial u}{\partial z}\right) \tag{2.24a}$$

$$\frac{\partial p}{\partial y} = -f\rho u + \frac{\partial}{\partial z}\left(A_z \frac{\partial v}{\partial z}\right), \tag{2.24b}$$

where x,y,z represent the coordinate system, u,v the associated velocity components, ρ is the density of the fluid, p the pressure, A_z the eddy viscosity and finally the Coriolis parameter $f = 2\omega \sin(\phi)$, where ϕ is the latitude and ω the rotation rate of the Earth.

Now these equations are integrated from the surface (0 meters) to the depth -D, where the horizontal pressure gradient is zero. Integrating the left hand side with respect to these boundaries yields:

$$\frac{\partial P}{\partial x} = \int_{-D}^{0} \frac{\partial p}{\partial x} dz \tag{2.25a}$$

$$\frac{\partial P}{\partial y} = \int_{-D}^{0} \frac{\partial p}{\partial y} dz. \tag{2.25b}$$

Integrating the first term on the right hand side under the assumption of a depth independent Coriolis term leaves an integration of density times velocity over a certain distance (here depth -D), which results in a mass transport according to:

$$M_x = \int_{-D}^{0} \rho v(z) dz \tag{2.26a}$$

$$M_y = \int_{-D}^{0} \rho u(z) dz \tag{2.26b}$$

In order to integrate the last term on the right hand side of equation 2.24 requires the assumption that the eddy viscosity A_z is constant with depth or at least significantly slower changing on the vertical axis than velocity itself. In analogy to the relation between the stress term and the molecular viscosity ($T_{xz} = \rho\nu\frac{\partial u}{\partial z}$), the relation for the eddy viscosity is:

$$T_{xz} = A_z \frac{\partial u}{\partial z} \tag{2.27a}$$

$$T_{yz} = A_z \frac{\partial v}{\partial z}. \tag{2.27b}$$

Inserting equation 2.27 into 2.24 and integrating from the surface to depth -D yields

$$\int_{-D}^{0} \frac{\partial}{\partial z}\left(A_z \frac{\partial u}{\partial z}\right) dz = \int_{-D}^{0} \frac{\partial T_{xz}}{\partial z} dz = T_{xz}\Big|_{-D}^{0} \tag{2.28a}$$

$$\int_{-D}^{0} \frac{\partial}{\partial z}\left(A_z \frac{\partial v}{\partial z}\right) dz = \int_{-D}^{0} \frac{\partial T_{yz}}{\partial z} dz = T_{yz}\Big|_{-D}^{0}. \tag{2.28b}$$

This leaves the integration of the last term of equation 2.24 to be the stress terms (T_{xz}, T_{yz}) at the surface and depth -D. The stress at the surface equals the wind stress, while the stress at the depth -D is by definition zero:

$$T_{xz}\Big|^{0} = T_x, \qquad T_{yz}\Big|^{0} = T_y \tag{2.29a}$$

$$T_{xz}\Big|_{-D} = 0, \qquad T_{yz}\Big|_{-D} = 0. \tag{2.29b}$$

Inserting the above derived integration solutions into equation 2.24 yields:

$$\frac{\partial P}{\partial x} = \quad fM_y + T_x \tag{2.30a}$$

$$\frac{\partial P}{\partial y} = -fM_x + T_y. \tag{2.30b}$$

Similarly, Sverdrup integrated the continuity equation, showing that

$$\frac{\partial M_x}{\partial x} + \frac{\partial M_y}{\partial y} = 0. \tag{2.31}$$

Differentiating equations 2.30a with respect to y and 2.30b with respect to x, subtracting both and inserting them into the integrated continuity equation (2.31) yields the north-south mass flux M_y according to:

$$\beta M_y = \frac{\partial T_y}{\partial x} - \frac{\partial T_x}{\partial y}. \tag{2.32}$$

Conveniently is the right hand side of this equation the curl of the wind stress, such that

$$\nabla \times \vec{T} = curl_z(\vec{T}) = \frac{\partial T_y}{\partial x} - \frac{\partial T_x}{\partial y}. \tag{2.33}$$

On the left hand side of equation 2.32 the north-south mass flux M_y is multiplied by the rate of change of the Coriolis parameter with respect to latitude:

$$\beta = \frac{\partial f}{\partial y} = \frac{2\Omega \cos\phi}{R}. \tag{2.34}$$

In regions of a predominantly zonal wind regime (eg., tropical and North Pacific ocean around 30°N) $\frac{\partial T_y}{\partial x}$ is insignificant, leaving the north-south mass flux as

$$M_y \approx -\frac{1}{\beta}\frac{\partial T_x}{\partial y}. \tag{2.35}$$

The derivation of the lateral (east-west) mass transport M_x is for example explained in Stewart (2008) Introduction to Physical Oceanography. The result is:

$$M_x = \frac{\Delta x}{2\Omega \cos\phi} \left[\frac{\partial T_x}{\partial y} \tan\phi + \frac{\partial^2 T_x}{\partial y^2} R \right], \tag{2.36}$$

where Δx is the distance from the eastern shore. The mass flux $M_x(\Delta x = 0)$ on the eastern boundary is zero. The last equation is just for completeness, for the purpose of this study, the derivation of M_y will suffice.

Sverdrup's theory is a powerful tool for investigating the wind driven oceanic mass transport. However, the derivation requires several assumptions which might interfere with nowadays observation and modeling capacities. Thus one needs to be aware of the limitations implied by the initial assumptions.

2.3 Data

2.3.1 Observed Earth Orientation Parameters

The International Earth Rotation and Reference Systems Service (IERS) publishes definitions for the International Celestial Reference Frame (ICRF) and the International Terrestrial Reference Frame (ITRF). Additionally, IERS provides the observed Earth Orientation Parameters (EOP), which transform coordinates from one reference system to the other (Vondrák and Richter, 2004). The data can be downloaded from the IERS website[1]. The herein presented results make use of the EOP-C04 data set, which is provided from 1962 to 2010. This data considers a set of observations, such as: GPS, Very Long Baseline Interferometry, lunar and satellite laser ranging and optical astronomy. Bizouard and Gambis (2008) describe the data processing in all detail. The precision of the observed Earth's intermediate rotational pole is 0.05 milliarc seconds within the terrestrial reference frame (Bizouard and Seoane, 2009). Additional information can be obtained from the IERS technical report 2010 (Petit and Luzum, 2010).

The observed EOPs are converted to geodetic excitation functions or Earth Rotational Excitation (ERE) according to Wilson and Vicente (1990). They find a Chandler frequency of $T_{CW} = 433.0 \pm 1.1$ solar days and a damping factor of $Q = 179$. Gross (2007) recommends using exactly these values, which is done in this study.

[1] `http://www.iers.org/`

2.3.2 Operational Earth Rotation Excitation

The operational EREs are provided by the GFZ German Research Centre for Geosciences and are freely available for download[1]. The herein provided EREs contain excitation functions separated into mass and motion components for atmosphere (AAM), ocean (OAM) and land (HAM). The atmosphere data comes from the European Centre for Medium-Range Weather Forecasts (ECMWF), which is used to force the Ocean Model for Circulation and Tides (OMCT) and the Land Surface Discharge Model (LSDM). Mass conservation among the three subsystems is accounted for by means of freshwater fluxes. The operational EREs are provided for four different atmospheric data sets, including ECMWF ERA-40 reanalysis (1958 - 2001), ECMWF ERA-Interim reanalysis (1989 - 2008), operational ECMWF (2001 - now) and ECMWF 10-day forecast. For this study, only ERA-40 and ERA-Interim reanalysis data is used. Dobslaw et al. (2010) and Dill and Dobslaw (2010) give all related details regarding the operational EREs.

2.3.3 GRACE

The Gravity Recovery and Climate Experiment (GRACE) satellite mission was launched in March 2002 and provides global observations of the Earth's gravity field in the form of monthly sets of spherical harmonic coefficients (Tapley et al., 2004b). Temporal mass variations are estimated using time-varying coefficients (Wahr et al., 1998).

The herein processed GRACE data is the RL05 solution of the GFZ German Research Centre for Geosciences in Potsdam (Dahle et al., 2012). Currently, the data covers 72 months (01/2005 - 12/2010) and have been synthesized as mass distribution grids in meter of equivalent water thickness with a spatial resolution of $1^\circ \times 1^\circ$. The data has been processed according to Chambers (2006), but in contrast no GIA correction was applied. Additionally, a non-isotropic two-point kernel filter (Kusche, 2007) has been applied for destriping. Further destriping of the GRACE RL05 data is achieved using an EOF reconstruction method as described by Chambers and Willis (2010).

All the above described GRACE related preprocessing steps of the herein used data, have been performed by Inga Bergmann Wolf.

2.4 Data Processing

This section describes all data processing routines that are applied in this study. All data sets, including observations, operational and modeled data, are processed with the same routines.

[1] http://www.gfz-potsdam.de/portal/gfz/Struktur/Departments/Department+1/sec13/services

Indices are treated as simple time series, while gridded data are treated as time series for each grid point separately.

First the data is detrended. Then the long term variability is reduced by applying a high-pass Butterworth filter with a half power point or cutoff frequency at 7 years, allowing daily to interannual variability. The cutoff frequency is chosen such that observed long term variations related to core-mantle coupling or post-glacial rebound are excluded. On the other hand interannual climate variations related to ENSO or NAM are present in the data. For better filtering results at the boundaries, the start and end points of the time series are padded towards zero using an arc tangent function.

Now the data still includes a seasonal cycle, which is investigated for example by computing the average day or month for the whole time series. This means for example, that all Januaries are concatenated in one time series. The average of this time series is the average January value. This is repeated for all months giving an average annual cycle. Additionally, the standard deviation is computed for each monthly time series, allowing the evaluation of the monthly variability and thus the variability of the annual cycle. Interannual variations are computed by removing the average annual cycle from the whole time series.

2.4.1 Composite Mean Differences

We use Composite Mean Differences (CMDs) to visualize the spatial effects of a certain phenomena. A field (e.g., surface pressure) is sorted with respect to an index (e.g., Nino3.4 index representing the El Niño Southern Oscillation). In general we show maximum conditions minus minimum conditions, where we define the maximum conditions as the index exceeding one standard deviation and minimum conditions as all time steps, where the index is below minus one standard deviation. However, the thresholds can be chosen manually. The data field is now separated into maximum and minimum composites (e.g., all El Niño months form one composite and all La Niña months form the other one). Both composites are averaged and subtracted from one another, visualizing maximum minus minimum conditions. For example, Figure 3.8 (a) shows the Nino3.4 CMDs of the global surface pressure. This is the difference in surface pressure of the average El Niño minus the average La Niña event. CMDs are commonly used to analyze the relation of a certain time series on a field (Labitzke et al., 2002; Camp and Tung, 2007).

2.4.2 Bootstrapping

The bootstrap algorithm (Efron, 1979; Efron and Tibshirani, 1993) is highly qualified for the evaluation of uncertainties of the CMD results. This is due to the nature of CMDs, where we have a maximum and a minimum composite consisting of N and M samples, respectively.

The bootstrap analysis now takes a set of randomly chosen samples from the maximum and minimum composite and computes the differences between these random samples. In more detail we choose exactly N and M samples, respectively, but allow multiple appearance. This means that a composite may consist of only one time slice, which is chosen N times in a role. In our study this choosing process is repeated 1000 times giving 1000 fields of differences. The significance is computed based on the statistical distribution of these 1000 fields. In this study all figures considering statistical significance, show only values exceeding 99% statistical significance (e.g., Figures 3.6, 3.8), which means that 99% of the differences show the same sign and are none-zero. One major advantage of bootstrapping is that it requires no a priori information with respect to the analyzed data.

2.4.3 Empirical Orthogonal Functions

Empirical Orthogonal Function (EOF) analysis is a method which decomposes multivariate data sets into orthogonal basis functions (Preisendorfer and Mobley, 1988; Bjornsson and Venegas, 1997). In other words, the data set is transformed into a new coordinate system (defined by the EOFs), where the axes are ordered with respect to their variance, meaning that the first EOF explains most of the total variance and the last EOF explains the least amount of variance. The transformed variables are called Principle Components (PCs) and can be linearly combined with the EOFs to compute the original data.

In this study the multivariate data d depends only on time and location and is decomposed into spatial patterns (EOFs) and temporal variations (PCs). EOFs are by definition orthogonal to each other and PCs are uncorrelated. As mentioned above, the linear combination of both yields the initial data, creating a system of linear equations according to:

$$d = PC \times EOF \tag{2.37}$$

The associated dimensions are $d : [t, r]$,$PC : [t, n_{EOF}]$ and $EOF : [n_{EOF}, r]$, with t the temporal and r the spatial dimension. n_{EOF} denotes the number of considered EOFs. The maximum number of EOFs (n_{EOF}) for a unique solution is equal to the number of elements of the smallest dimension of the data d. For example, if the data is only a time series (spatial dimension is one) then the EOF analysis would give one PC and one scaling factor (EOF). Multiplying both, yields the initial time series.

Based on the linear equations above, it is also possible to filter a spatial pattern with respect to a data set d. This means we define a new spatial pattern or coordinate axis (not necessarily orthogonal) and compute the associated time series of the projected variable. Equation 2.38 performs this projection, where d is the data set, EOF is the new spatial pattern (or new

axis) and PC is the new time series representing the appearance of pattern EOF in the data set d:

$$PC = d \times EOF^T \times \left(EOF \times EOF^T\right)^{-1} \tag{2.38}$$

Accordingly, it is possible to project a certain time series on a data set and retrieve the associated axis or spatial pattern. This is done by equation 2.39, which solves equation 2.37 with respect to the field EOF. If the data set d would have no spatial dimension, but only a temporal one, then this equation would describe the solution of a general Multiple Linear Regression (MLR), where d is the initial time series, PC are the different regressors (e.g., climate indices) and EOF is the MLR coefficient. The MLR usually includes several indices but only one data time series, which makes the system of linear equations overdetermined, permitting a unique solution. In general this problem is solved using least squares, which minimizes the error:

$$EOF = \left(PC^T \times PC\right)^{-1} \times PC^T \times d \tag{2.39}$$

2.4.4 Multiple Linear Regression

The Multiple Linear Regression (MLR) is a widely used and robust method for the evaluation of the impact of certain factors (SPARC CCMVal, 2010). As mentioned above, the MLR and EOF analysis are closely related. The math describing the solution is the same for both methods, only the initial assumptions differ. For the EOF analysis the PCs (and the EOFs) are by definition orthogonal, while the regressors of a MLR might be correlated. Computing the MLR coefficients for all PCs of the associated data set d, will give exactly the EOF pattern with the error equal to zero. However, the MLR does not require independent regressors (PCs) but solves the overdetermined system of equations in a least squares sense introducing an error term ε. The system of linear equations is

$$d = X \times b + \varepsilon, \tag{2.40}$$

where d is the data, b is a set of constants, X is a set of time series and ε is the error. Equations 2.37 and 2.40 are virtually the same and thus are the solutions:

$$b = \left(X^T \times X\right)^{-1} \times X^T \times d. \tag{2.41}$$

There are other ways of solving the equation for b, for example considering weighting functions or covariance matrices. Nevertheless, the most common solution applying simple least squares is given above.

Chapter 3

Model Description and Experimental Design

3.1 Introduction

In May 1981 Nobel Price winner Richard Feynman ended his Key Note Lecture entitled "Modeling Physics with Computers" with a for any climate modeler utterly discouraging sentence: "Nature isn't classical, dammit, and if you want to make a simulation of nature you'd better make it quantum mechanical" (Feynman, 1982). Unfortunately not even the collective computational power of all computers of the world would suffice to meet this requirement for the mere modeling of an unperturbed cup of tea. Consequently any simulation describing the real world can only be an approximation with a limited accuracy.

The simplest approach on simulating or modeling a real world phenomenon is based on experiences or in other words statistics. A very basic statistical model, for example based on correlation, would predict that the average temperature in Berlin on the 1st of May is higher than on Christmas Eve. However these very simple statistical models allow to predict a certain phenomenon only within a certain range of experience.

More advanced models use the classical equations of physics in order to describe real world phenomena. In the context of climate studies these models are usually discretized on a certain grid aiming to reproduce the observed behavior of a system. These models by definition cannot describe subgrid phenomena even though these phenomena might be of importance for the quality of the modeling result. In order to further improve the modeling results the effect of these subscale phenomena, such as clouds, is approximated based on experiences or in other words parameters. In modern global scale climate models we find a whole concert of parameters describing subgrid phenomena. As indicated above, the resolution related limitations do not relate to a lack of physical understanding but clearly to the lack of computer resources. This includes the lack of computational power as well as the lack of data storage.

However, despite the limited accuracy of computer simulations there are clear advantages of modeling experiments. For example, one can perform sensitivity studies varying any model parameter and thus analyze the sensitivity of the system with respect to this parameter. This is for example done analyzing natural variations (e.g. change the QBO or solar cycle, Matthes et al. (2010)) or anthropogenic variations (e.g., change CO_2, Taylor et al. (2009)). In contrast, there is only one observable Earth. Model experiments also allow a prediction of the future climate and thus are of crucial importance for social and political decisions. Further, global models offer data at places that are not or only badly observed. They also allow investigations of observed variables in more detail. For example, observed Earth Rotation can be separated into the effects of subcomponents, leading to a better understanding of the underlying physics.

This chapter provides a detailed description of the relevant models for this study. This includes the Ocean Model for Circulation and Tides (OMCT), the Whole Atmosphere Community Climate Model (WACCM) and the Community Earth System Model (CESM). Further, this chapter discusses the experiments that are performed for this study. Finally, CESM is validated upon its capabilities to reproduce ENSO and NAM.

3.2 Models

3.2.1 Community Earth System Model - CESM

The Community Earth System Model is a well documented state-of-the-art coupled chemistry-climate model that is freely available for download[1]. It was developed by the National Center for Atmospheric Research (NCAR). Its predecessor CCSM3 (Collins et al., 2006) was used for several climate studies of the Intergovernmental Panel on Climate Change (IPCC) Fourth Assessment Report (Randall et al., 2007).

Within the CESM framework, the user is free to combine a different set of Earth system components, including atmosphere, ocean, land and ice, on different sets of model resolutions from coarse (4°x 5°) to fine (0.23°x 0.23°). Gent et al. (2011) give an extensive overview of the current capabilities and latest improvements of CESM.

In general the atmosphere component can be modeled with either (a) the Community Atmosphere Model - CAM, current version is CAM5 (Neale et al., 2010; Collins et al., 2006); or (b) the Whole Atmosphere Community Climate Model - WACCM, current version is WACCM4.0 (Garcia et al., 2007). The ocean is modeled using the Parallel Ocean Program - POP2, (Smith et al., 2010; Danabasoglu et al., 2011), while the land component is simulated using Community Land Model - CLM4, (Lawrence et al., 2011). Finally the sea ice component is described by the Community Ice CodE - CICE4, (Hunke and Lipscomb, 2010;

[1] http://www.cesm.ucar.edu/

Bailey et al., 2012). The latest CESM version 1.1 also includes a land ice component called the Community Ice Sheet Model (Glimmer - CISM). Additionally in this version, all major rivers where separated from the land component and form now the River Transport Model (RTM).

All the enabled model components communicate interactively via a coupler. It is possible to disable any of the aforementioned components and substitute it with a data component. This setting is for example applied in experiment ATMOS, where the ocean is turned off, using prescribed ocean data as boundary conditions for the other components.

A special issue in the Journal of Climate is dedicated to CESM, discussing the capabilities and limitations of CESM in great detail[1]. The relevant CESM related literature is referenced and discussed throughout the manuscript, in order to evaluate the modeling results more comprehensively. In more detail, CESM results are especially investigated in chapters 5. Atmosphere, Ocean and Land induced Earth Rotational Excitations and 6. North Pacific Mass Variations.

3.2.2 Ocean Model for Circulation and Tides - OMCT

The Ocean Model for Circulation and Tides (OMCT; Thomas et al. (2001)) is based on the Hamburg Ocean Primitive Equation model (HOPE; Wolff et al. (1997); Drijfhout et al. (1996)) and includes an additionally ephemeral tidal model. However, for all experiments related to this study, the tidal model is disabled. The OMCT solves the nonlinear momentum equations, applying the hydrostatic and Boussinesq approximations. It also satisfies the continuity equations and conservation equations for heat and salt. The horizontal velocity components, water elevation, potential temperature and salinity distribution are prognostically calculated variables. The vertical velocity component is calculated diagnostically using the continuity equation. Ice thickness, compactness, and drift are predicted with the included prognostic thermodynamic sea ice model. The OMCT has a horizontal resolution of 1.875° x 1.875° and 13 vertical layers. The model time step is 30 minutes. Atmospheric meridional and zonal wind stress, surface pressure, 2m temperature and freshwater fluxes are used to force the model. The OMCT is generally used at GFZ to de-alias GRACE satellite data (Flechtner, 2007). Recently, Dobslaw et al. (2010) used ERA reanalysis data to force the OMCT and a continental hydrosphere model to investigate the contributions of the Earth subsystems (atmosphere, ocean, hydrosphere) to Earth rotation, i.e. polar motion. OMCT results are investigated in chapter 4. Natural Variations in Stand-Alone Models.

[1] http://journals.ametsoc.org/page/CCSM4/CESM1

3.3 Experimental Design: CESM

As described above, CESM offers the possibility to couple several model components, which allows to investigate not only modeled climate sensitivity but also coupling effects. In order to investigate the natural climate variability we perform a set of four experiments, including (1) NATURAL featuring only natural variations; (2) NOQBO, which is the same as (1) just without a nudged quasi-biennial oscillation (QBO); (3) RCP considering anthropogenic variations, such as variable greenhouse gas (GHG) concentrations; and (4) ATMOS featuring a climatological data ocean, repeating the same annual cycle. All experiments are summarized in table 3.1 at the end of this section, while a detailed explanation for every experiment is given below.

All hereafter described CESM experiments are based on the CESM version 1.0.2, which was released in December 2010. The release notes[1] provide all related information. The modeling experiments were performed at the Deutsche Klimarechenzentrum (DKRZ) Hamburg.

All of the discussed CESM experiments are performed using the same model structure regarding horizontal and vertical resolution. In more detail, the atmosphere is modeled by WACCM3.5 on a horizontal resolution of 2.5°x 1.9°and 66 vertical levels up to 5.1×10^{-6} hPa (≈ 140 km). The land component (CLM4) is predefined on the same resolution as the atmosphere and offers up to 15 vertical layers. The ocean is modeled on a curvilinear grid with a horizontal resolution of roughly 1°(Smith et al., 2010) and 60 vertical layers. The sea ice component is on the same resolution as the ocean.

3.3.1 NATURAL

This experiment includes all interactive components: WACCM 3.5, CLM4, CICE4 and POP2 and is simulated from 1955 to 2100. It uses observed external forcings (e.g., solar cycle, QBO, no volcanoes) and projects them into the future. The spectrally resolved solar irradiance which changes from the far-ultraviolet to the near-infrared, is projected into the future by repeating cycles 20-23 from the years 1965 to 2008. The QBO is projected into the future by developing Fourier coefficients for the QBO time series, based on climatological values of Giorgetta[2]. These coefficients reproduce the observations for the years 1954 to 2004 and are used to expand the time series into the future (Neale et al., 2010).

All anthropogenic forcings such as GHGs, ODS, or airplane emissions are kept constant on a 1960s level, showing only an annual cycle, which was repeated for the whole modeling time. Therefore experiment NATURAL represents quasi natural variations, neglecting anthropogenic induced variations.

[1] http://www.cesm.ucar.edu/models/cesm1.0/tags/index.html

[2] http://www.pa.op.dlr.de/CCMVal/Forcings/qbo_data_ccmval/u_profile_195301-200412.html

3.3.2 NOQBO

This model experiment is identical to experiment NATURAL, solely leaving out the QBO nudging. Figure 3.1 shows the differences of the stratospheric zonal mean zonal wind, between both scenarios: a) the QBO is nudged towards observations (green line); and b) the model is unconstraint (blue line). As indicated by Figure 3.1, experiment 3.3.2 is performed from 1955 to 2010. The effect of the nudging is obvious; while the observed winds oscillate between $15\frac{m}{s}$ westerlies and $25\frac{m}{s}$ easterlies, the free and unconstraint experiment NOQBO experiences relatively stable easterly winds with an amplitude of about $10\frac{m}{s}$.

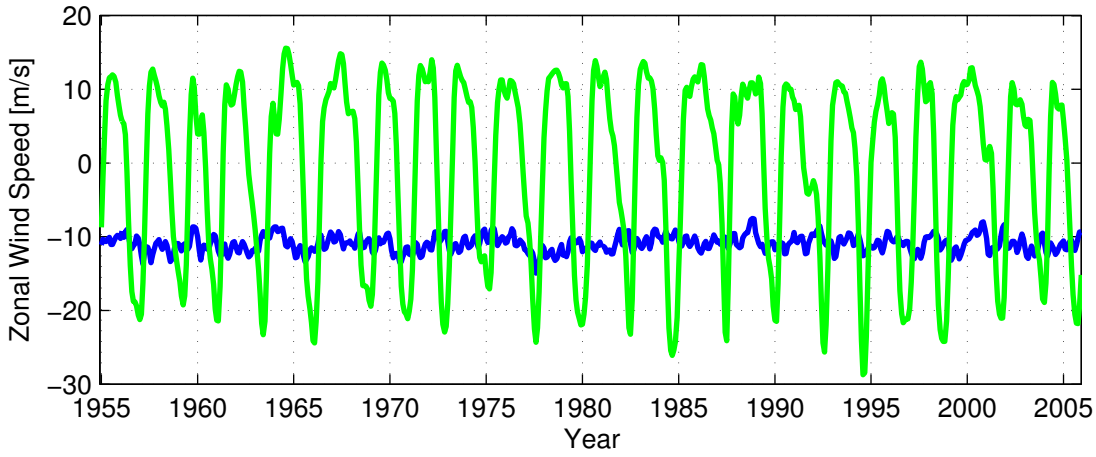

Figure 3.1: Green: QBO time series for the zonal mean zonal wind in the equatorial stratosphere as observed and nudged in the model experiments NATURAL, ATMOS and RCP ; Blue: zonal mean zonal wind in the same region, but for the free and unconstrained experiment NOQBO.

The QBO has significant global effects on the stratosphere and the troposphere (Baldwin et al., 2001). It for example alters the influence of other sources of natural variations, such as the solar cycle (Matthes et al., 2010). Additionally it influences the change in length of day on an internal timescale (Chao, 1989). Petrick et al. (2012) for example showed that nudging the QBO strengthens the solar cycle response in the southern hemispheric stratosphere down to the ocean, which shows a significant solar cycle response only for the nudged scenario.

All the previous studies are based on either observation or stand-alone atmospheric or ocean models. Comparing experiments NATURAL with NOQBO allows for the first time to quantify the influence of the QBO in a coupled climate system. Comparing this to previous stand-alone experiments will additionally indicate the influence of the coupling itself.

3.3.3 ATMOS

This experiment is again identical to the reference experiment NATURAL with the only difference, that the ocean and ice component is not interactively coupled. Instead, this experiment

consists only of the interactive atmosphere and land components. The oceanic and ice related boundary conditions for this scenario are climatological values computed from experiment NATURAL. We used the full ocean and ice data set (from 1955 to 2100) in order to compute a monthly mean seasonal cycle. This averaged annual cycle is repeated for the whole modeling period from 1955 to 2010. Thus, this experiment does not experience ocean related phenomena such as the El Niño Southern Oscillation.

Consequently, it is excellently suitable for analyzing and quantifying atmosphere-ocean coupling effects by comparing to experiment NATURAL. In more detail, it allows to quantify the influence of interannual ocean features, such as ENSO, on the atmosphere.

3.3.4 RCP

This experiment is identical to the first one (NATURAL), but now including all model relevant anthropogenic forcings. This relates mainly to GHGs and airplane emissions, which follow the observations for the whole modeling period from 1955 to 2010.

Comparing this experiment to NATURAL allows to quantify the anthropogenic share of the modeled climate variability.

3.4 Summary of all experiments

Table 3.1 summarizes all experiments that are performed in the context of this study and analyzed throughout this manuscript. This includes the stand-alone OMCT experiments, which are forced using two different WACCM experiments. "Chapter 4 Natural Variations in Stand-Alone Models" describes the differences between both simulations showing that the natural induced variations of the solar cycle and the QBO interact with each other, communicating from the stratosphere to the troposphere into the ocean. This result suggests the possibility feedback from the ocean back into the atmosphere leading directly to the coupled model experiments performed with CESM. Here a set of experiments is performed in order to separate natural from anthropogenic variations, but also coupling effects. "Chapter 5 Atmosphere, Ocean and Land induced Earth Rotational Excitations" describes the differences between those experiments on a global scale using Earth Rotational Excitations (EREs). Additionally, the influence of all subsystems on the total ERE budget is analyzed indicating areas of especially strong coupling effects. One of the most pronounced regions of atmosphere-ocean interaction is the North Pacific, which is analyzed in all detail in "Chapter 6 North Pacific Mass Variations".

Table 3.1: Experiments

CESM 1.0.2

Name	Time	Key Features
NATURAL	1955 - 2100	Natural variations, including realistic solar cycle and QBO nudging. GHG and ODs on 1960s level, featuring only an annual cycle. Initial CESM compset: B1955WCN. Components: WACCM 3.5, CLM4, POP2, CICE4.
NOQBO	1955 - 2010	As NATURAL, but no QBO nudging.
ATMOS	1955 - 2010	As NATURAL, but climatological data ocean and ice components, based on NATURAL ocean output. Active components: WACCM3.5, CLM4.
RCP	1955 - 2010	As NATURAL, but including anthropogenic forcings, GHG and ODs follow observations till 2005, afterward RCP8.5 projections are used.

OMCT

Name	Time	Description
O^{SC}_{QBO}	110 years	Forced with WACCM 3.19, including solar cycle and QBO nudging.
O^{SC}	110 years	Forced with WACCM 3.19, including only solar cycle.

3.5 Climate Indices in Observations and Models

Climate indices represent dominant global scale climate modes such as the Northern and Southern Annular Mode (NAM, SAM) or the El Niño Southern Oscillation (ENSO) in a one dimensional time series. Representing these global scale phenomena in a single time series is clearly a simplification, which carries risks but also great benefits. Advantages are for example an easy quantification and evaluation of the investigated climate mode. On the downside it is possible that a certain index definition is not representing the intended physical phenomena. For example, the upcoming section 3.5.1 discussing the NAM and its definition, reveals deviating physical phenomena between observations and the modeling domain, despite the identical computation of the NAM index.

The forthcoming sections introduce NAM and ENSO in more detail, including a description of the related physical processes as well as the computation of the related indices and a comparison between the modeled and observed features.

3.5.1 Northern Annular Mode - NAM

The Annular Modes (AM) explain most of the anomalous (non-seasonal) atmospheric variability in the extratropics (Thompson and Wallace, 2000; Thompson et al., 2000). The Northern

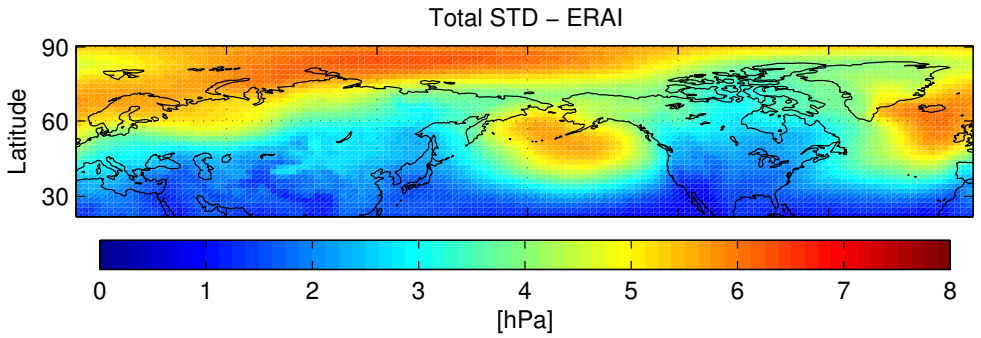

Figure 3.2: Standard deviation of the deseasonalized Mean Sea Level Pressure of ERA-Interim data.

and Southern Annular Mode (NAM and SAM) are hemispheric scale patterns that explain about 20 - 30 % of the total variance of the respective deseasonalized wind and geopotential height fields. The NAM, also know as Arctic Oscillation (AO), is closely related to the North Atlantic Oscillation (NAO), which in fact describes the same physical phenomenon (Kerr, 1999; Wallace, 2000). In contrast to ENSO, the AMs are generated by internal mid-latitudinal atmospheric dynamics. In general, the AMs represent a meridional north-south shift of atmospheric mass, which coincides with a north-south vacillation of the wind field at around 55°- 60° and 30°- 35°. Positive AM are defined by negative pressure anomalies in the polar regions and positive ones in the circumferencing mid-latitudes. The associated increased pressure gradients cause enhanced and northward shifted mid-latitudinal jets (Thompson and Wallace, 2000). The NAM shows enhanced variability during boreal winter, when stratosphere-troposphere coupling is strongest.

Gerber et al. (2010), Thompson and Wallace (2000), and Thompson et al. (2000) showed that the AM variability is influenced by stratosphere-troposphere coupling affects from subseasonal (month-to-month) to interannual timescales. Further, Robertson et al. (2000) find a relation to the north Atlantic Sea Surface Temperatures (SSTs), while Cohen and Entekhabi (1999) and Allen and Zender (2011) establish the connection to the Eurasian snow cover. Additionally, recent studies indicate coupling effects between arctic sea ice distribution (especially in the Atlantic sector) and the NAM (Rigor et al., 2002; Deser et al., 2007; Jaiser et al., 2012).

A common definition of the NAM index is given by Thompson and Wallace (1998) and Baldwin and Thompson (2009) as the Principle Component of the first EOF (cf. 2.4.3) of the deseasonalized Mean Sea Level Pressure north of 20°N. Figure 3.2 shows the total standard deviation of the deseasonalized MSLP of this region for ERA-Interim reanalysis data in hPa. The strongest variations are clearly located in the northern Atlantic ocean, reaching into Arctic ocean. Similarly strong signals are present in the northern Pacific.

For reference Figure 3.3 shows the difference between the total standard deviation of the MSLP of the ERA-Interim data and the MERRA reanalysis data as well as for all CESM

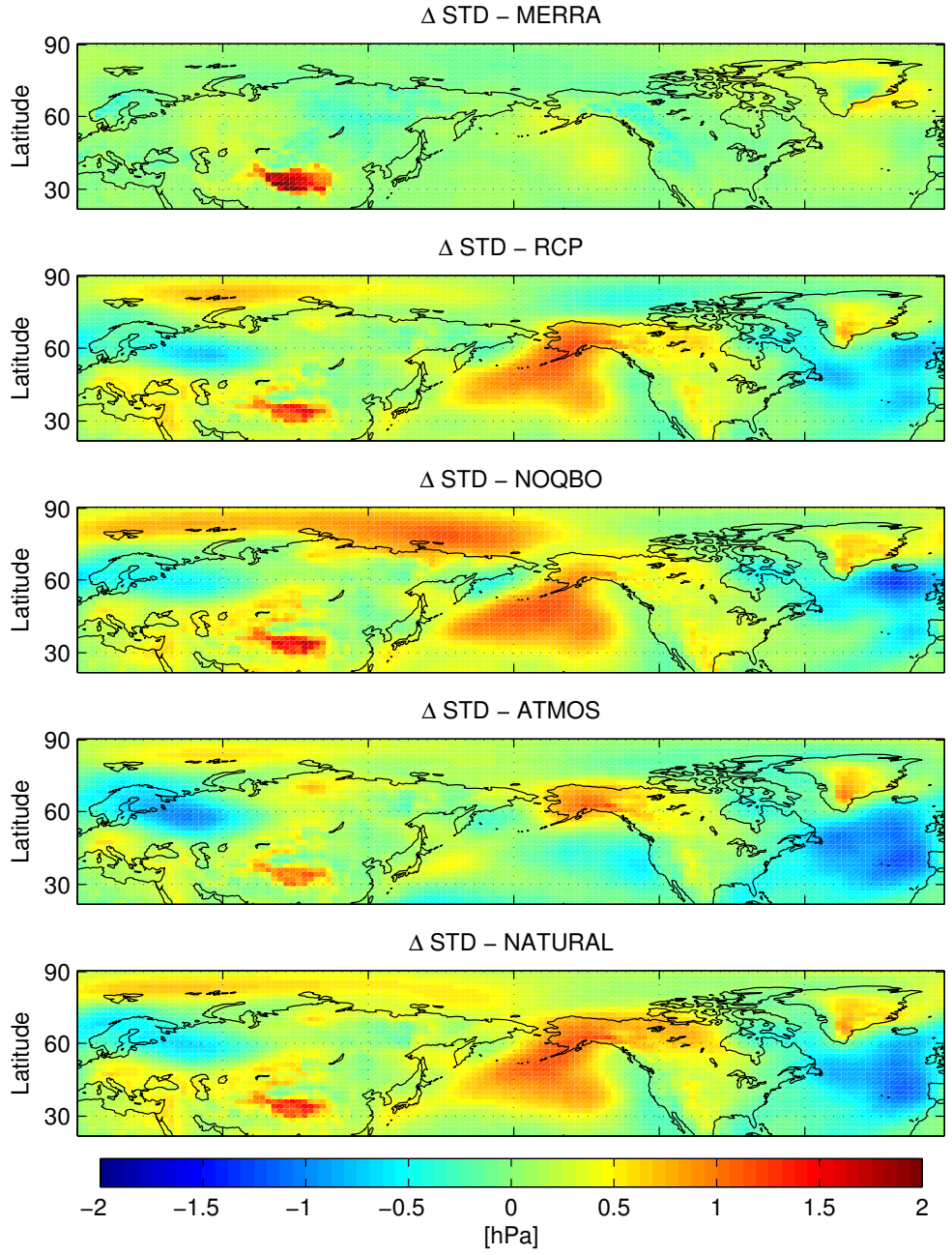

Figure 3.3: The differences between the ERA-Interim standard deviation of the MSLP and MERRA data (top) and all four CESM experiments. Positive values indicate more variation in the respective data set.

experiments. The MERRA data is in agreement with ERA-Interim, featuring only small variations between Greenland and Island and a clear offset in the Himalayan region. The latter one is most likely related to MSLP extrapolation difference between the reanalysis data sets. The CESM experiments generally show less variance in the Atlantic sector and more in the Pacific one. Only experiment ATMOS, which uses a climatological ocean and thus does not experience an ENSO cycle, shows realistic pressure variations in the Pacific. This indicates

that the overestimation of the MSLP variation of the other three CESM experiment might be related to ENSO or other atmosphere-ocean coupling processes. In fact Deser et al. (2011) find CESM overestimating ENSO for the herein used resolution setting.

It is interesting to note that experiment NOQBO shows an increased MSLP variation in the polar region, especially north of Siberia. This can be explained with the Holton-Tan effect (Holton and Tan, 1980, 1982), which describes a more variable northern hemisphere during the QBO_{east} phase. The increased variability is related to reflected planetary waves that are resolved during the QBO_{west} phase. Since experiment NOQBO features solely easterly winds in the equatorial stratosphere (Figure 3.1), planetary waves are constantly reflected towards the pole leading to a constantly perturbed polar vortex. This causes in general a weaker polar vortex, which experiences more frequent stratospheric warmings and thus a more variable polar MSLP. This is in agreement with analysis on the very same CESM experiments performed by Felicitas Hansen (personal communication).

Summarizing, the MSLP is modeled more variable in the Pacific sector, which is most likely related to ENSO, while the Atlantic sector features significantly smaller variations with respect to the reanalysis data.

Regarding the NAM, Figure 3.4 shows the first EOF pattern for ERA-Interim and MERRA data as well as for all CESM experiments. The title indicates the explained variance for each data set. Again, all computations are performed for the longest available time series (ERA-Interim: 1989 - 2010; MERRA: 1979 - 2012; CESM: 50/145 modeling years) and additionally tested for shorter time slices down to 20 years. The depicted patterns are robust for all time slices. In order to validate the processing routines the ERA-Interim and MERRA based results are evaluated upon the NAM index provided by National Oceanic and Atmospheric Administration (NOAA[1]), which is computed in the same way. The results are virtually identical approving the applied routines.

The aforementioned close relation between the NAO and the NAM is evident in the ERA-Interim and MERRA data (Figure 3.4 top). Both feature clear positive pressure anomalies in the north Atlantic and negative anomalies in the mid-latitudes, between 30°and 60°N. The negative pressure anomalies peak in the Pacific and Atlantic sector, with slightly stronger values in the latter one. Both modes explain about 18 % of the total variance. In contrast to the reanalysis data the CESM experiments RCP, NOQBO and NATURAL feature a clearly dominant pressure signal in the Pacific sector. The Atlantic pressure gradient is also modeled, but clearly weaker pronounced. Additionally the CESM EOF pattern show stronger positive anomalies in northern central Asia. Experiment ATMOS yields a more realistic first EOF pattern, underestimating the NAO pressure signal only slightly. However, the positive pressure anomalies in northern central Asia are still present. These differences are clearly related to the

[1] http://www.esrl.noaa.gov/psd/data/climateindices/list/

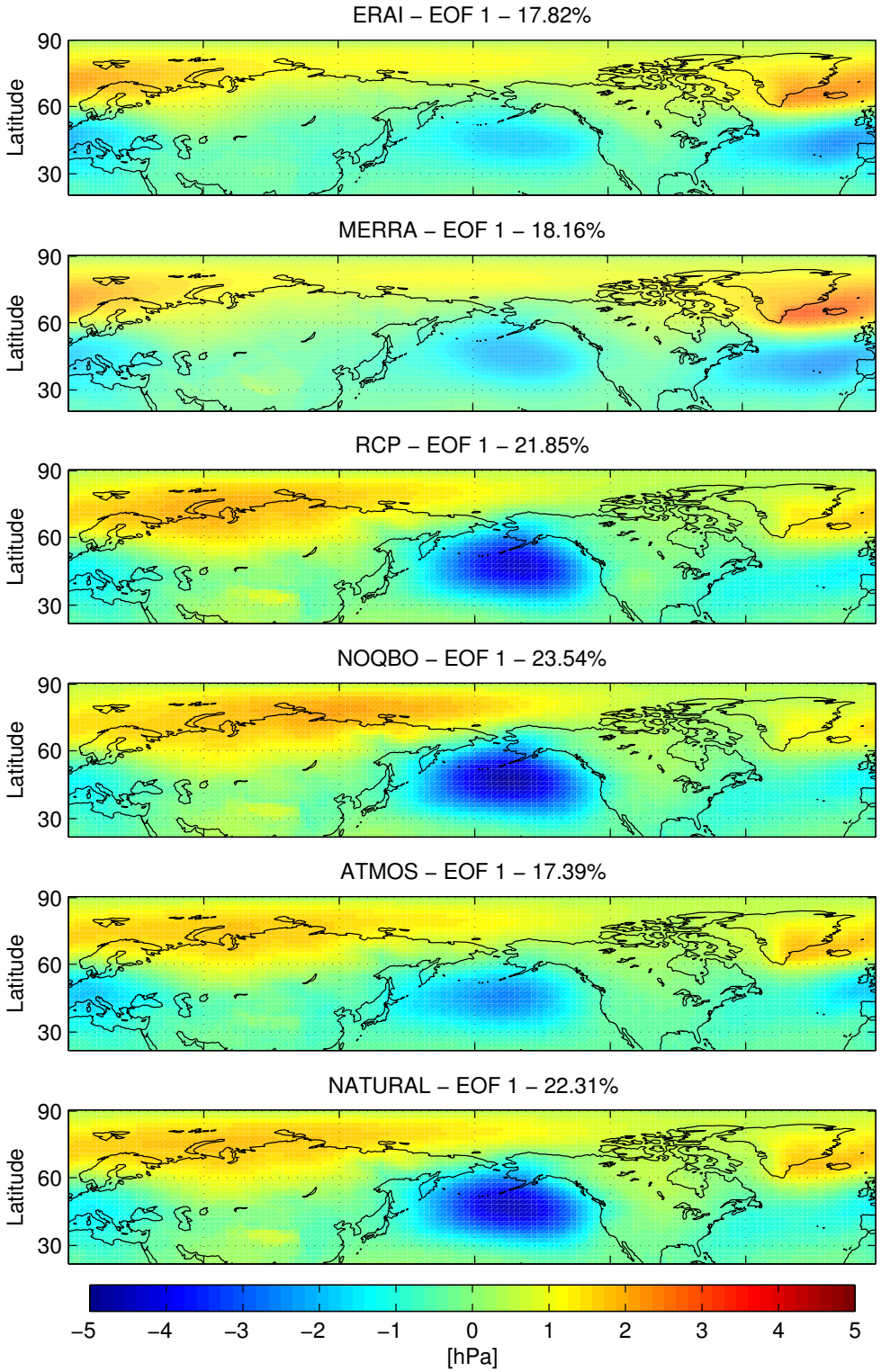

Figure 3.4: First EOF of the MSLP north of 20°N, for ERA-Interim, MERRA and CESM data.

overestimation of the Pacific and the underestimation of the Atlantic MSLP variation, since the first EOF explains the most of the variance.

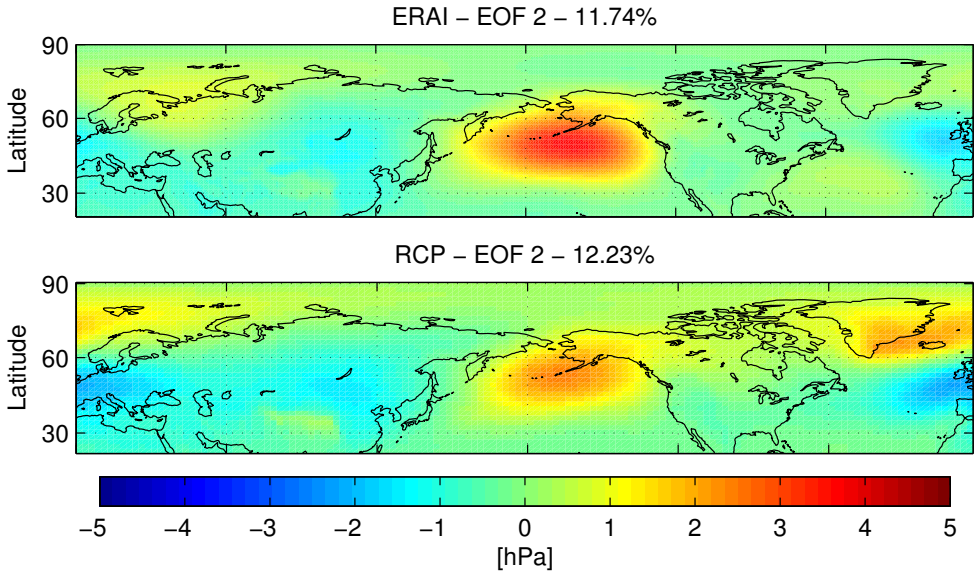

Figure 3.5: Second EOF of the MSLP north of 20°N. The title indicates the data set and the explained variance.

The modeled Pacific pressure system reminds of the Pacific Decadal Oscillation (PDO) pattern (Mantua and Hare, 2002; Hare, 1996). However, since the modeled data is high-passed filtered (7-years) the PDO cannot explain the strong Pacific pattern. The PDO is often described as a long-lived El Niño-like pattern (Mantua and Hare, 2002), indicating ENSO as a possible candidate perturbing the EOF analysis within the modeling domain. In agreement the only experiment prescribing SSTs and thus not featuring an ENSO cycle (ATMOS), shows the strongest similarities to the reanalysis data. Taking this into account as well as the knowledge of CESM overestimating the ENSO cycle for the here used freely coupled model settings, suggests that ENSO dominates the first MSLP EOF of the northern hemisphere especially in the Pacific sector. This is in agreement with the spread of the explained variances of the first EOFs among the modeling studies. Experiment NOQBO neglects an important source of natural variation (QBO), which leaves relatively more variability for other factors, such as ENSO. Consequently the first EOF of this experiment accounts for most variability (23.5%). The first EOFs of experiment RCP and NATURAL explain about the same variance, with a slightly lower value for RCP indicating more energy in smaller scale patterns. All these experiments greatly overestimate the results of the reanalysis data, only experiment ATMOS features a slight underestimation, which is clearly related to the absence of ENSO.

Figure 3.5 shows the second EOF patterns for ERA-Interim and experiment RCP, representing the main differences between the reanalysis data and the modeling results. The second EOF features are somewhat reversed compared to the first EOFs, showing high Pacific variability in the reanalysis data and a NAO-like pattern in the modeled Atlantic region. This clearly indicates the NAM as independent from a significant part of the North Pacific MSLP

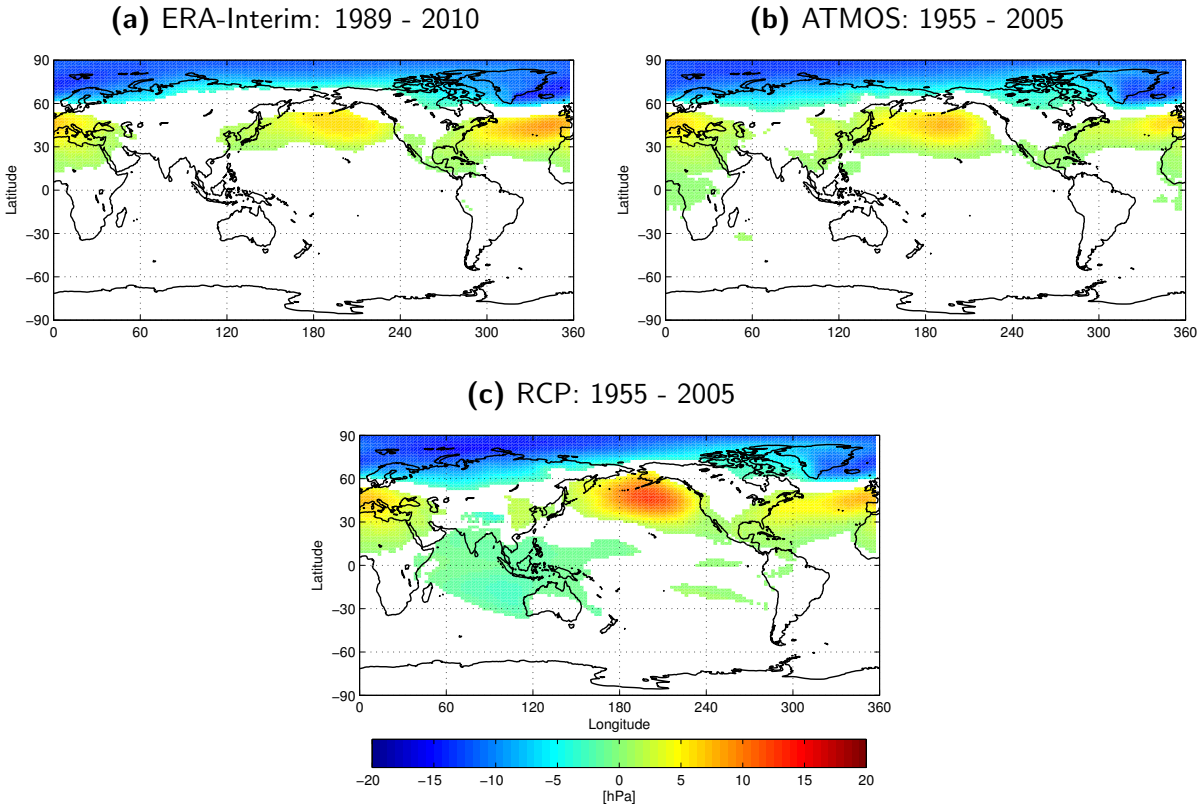

Figure 3.6: Composite Mean Difference of the Mean Sea Level Pressure for NAM_{MAX} minus NAM_{MIN} composites for (a) ERA-Interim data, (b) Experiment.

variation, for the reanalysis data, which is not the case for CESM if the EOF based NAM definition is taken into consideration.

All together it is clear that the principle component of the first EOF for reanalysis and modeled data represent similar but not the same physical processes. Therefore the NAM as a defined physical process cannot be properly described using the mathematical solutions of the EOF analysis, for the CESM models. Consequently another approach describing the NAM has to be chosen. This is projecting the correct EOF pattern based on ERA-Interim data (Figure 3.4 top) onto the whole time series of modeled MSLP. The new time series will again be dominated by the Pacific sector, since CESM accounts more variability in this region. However, the new index will represent the physical processes associated with the NAM rather than a pure mathematical solution.

In order to verify this statement Figure 3.6 shows the composite mean differences (CMDs, see section 2.4.1) of NAM_{max} minus NAM_{min} conditions for ERA-Interim data and experiment RCP for all values exceeding a statistical significance of 99%. The maximum composite consists of all months where the NAM index exceeds one standard deviation, while the minimum composites consist of the reverse for negative values. Figure 3.6a shows again the NAM related circumferencing pressure signal with slightly stronger amplitudes in the Atlantic. Fig-

ure 3.6c shows similar features in the northern hemisphere, including the exaggerated North Pacific signal. However, it is clearly more consistent with the reanalysis data than the related EOF patterns. Additionally to the northern hemispheric signal CESM shows slight negative but significant pressure anomalies in the equatorial Indian ocean. This feature can be attributed to the negative ENSO (La Niña) phase, indicating again the modeled connection between ENSO and NAM. Consequently, this feature is not present in the ATMOS experiment (Figure 3.6b), which has no ENSO cycle.

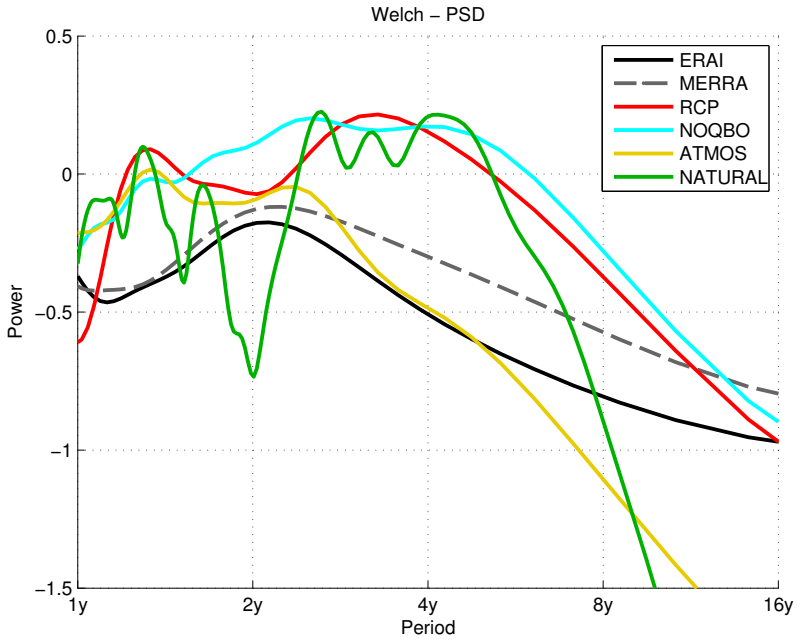

Figure 3.7: Power spectral density of the projected NAM index according to Welch's method for the reanalysis data and all CESM experiments. The 95 % significance is plotted only for ERA-Interim as dotted black lines.

For a better understanding of the temporal behavior of the computed NAM indices, Figure 3.7 shows the power spectral density according to Welch's method. The reanalysis data show most of the power within the range of two years, which is only met by experiment ATMOS. All the other CESM experiments feature the highest energy within the range of two to five years. This again is typical for ENSO, once more indicating the connection.

Summarizing one can say that our CESM experiments appear to exaggerate MSLP variations in the Pacific sector and underestimate the same in the Atlantic. This is related to the overestimation of ENSO, which predominantly affects the Pacific sector, which in turn perturbs the modeled Northern Annular Mode. The only experiment without ENSO (ATMOS) agrees best with the ERA-Interim and the MERRA features.

3.5.2 El Niño Southern Oscillation - ENSO

The El Niño Southern Oscillation (ENSO) is a highly investigated global scale phenomenon that is defined in the equatorial Indo-Pacific, where it is driven by ocean atmosphere coupling effects (Neelin et al., 1998; Chang et al., 2006). It alters precipitation and temperatures on a global scale via teleconnections (Trenberth et al., 1998; Alexander et al., 2002). The warm phase is called El Niño and features positive temperature anomalies in the equatorial east Pacific, causing heavy rain at the Pacific coast of South America. The cold phase is called La Niña and shows negative temperature anomalies in the eastern Pacific and positive precipitation anomalies from southeast Asia to north Australia. Both phases last about 1-2 years, repeating every 3-6 years. La Niña usually lasts a little longer, but is also weaker pronounced (Harrison and Larkin, 1998; Okumura and Deser, 2010). Here, ENSO is represented by the Nino3.4 index, in contrast to other recent studies, which use for example the Multi-Variate ENSO Index (MAI, Wolter and Timlin (1998)).

The capability of CESM to reproduce ENSO is documented by Deser et al. (2011) and summarized in this paragraph. They find a realistic ENSO frequency (3-6 years) and also a realistic variability among the different ENSO events. Further, CESM models the observed longer duration of La Niña events compared to El Niño and also features realistic ocean temperatures. Teleconnection patterns related to temperature and precipitation are well simulated. Nevertheless, CESM still overestimates the overall magnitude of the ENSO cycle by about 30%. The wintertime Aleutian Low is modeled too strong and too persistent lasting into spring. Deser et al. (2011) analyze experiments using all active components, including CAM4 (on 0.9°x 1.25° and 1.8°x 2.5° resolution). Our experiments use WACCM3.5 on the 1.8°x 2.5° resolution, which might imply deviations from the findings of Deser et al. (2011).

The interest of this study lays mainly upon dynamical mass and motion variations that potentially influence the EREs. Thus, we do not compare the standard SSTs, but the ENSO related pressure system. Figure 3.8 shows the MSLP pressure CMD with respect to the Nino3.4 index for (a) ERA-Interim data and (b)-(d) the modeling experiments that use an interactively coupled ocean. Visualized are only signals exceeding 99% statistical significance. Again visualized features are based on the longest available time series and are tested for time slices down to twenty years. The results are robust, solely the significance varies due to changes in the length of the investigated time slice.

The major features agree between all data sets. This includes positive pressure anomalies in the equatorial Indian and western Pacific ocean as well as in the west Antarctic. However, the first-mentioned is constantly modeled too strong while the latter one is always modeled too weak. Negative anomalies are present in the central and eastern Pacific ocean, reaching into mid-latitudes. Further, the northern and southern Atlantic shows negative pressure anomalies in the mid-latitudes. However, there are clear differences, especially regarding the significant

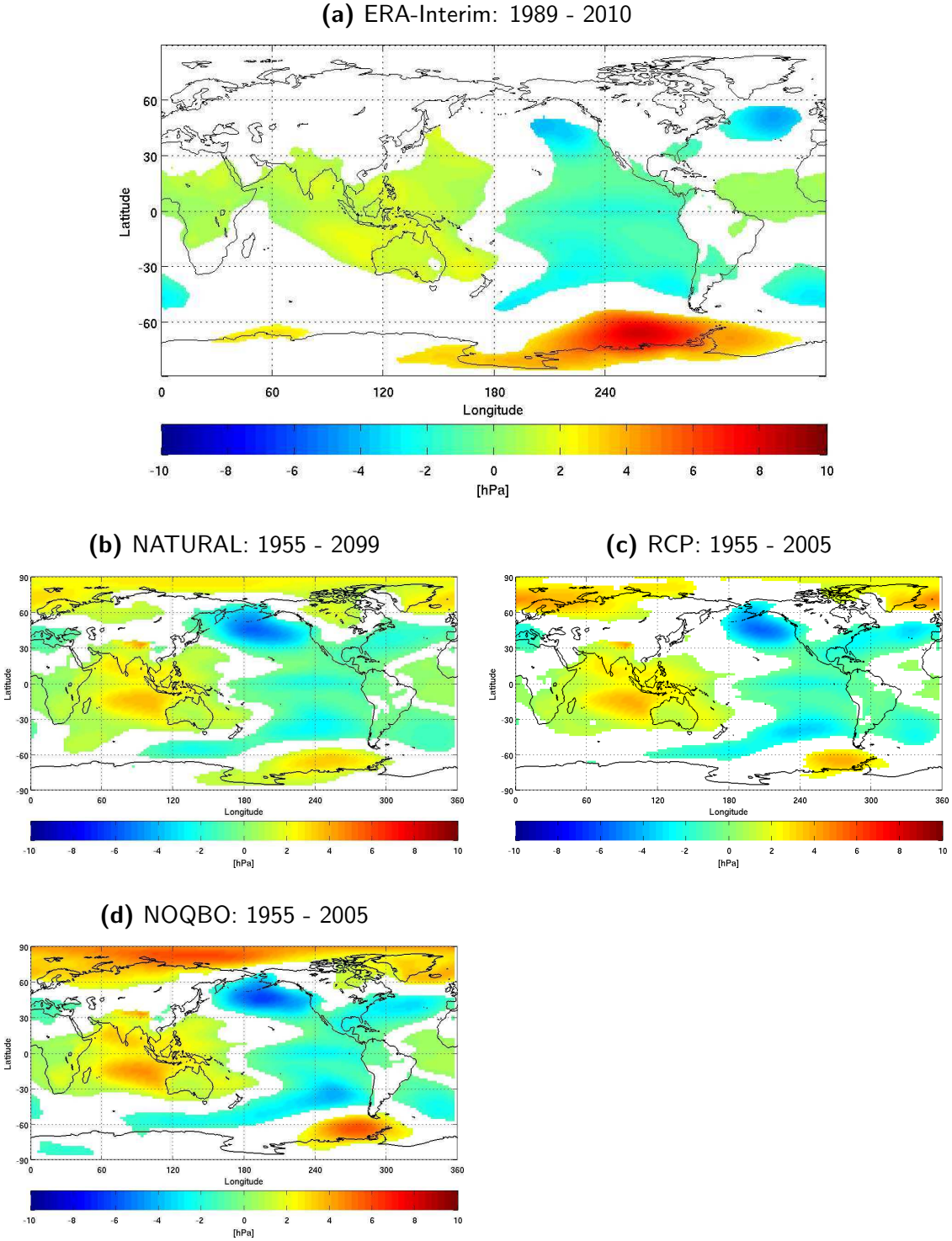

Figure 3.8: Composite Mean Difference of the Mean Sea Level Pressure for El Niño minus La Niña composites, for (a) ERA-Interim data and (b) - (d) all CESM experiments.

values in the northern hemisphere. Here we find positive pressure anomalies at the pole and circumferencing negative values, mainly over the ocean. This indicates a connection between ENSO and NAM that is not present in the ERA-Interim data. This connection again appears

to be strongest in the NOQBO experiment indicating unrealistic coupling effects in the absence of the QBO. As for the NAM, we find in all model experiments the North Pacific pressure anomalies significantly greater than the north Atlantic ones.

Chapter 4

Natural Variations in Stand-Alone Models

The entire work discusses natural and anthropogenic variations of the climate system and its subsystems. Until recently the available computational resources limited the associated modeling studies to the investigation of only one subsystem, for example the atmosphere or the ocean. Substantial work and significant progress has been done on all sides of the modeling community in order to further improve the models towards the observations. However, all stand-alone modeling studies by definition lack the capability of investigating coupling effects between the different systems. The question whether these coupling effects occur and to what extend they are important, especially with respect to natural and anthropogenic climate variation, requires a careful assessment.

In this context, Petrick et al. (2012) investigate the effect of two slightly different atmospheric modeling experiments on the ocean. They find that variations in the equatorial stratosphere propagate through the troposphere to the surface where they do not translate into a significant ocean signal. Despite the absence of such a footprint, further analysis shows that these stratospheric variations alter other modes of climate variations, namely the influence of the solar cycle, which now does propagate into the ocean.

The forthcoming chapter presents the work of Petrick et al. (2012) and can be understood as a pre-study and introduction for the subsequent chapters 5 and 6 which are based on the results of coupled climate models. Basically this study investigates the question of: Why do we need coupled climate models in the context of studying natural and anthropogenic climate variations?

4.1 Introduction

One of the most important sources of natural climate variability is provided by the Sun on different timescales, and its climate influence is under continued discussion. Recently Gray et al. (2010) provided a comprehensive review of solar influences on the climate system. One complication of the solar cycle influence is the (possible non-linear) interaction with the quasi-biennial oscillation (QBO) of equatorial stratospheric winds first noted by Labitzke (1987) and Labitzke and Van Loon (1988). Kodera and Kuroda (2002) introduced the so-called "top-down" mechanism for the stratosphere. This mechanism describes how relatively small UV variations with the 11 year solar cycle in the tropical upper stratosphere can lead to a significantly enhanced dynamical response throughout the stratosphere. Changes in middle atmosphere heating and therefore in ozone production and loss induce changes in the meridional temperature gradients, which in turn alter the propagation properties for planetary waves and lead to circulation changes. However, the effects of the solar cycle are not confined to the stratosphere. Further down, e.g., White et al. (1997) noted a small decadal to interdecadal solar cycle effect in globally averaged Sea Surface Temperatures (SSTs). Later, Roy and Haigh (2010) found in agreement with other authors a significant solar cycle response during boreal winter in the surface pressure (i.e., a weakening of the Aleutian Low and a northward shift of the Hawaiian High during solar maximum (S_{max})). On the Southern Hemisphere (SH) van Loon and Meehl (2011) found significant positive Sea Level Pressure (SLP) anomalies in the Southeast Pacific during S_{max} conditions.

Most modeling studies have difficulties to reproduce the pattern and magnitude of the observed climate system response to the solar cycle. Meehl et al. (2009) suggested that in addition to the "top-down" mechanism a so-called "bottom-up" mechanism takes place in which the ocean feedback amplifies the solar cycle effect. Taking into account the middle atmosphere and the ocean improves the amplitude of the modeling results. The importance of other sources of natural variability (e.g., the QBO) on the climate system's solar cycle response is for example discussed in a model study by Matthes et al. (2010).

To shed more light on the response of the ocean to the "top-down" mechanism, we extend the "top-down" investigation in the atmosphere by adding a dynamic ocean model. Therefore we use two 110-year model experiments of NCAR's Whole Atmosphere Community Climate Model (WACCM3.19), a fully coupled chemistry-climate model (CCM, Garcia et al. (2007)), to force GFZ's Ocean Model for Circulation and Tides (OMCT, Thomas et al. (2001)), an Ocean General Circulation Model (OGCM). Both atmospheric experiments include a time-varying solar forcing, but only one includes a (prescribed) QBO (Matthes et al. (2010)). In order to isolate the "top-down" effect, our atmospheric simulations used climatological SSTs. The modeled atmospheric data are then used to force the ocean model. This contrasts the experimental design of Meehl et al. (2009), who compare three different model settings:

WACCM stand-alone (for analyzing the top-down mechanism); WACCM coupled to an ocean (combined top-down and bottom up); and CAM coupled to an ocean (bottom-up). All three model studies do not include a QBO. The present study instead focuses solely on the signal that propagates from the stratosphere through the troposphere into the ocean, excluding all ocean feedbacks, i.e. "bottom-up" mechanism. The goal is to investigate whether prescribed stratospheric winds, i.e. the QBO, significantly affect not only the stratospheric, but also the tropospheric and the oceanic response to the solar cycle.

This chapter is structured as follows: the description of the dynamic ocean model as well as the experimental design and the analysis methods, are given in section 2. Section 3 and 4 describe the results of the model experiments, in particular the impact of the QBO and the solar cycle on the atmosphere and their subsequent effects on ocean dynamics. Sections 5 and 6 summarize and conclude the results.

4.2 Experimental Design

4.2.1 Experimental Design

We carried out two 110-year simulations with the OMCT (see Table 3.1). The atmospheric forcing for these long-term OMCT runs came from two 110-year simulations of NCAR's Whole Atmosphere Community Climate Model (WACCM), version 3.19, as described by Matthes et al. (2012). WACCM is a fully-interactive Chemistry-Climate Model (CCM) resolving the Troposphere, the Stratosphere, and the Mesosphere up to the Thermosphere [5.1×10^{-6} hPa (~ 140 km)] (Garcia et al., 2007). WACCM3 is an expanded version of the Community Atmospheric Model, Version 3 (CAM3) and includes all of the physical parametrization of CAM3 (Collins et al., 2006). The detailed neutral chemistry model for the middle atmosphere is based on the Model for Ozone and Related Chemical Tracers, Version 3 (MOZART3) and accounts for radiatively active gases affecting heating and cooling rates and hence dynamics (Kinnison et al., 2007). The horizontal resolution is 1.9° x 2.5° and 66 vertical levels are included. Because WACCM is not able to generate an internal QBO, modeled tropical stratospheric zonal winds are relaxed toward observations in the equatorial band from 22° N to 22° S (Matthes et al., 2010). Two transient 110-year simulations of WACCM were carried out under natural forcings only, one solely with the 11-year solar cycle, i.e. a varying solar spectral irradiance (A^{SC}), and the other one with both a solar cycle and a QBO (A^{SC}_{QBO}). As a proxy for the solar cycle irradiance, we use the f10.7 cm solar radio flux. Geomagnetic activity is accounted for by the kp-index. All other natural and anthropogenic forcings were held constant at 1995 conditions (i.e. climatological monthly varying SSTs, GHGs, and ODS). No volcanic effects are included. Since we do not have solar cycle and QBO observations for 110 years, the observed f10.7cm

solar radio flux, the kp-index as well as the equatorial winds in the tropical lower stratosphere from 1953 to 2004 were extended with two repetitions of the years from 1962 to 2004 (Matthes et al., 2012). We choose the year 1962 because the solar cycle and the QBO show similar phases as in 2004, allowing a smooth continuation. These two atmospheric simulations were used to force the dynamic ocean model in order to study the oceanic sensitivity to the prescribed natural forcings, yielding experiments O^{SC} and O^{SC}_{QBO}. Note that in the experiments presented here, no freshwater fluxes were accounted for.

Rind et al. (2008) find a partly statistically significant solar cycle related precipitation reduction near and south of the equator of about 1 millimeter per day for August and an increase in precipitation north of the equator especially above southern Asia with a similar amplitude. The precipitation effect is spatially localized and variable over the year. Huang and Mehta (2005) indicate that precipitation changes of about 1.5 m / yr on interannual timescales have the potential to influence the baroclinic circulation of an ocean. Based on the results from Rind et al. (2008) with Huang and Mehta (2005) we expect solar cycle related precipitation changes to have only minor effects on our modeling results, especially since we investigate multidecadal monthly mean results.

4.2.2 Methods and Data

We analyze monthly mean model data, which are deseasonalized by subtracting the long-term monthly means from each month of the time series. We then use the composite mean differences (CMD, cf section 2.4.1) between the solar maximum (S_{max}) minus the solar minimum (S_{min}) months to visualize the influences of the solar cycle. Here solar maximum and minimum month are defined according to Matthes et al. (2012), with S_{max} : f10.7cm solar radio flux > 150 solar flux units ($10^{-22}\frac{W}{m^2 Hz}$, hereafter sfu) and S_{min}: f10.7cm solar radio flux < 90 sfu. The composites include 348 S_{max} and 391 S_{min} months. For additional confirmation of our results we computed the correlation between the f10.7 and the model output. The difference between the correlation and the CMD results in terms of significance patterns is marginal; the correlation of the resulting spatial patterns of both methods exceeds 90%. The 99% statistical significance is determined with a Student's t-test, taking into account the auto-correlation by reducing the degrees of freedom accordingly. The significance patterns as well as the anomalies are also verified by bootstrap analysis, using 1000 samples. All three methods yield very similar signals and significances.

4.3 QBO Footprint and Solar Signal in the Atmosphere

In order to investigate the response of the atmosphere and the ocean to varying natural forcings such as the QBO and the solar cycle, we start analyzing the effect of the QBO, using the

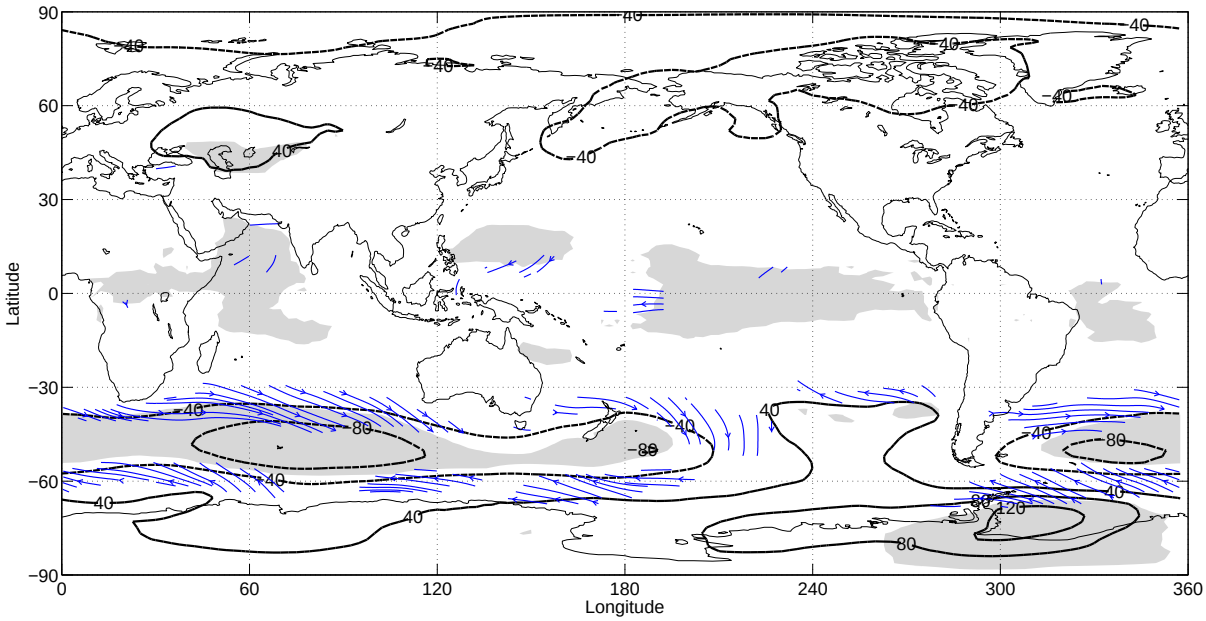

Figure 4.1: Composite mean difference between $QBO_{west} - QBO_{east}$ of surface pressure in Pa. Shaded regions denote 99% significance. Arrows represent 99% significant surface wind anomalies. The significant surface wind anomalies in the southern hemisphere reach an amplitude of $0.75\frac{m}{s}$ in the South Atlantic and $0.5 - 0.6\frac{m}{s}$ in the South Pacific and Indian ocean.

atmospheric A^{SC}_{QBO} and the corresponding oceanic O^{SC}_{QBO} experiment. Afterward, we compare the solar cycle response of this realization to the solar cycle only (A^{SC}) experiment. Fig. 4.1 shows the CMD in atmospheric surface pressure where the QBO signal has been lagged by 4 months. A lag of 4 months yields the most significant signal and agrees with Marsh and Garcia (2007), who found that the correlation between 52 hPa temperature and ozone and the surface NINO3.4 index in WACCM peaks at a lag of 4-5 months. They also indicate that this is the model-related coupling time between the stratosphere and the surface troposphere.

In Fig. 4.1 we find significant negative pressure anomalies in the SH, between $30°S$ and $60°S$, peaking in the South Atlantic and South Indian Ocean with a maximum amplitude of 100 Pa. In the southern polar region we find positive pressure anomalies for $QBO_{west} - QBO_{east}$ of more than 120 Pa, significant mainly in the vicinity of the Weddel Sea. The pressure anomalies in the SH show a negative SAM-like pattern and are associated with significant wind anomalies, represented by blue stream lines. The wind anomalies shown are significant at the 99% level and have an amplitude of about $0.7\frac{m}{s}$. However, these significant atmospheric surface anomalies do not propagate into the ocean (not shown), because the signal amplitude is very fast and its amplitude is too weak.

We also find significant pressure anomalies in the equatorial Pacific, Indian and Atlantic oceans. However, these signals are very weak, with an maximum amplitude of about 10 Pa. Because the variability of the deseasonalized equatorial surface data is low, small differences between the QBO phases are significant. In contrast the NH shows stronger negative anomalies

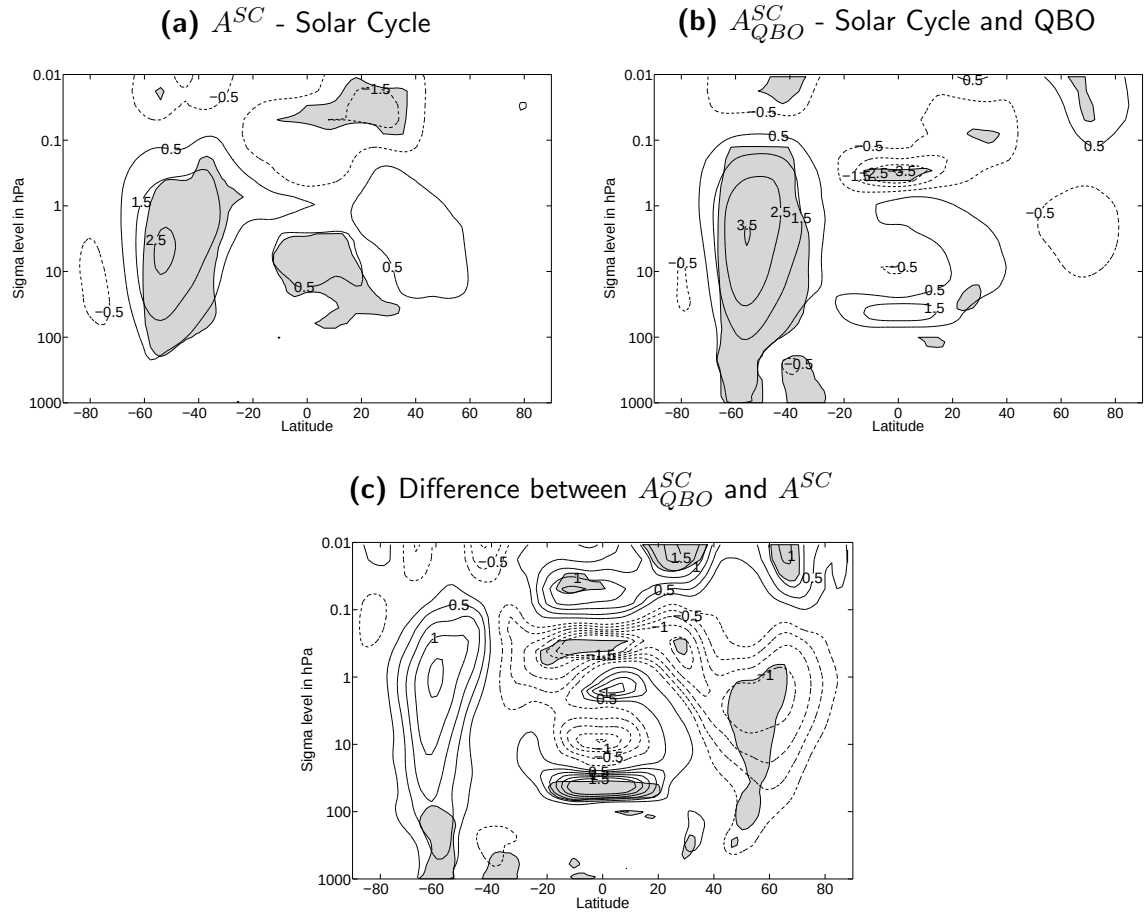

Figure 4.2: Annual mean composite mean difference between $S_{max} - S_{min}$ of zonal mean zonal wind for a) A^{SC}, b) A^{SC}_{QBO}, and c) A^{SC}_{QBO} - A^{SC}. Shaded regions denote 99% significance. Contour lines denote anomalies in $\frac{m}{s}$, negative values are dashed.

of up to 50 Pa, which are, however, not significant due to the high variability of the signal here.

Summarizing, we find a significant atmospheric surface signal for the lagged $QBO_{west} - QBO_{east}$ CMD, which do not propagate into the ocean. We further concentrate on the solar cycle response of our modeled atmospheres for both the solar cycle only (A^{SC},O^{SC}) and the solar cycle plus QBO (A^{SC}_{QBO},O^{SC}_{QBO}) experiments.

4.3.1 Solar Signal in the Zonal Mean Zonal Wind considering the QBO

The CMD of the atmospheric zonal mean zonal wind with the solar cycle is shown in Figure 4.2 for a) the WACCM simulation with solar cycle only (A^{SC}) and b) the WACCM simulation with solar cycle and nudged QBO (A^{SC}_{QBO}). Both figures differ especially in the SH troposphere. The A^{SC} run shows significant positive anomalies mainly above 100 hPa, peaking in southern

mid-latitudes between 30° and 60° S and at the equatorial regions at 10 hPa. Negative values are present in the equatorial mesosphere above 0.1 hPa (Figure 4.2a).

Prescribing the QBO leads to a significant strengthening of the atmospheric solar cycle response especially on the SH troposphere (Figure 4.2b). Now we find stronger positive anomalies, reaching from the lower mesosphere / upper stratosphere down to the surface between 50° and 60° S. The amplitude of the positive anomalies increases by about $1\frac{m}{s}$ to a maximum of about $3.5\frac{m}{s}$. Additionally significant negative values are present in the troposphere between 25° and 40° S. The significant positive anomalies in the equatorial stratosphere vanishes because the QBO nudging zone is located here. One can see a QBO signature in the equatorial stratosphere, which indicates that the solar cycle composite does not filter the QBO signal entirely. The reason why we see a QBO footprint in the solar cycle composite is related to the fact, that during S_{max} conditions (total of 348 months) there are 144 QBO_{west} and 124 QBO_{east} months, or in other words a slight tendency towards the QBO_{west} phase. During S_{min} conditions (total of 391 months) we find 143 QBO_{west} and 156 QBO_{east} months, indicating a slight tendency towards the QBO_{east} phase. Therefore, the $S_{max} - S_{min}$ composite shows slight $QBO_{west} - QBO_{east}$ features. This does not indicate a phenomenological connection between the solar cycle and the QBO, since both time series are prescribed in this modeling study.

The weak positive anomalies in the northern stratosphere found for the A^{SC} experiment (Figure 4.2a), turn into weak negative anomalies when prescribing the QBO (Figure 4.2b); both are not significant. Comparing both solar cycle responses (Figure 4.2c: A^{SC}_{QBO} - A^{SC}) with each other reveals that the increase of the zonal mean zonal wind in the SH is only significant for the troposphere, but not for the stratosphere. This means that an increase of zonal mean zonal wind of about $1\frac{m}{s}$ at the height of 1 hPa is not significant, while the increase of $0.4\frac{m}{s}$ in the troposphere is significant for both cases: $S_{max} - S_{min}$ (Figure 4.2b) and for $A^{SC}_{QBO} - A^{SC}$ (Figure 4.2c). Since we have about 10 solar cycles in the 110 years of model output, the signal to noise ration could be further improved by continuing the experiment. This may increase the significance of certain patterns, for example the strengthening of the southern stratospheric jet.

The annual mean zonal mean zonal wind results of experiment A^{SC}_{QBO} (Fig. 4.2) compare well to the analysis of Kuroda and Kodera (2005), who found similar patterns in ERA40 reanalysis data from October through December (OND). These months dominate the annual mean response of the SH (shown in Figure 4.2). Thompson and Wallace (2000) found the SAM coupled with the stratospheric circulation during these months. Our A^{SC}_{QBO} experiment also shows the strongest stratosphere-troposphere coupling during OND, whereas the coupling in the A_{SC} run is weaker. In Figure 4.3 we provide OND zonal mean zonal wind for the A^{SC} and A^{SC}_{QBO} experiment. This indicates that prescribing the QBO improves the atmospheric

solar cycle response compared to observations, as the experiment without QBO does not show these features.

On the NH both experiments (A^{SC}_{QBO},A^{SC}) show no significant solar cycle response. The NH experiences more interannual variability possibly overwhelming a solar cycle response. Greater land-sea contrast in the NH causes more planetary wave activity which disturb the polar vortex. Similarly, Kodera and Kuroda (2002) found the interannual polar night jet variability substantially larger in the NH compared to the SH. According to the Holton-Tan effect (Holton and Tan (1980) and Holton and Tan (1982)) the NH is more variable during QBO_{east} phase because planetary waves are reflected poleward causing more disturbance in the extratropical stratosphere. In the A^{SC} experiment with no prescribed QBO, we find climatological easterly winds in the equatorial stratosphere. These easterly winds tend to reflect the planetary waves which means a constantly more disturbed polar vortex. Thus we would expect a more variable extratropical stratosphere and hence a smaller and less significant solar cycle response. In fact the A^{SC} experiment shows a weaker zonal mean zonal wind signal in the mid- to high-latitude troposphere compared to the A^{SC}_{QBO}.

To summarize, we find a significant dynamic response of the atmosphere to the solar cycle, which only propagates to the surface on the southern hemisphere if the QBO is prescribed. The next questions are: How does the atmospheric reaction to the solar cycle looks like at the Earth's surface? And, does this dynamic atmospheric surface state translates into an oceanic response?

(a) A^{SC} **(b)** A^{SC}_{QBO}

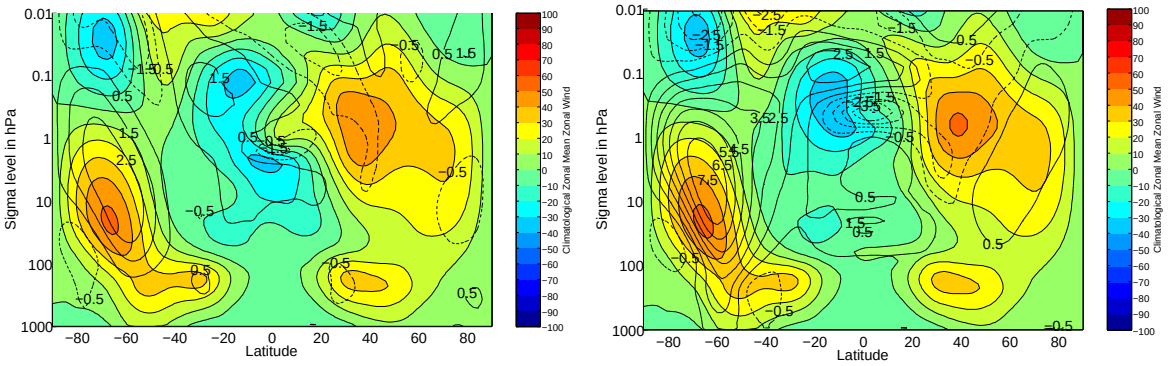

Figure 4.3: Colored contours show the average zonal mean zonal wind for October through December for (top) solar cycle only (A^{SC}) and (bottom) solar cycle plus QBO (A^{SC}_{QBO}) experiment. Differences are especially present in the equatorial stratosphere, where the QBO nudging takes place. The overlaying black contour lines show the composite mean difference between solar maximum minus solar minimum for October through December. The solar cycle response and the stratosphere-troposphere coupling are clearly stronger in (A^{SC}_{QBO}) (Figure S2).

4.3.2 Solar Signal at the Surface Atmosphere considering the QBO

As shown in Figure 4.2b, nudging QBO winds in the stratosphere influences the zonal mean zonal winds from the stratosphere down to the surface, especially in the SH. The corresponding surface pressure anomalies as well as significant surface wind vectors are shown in Figure 4.4b. Here, the surface pressure anomalies show a positive SAM-like pattern, including negative south-polar anomalies and positive annular anomalies in southern mid-latitudes, with an amplitude of up to $\pm$ 1.3 hPa, which is between 20 % and 35 % of the local standard deviation of the deseasonalized monthly mean data. The most pronounced and significant anomalies in mid-latitudes appear in the southern Indian (around 90° E) and in the southern Pacific Ocean (around 150° W). The two positive pressure anomalies correspond to anticyclonic, counterclockwise winds, whereas the large polar pressure low induces cyclonic winds at high southern latitudes (south of 60° S). The wind anomalies are between $0.5\frac{m}{s}$ and $0.9\frac{m}{s}$ (i.e. 20 % to 30 % of the local standard deviation), with the maximum located around 60° S. As already stated above, the spatial pattern of the composite mean difference and the correlations, as well as their spatial significance, are very similar.

The solar cycle only experiment (A^{SC}) differs significantly from the experiment with solar cycle and QBO(A^{SC}_{QBO}): The surface pressure anomalies for S_{max} minus S_{min} (Figure 4.4a) are generally smaller and less significant than when the QBO is included (Figure 4.4b). Instead of the strong SAM-like pattern as seen in the A^{SC}_{QBO} experiments, significant positive anomalies appear southwest of Australia as well as in the subtropical South Atlantic and Pacific. Stronger but not significant negative anomalies occur between South America and the Antarctic and over Siberia. The smaller amplitude and the more localized spatial pattern (compared to A^{SC}_{QBO}, Figure 4.4b) suggest a weaker atmospheric impact on the ocean by the atmosphere when the solar cycle is the only source of natural variability.

Roy and Haigh (2010) analyzed 150 years of DJF SLP from the Hadley Centre HadSLP2 dataset and found a comparable solar cycle footprint to our A^{SC}_{QBO} experiment in the SH. They also found negative pressure anomalies at the South Pole, while the southern mid-latitudes show positive anomalies. Their DJF signal was not significant, but compares well in shape to our non-significant DJF signal in A^{SC}_{QBO} experiment. For the annual mean we find weaker but significant amplitudes (Fig. 4.4b) compared to DJF from Roy and Haigh (2010). The equatorial regions as well as the NH show substantial differences: Roy and Haigh (2010) found for DJF a northward shift of the Hawaiian High and a weakening of the Aleutian Low, the latter is in agreement with van Loon and Meehl (2011). In contrast to these observational studies, our model simulations do not show significant signals in the NH, neither for DJF nor for the whole time series. We speculate that the reasons for this dissonance relate mainly to two facts: a) an incorrect modeling of the atmospheric planetary waves, especially important on the NH; and b) our atmospheric experiments are forced with climatological SSTs, omitting any ocean

feedback and interannual variability, e.g. ENSO. We therefore investigate a pure and idealized "top-down" solar cycle response of the atmosphere and the ocean. The latter indicates the importance of atmosphere-ocean coupling. In the following we exemplarily show, how changes in the middle atmosphere can have a significant impact on the oceanic circulation.

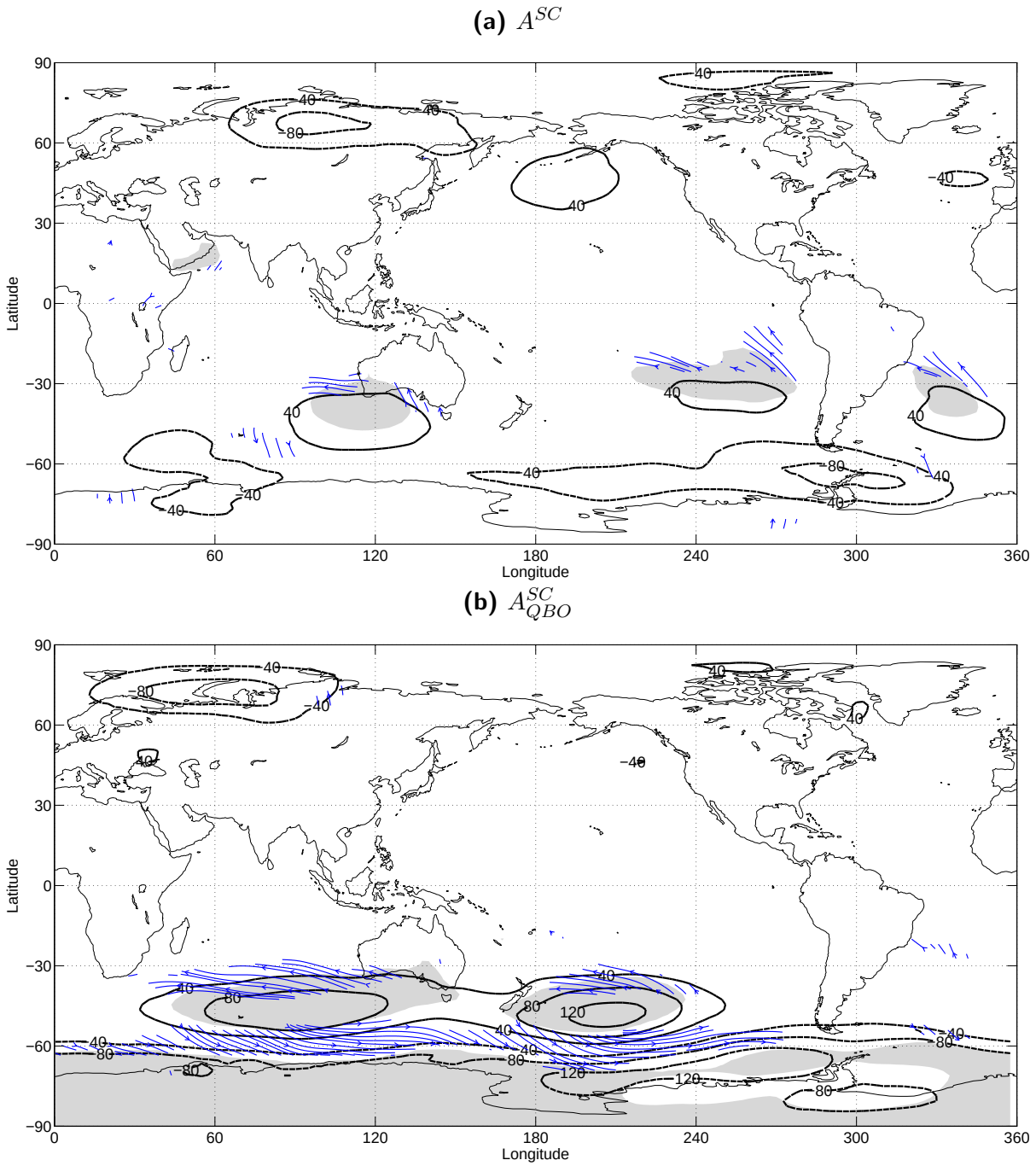

Figure 4.4: Same as Figure 4.2, but for atmospheric surface pressure in Pa for a) A^{SC} and b) A^{SC}_{QBO}. Arrows denote 99% significant wind anomalies. The maximum wind anomalies for a) reach $0.5\frac{m}{s}$ in the South Atlantic, while for b) amplitudes of up to $0.9\frac{m}{s}$ occur around 60° S.

4.4 Solar Signal in the Ocean considering the QBO

The analysis of the modeled oceanic reaction (O^{SC}) to the atmospheric forcing (A^{SC}) yields, as expected, a weak and non-significant response (not shown). We therefore focus our further analysis in this section on the ocean response (O^{SC}_{QBO}) to the more realistic atmospheric forcing, which includes the solar cycle and a nudged QBO (A^{SC}_{QBO}). We focus on the SH since the surface atmospheric forcing anomalies are strongest here (cf. Figure 4.4b). Figure 4.5a shows the solar cycle response of the ocean for the sea surface heights (SSH) and the oceanic surface currents. Shaded regions as well as streamlines show where the signal exceeds 99% statistical significance. Note that lagging the data does not enhance the signal. The shown oceanic surface current anomalies and SSH perturbations (Figure 4.5a) correspond well with the atmospheric surface forcing (Figure 4.4b). The maximum SSH response appears in the southern Indian and southern Pacific Ocean around 50° S. The corresponding current anomalies frame the SSH signal. The significant SSH anomalies vary between 2 and 6 cm, representing 20 to 45 % of the local standard deviation of the monthly mean deseasonalized ocean data. On a decadal timescale we find significant surface atmospheric wind stress anomalies transferring momentum into the ocean (Figures 4.4b and 4.5). Due to the Coriolis force, wind-generated oceanic surface currents deviate toward the left in the SH. This deviation toward the left continues from ocean layer to ocean layer. The vertical integral gives the net effect of the mass transport, which is perpendicular to the original wind stress and thus points to the center of the positive surface pressure anomalies. Summarizing we find the anticyclonic wind anomaly patterns (Figure 4.4b, experiment A^{SC}_{QBO}) inducing convergent oceanic surface currents (Figure 4.5a, experiment O^{SC}_{QBO}). This oceanic water convergence causes an increase in SSH at the center as well as a downwelling. Thus we find counter intuitive positive SSH anomalies in the regions of positive surface pressure anomalies (cf. Figures 4.4b and 4.5), which is the case during S_{max}. Boening et al. (2011) found a similar phenomenon, though not related to the solar cycle, in the Southeast Pacific Ocean in November 2009 analyzing satellite altimetry and GRACE gravity field data. Here, an exceptionally persistent atmospheric high pressure field and the associated anticyclonic wind forcing caused anomalous ocean currents, leading to oceanic convergence (positive SSH anomalies) toward the atmospheric high pressure field. This observation is in good agreement with our modeling results.

In Figure 4.5b we show significant SST anomalies and the same oceanic surface current anomalies as in Figure 4.5a. We find a variety of significant positive and negative temperature anomalies, with an amplitude exceeding $\pm$ 0.1 K. The significant temperature anomalies explain between 20 and 45 % of the local standard deviation of the monthly mean deseasonalized ocean data. The shown anomalies cannot be attributed to atmospheric temperature anomalies and thus relate to a change in the oceanic surface state. In general we find positive temperature anomalies on the east side of the positive pressure anomalies and negative anomalies

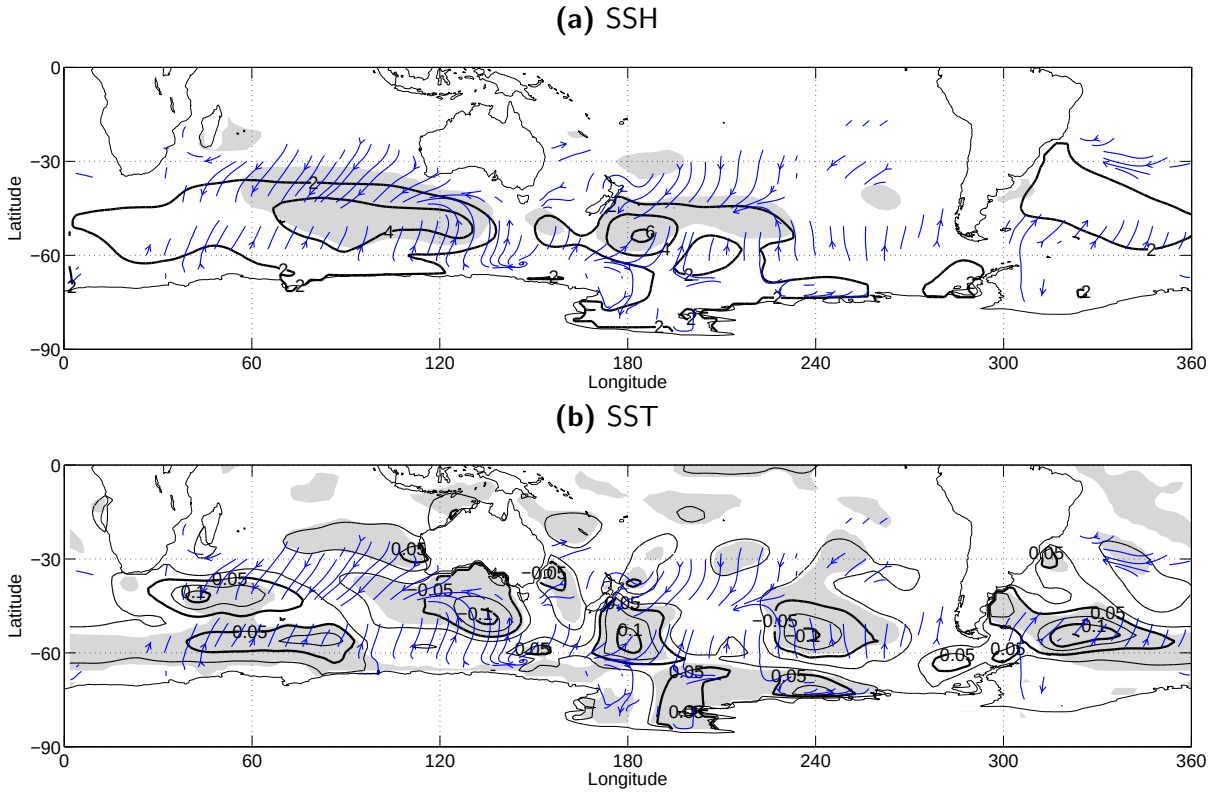

Figure 4.5: Annual mean composite mean difference between $S_{max} - S_{min}$ of a) oceanic sea surface height (SSH) anomalies in cm and b) sea surface temperature (SST) anomalies in K for O^{SC}_{QBO}. Arrows denote 99% significant current anomalies, with maximum amplitudes of $1.2\frac{cm}{s}$ in the southern Pacific.

on the west side (cf. Figure 4.4b). This can be explained with the general anti-clockwise atmospheric wind anomalies and the associated ocean current anomalies. Both bring warmer water polewards on the east side and cooler water equatorward on the west side. The question whether SST anomalies of a tenth of a K are sufficient to perturb the atmosphere significantly cannot be answered with our experiments and thus remains open for further studies.

4.5 Summary

We used two atmospheric experiments from the chemistry-climate model WACCM, one with solar cycle only forcing (A^{SC}) and one with solar cycle and a nudged QBO (A^{SC}_{QBO}) to force the ocean general circulation model OMCT for 110 years. We first investigated the influence of the QBO on atmospheric near-surface conditions and found a significant QBO signal in the surface pressure, which was accompanied by significant atmospheric surface wind field anomalies. However, this change in the atmospheric forcing did not translate into an oceanic response. This could be related to a) the small magnitude of the perturbation and b) the fast changing QBO signal (especially during short and strong easterly wind phases) to which the

ocean cannot adjust that fast. We further investigated the effect of the QBO in combination with the solar cycle. We find that the presence of a QBO alters the solar cycle footprint in the northern stratosphere and strengthens it in the SH down to the surface (at around 50° S to 60° S), where positive zonal mean zonal wind anomalies reach the surface (Figure 4.2b) during S_{max}. This agrees well with the findings of Kuroda and Kodera (2005), who found positive zonal mean zonal wind anomalies especially from October to December during S_{max}. The results from the experiment with solar cycle and QBO (A^{SC}_{QBO}) deviate from the solar cycle only experiment (A^{SC}), where the solar cycle response is confined to the stratosphere only (Figure 4.2a). In the more realistic experiment with time-varying solar cycle and QBO (A^{SC}_{QBO}), we find in agreement with van Loon and Meehl (2011), significant surface pressure anomalies where positive SAM anomalies occur during S_{max} (Figure 4.4b). Roy and Haigh (2010) found similar but not statistically significant surface pressure anomalies. The associated atmospheric wind anomalies (Figure 4.4b) translate into oceanic surface current anomalies (Figure 4.5), which in the SH deviate left due to the Coriolis force. The transfer of momentum from the surface atmosphere to the surface ocean continues into deeper ocean layers (not explicitly shown). The net effect of the transport is perpendicular to the initial wind forcing in the SH pointing toward the center of the positive surface pressure anomaly of an anticyclonic wind field (see Figure 4.4b). This leads to the convergence of ocean mass and the counter intuitive increase of SSHs in regions of positive surface pressure anomalies. According to Wunsch and Stammer (1997) one would expect that the ocean adjusts inverse barometrically such that the sea level rises in areas of low atmosphere pressure and falls in areas of high atmospheric pressure. However, we find an oceanic mass convergence, which is induced by an anticyclonic wind field. Boening et al. (2011) found a similar phenomenon in the Southeast Pacific ocean in November 2009, where a persistent atmospheric high pressure field caused positive SSH anomalies.

Furthermore, even though the presence of a QBO generally improves the atmospheric simulation, the nudging is also continuously perturbing an otherwise free-running model. As such, it prevents an atmospheric feedback into the nudging zone, for example via planetary waves. Nevertheless, a solar cycle signal at the surface atmosphere is only present in combination with a prescribed QBO. The question, whether this feature still occurs with an internally generated QBO, remains to be answered. However, we do find that changes in the middle atmosphere have the potential to influence the ocean surface and deeper layers on decadal timescale creating an integrated ocean mass convergence which is visible as positive SSH anomalies. Taking this into account leads to the question, whether the perturbed ocean feeds back to the atmosphere, and whether this feedback enhances or mitigates the solar cycle footprint in the atmosphere. We assume that a possible feedback from the ocean into the atmosphere will not be induced by the shown SSH anomalies of a few cm (Fig. 4.5). It is more likely that the

atmospherically induced ocean current anomalies impact the atmosphere indirectly, by altering the SSTs. The here-shown SST anomalies of a tenth of K appear to be rather small, but they represent up to 40 % of the standard deviation of the local monthly mean deseasonalized SSTs in our model. Due to the idealized character of our model study, the physical interpretation of this is limited. The scope of this analysis is to show that changes in the middle atmosphere effect the troposphere and even the ocean significantly, despite the small amplitudes. Consequently, comprehensive Earth System modeling studies should include models resolving the middle atmosphere (including the QBO) as well as a coupled ocean general circulation model.

Our experiments show that processes in the middle atmosphere (e.g. a transient prescribed QBO) can modulate the solar cycle response of the stratosphere. In our simulations we find that the insertion of the QBO significantly weakens the solar cycle response of the northern jet. Further we find a strengthening of the jet in the SH, which is significant only in the troposphere (fig. 4.2c). The extension of the solar cycle response of the southern jet from the stratosphere into the troposphere indicates increased stratosphere-troposphere coupling in the A^{SC}_{QBO} experiment. To summarize, the insertion of the QBO alters the "top-down" mechanism in the NH and it strengthens it in the SH, where we also find changes in the troposphere which reach the surface (wind anomalies, fig. 4.4b). Finally these atmospheric surface wind anomalies alter the surface and deeper ocean dynamics as well as the SSHs. Moreover, we expect the oceanic reaction to feedback upon the atmosphere. We conclude:

1. The QBO influences the climate system response to the solar cycle in the atmosphere as well as in the ocean, especially in the SH.

2. This particularly strengthens the atmospheric "top-down" mechanism and brings the solar cycle response down to the surface.

3. In order to model a realistic climate response to varying natural forcings (e.g. solar cycle, QBO), numerical models need to include a realistically modeled middle atmosphere.

We have shown that a realistic middle atmosphere is essential for modeling studies, that investigate the solar cycle response of the Earth system. We further showed an atmospherically induced solar cycle response of the ocean, which may have the potential to feed back to the atmosphere. However, the answer to this question remains for further studies.

4.6 Concluding Remarks

In a retrospective view of this study it became clear that a thorough and responsible investigation of natural climate variations as intended within this work would substantially benefit from the application of a coupled climate model. Consequently, no effort was spared in order to

implement and evaluation the Community Earth System Model (CESM, cf. section 3.2.1) at the Deutsche Klimarechenzentrum (DKRZ) in Hamburg. After the successful implementation process of several million lines of CESM code, the program was tested by performing the computation of two decades of a reference experiment, which then was analyzed and compared to existing reference data from NCAR. Finally, the CESM implementation was found robust and four experiments were designed in order to investigate natural and anthropogenic climate variations. The outlines of these experiments are described in section 3.3. The analysis of these experiments focuses on global scale dynamical effects, e.g. mass and motion variations that alter the global Earth Rotational Excitation (cf. Chapter 5). The coupled climate model allowed to investigate these global scale effects for each subsystem separately. These analyses revealed dynamic coupling effects between the subsystems that are discussed in chapter 6.

Chapter 5

Atmosphere, Ocean and Land induced Earth Rotational Excitations

The Earth Rotational Excitations (EREs) represent an integral measure of the system state, condensing global mass and motion variations into 3 time series. Once the EREs are computed it is easy to compare model simulations among each other or perform a global model consistency check by comparing to observational data. This easily allows to identify globally varying features, which then can be investigated in more detail.

This chapter describes the variations of the modeled EREs for all CESM experiments (cf. section 3.3) and compares them to observational and operational ERE data. The observational data is provided by IERS (cf. section 2.3.1) with very high precession. The operational data is provided by the GFZ (cf. section 2.3.2) and offers EREs separated into mass and motion components for the atmosphere, ocean and land. The subsystems are modeled separately, where the atmosphere (provided by the ECMWF) assimilates observational data and is used to force the land and ocean model. The CESM EREs are also separated into mass and motion components for all subsystems, which are coupled physically consistent but do not consider any observational data.

The analysis starts comparing the annual cycle of the EREs ($\chi_{1,2,3}$), for observational (IERS), operational (GFZ) and modeled or synthetic (CESM) data. Comparing the annual cycle of the angular momentum of the subsystems (atmosphere, ocean and land) will naturally include only the operational and the synthetic data. Finally, this chapter discusses interannual ERE variations in the context of global scale climate phenomena, such as NAM and ENSO (cf. section 3.5). But first a general introduction on ERE including major scientific milestones is given.

5.1 Introduction

The Earth rotation is variable in terms of the rotation speed (length of day - LOD) and in the orientation of the rotational axis (polar motion - PM). It varies due to external and internal processes. External torques cause precession and nutation and are well known. They are for example related to lunar and solar tides. Reducing all external torques that act on the Earth system, leaves a well known total angular momentum budget. The Earth has highly dynamic fluidal components, such as the atmosphere and ocean, which feature mass and motion variations on daily to interannual scales. The total angular momentum of the atmosphere (AAM), ocean (OAM), continental hydrosphere (HAM) and the solid Earth is conserved, thus variations in one component triggers variations in any of the other ones.

Several studies indicated the importance of the AAM for subdecadal ERE variations. For example Barnes et al. (1983) found changes in length of day (ΔLOD) related to angular momentum transfer between the atmosphere and the solid earth. They also relate meteorological phenomena (here global wind and pressure patterns) to polar motion excitations. They find predominantly atmospheric mass terms exciting the polar motion rather than variations in the atmospheric motion. Regarding the length of day, Rosen et al. (1984) find the El Niño event of 1982/83 causing major wind anomalies, which translate directly into the motion term of the atmospheric angular momentum and in turn trigger changes in the LOD. They identify an El Niño related minimum of the equatorial atmospheric easterly momentum, while subtropical westerly momentum is exceptionally high. They speculate that the northern hemispheric subtropical jet strengthens and additionally moves further south altering the LOD. Later Chao (1989) finds a statistical relations between interannual LOD variations and El Niño as well as the QBO. However, the "correlation study" of Chao (1989) lacks any physical explanation. The polar motion components were more intensely discussed by Salstein and Rosen (1989), who identified the extratropical South Pacific, the North Pacific and the north Atlantic regions as especially important for polar motion excitation. They found that intraseasonal atmospheric surface pressure (mass component) variations strongly affect the polar motion.

Kuehne and Wilson (1991) identified terrestrial water storage influencing the total angular momentum budget from 1900 to 1985. They combine station wise observed atmospheric pressure, precipitation, evaporation, runoff and temperature values into 612 basins, representing the global terrestrial surface mass. Translating these values into EREs indicates that terrestrial water particularly influences the polar motion excitation on seasonal timescales. However, they do not indicate regions of particularly high influence.

Investigating the oceanic angular momentum (OAM) budget in the context of a modeling study, Ponte et al. (1998) showed significant polar motion excitation. They find the OAMs closing the total angular momentum budget towards observations on a seasonal to subseasonal

timescale. Again, they do not identify regions of especially high influence, but investigate the oceanic excitation on a global scale.

The combined effects on atmosphere and ocean excitation of the Earth's wobble were investigated by Gross et al. (2003). They found the atmosphere surface pressure explaining twice as much of the polar motion excitation as the atmospheric winds or the ocean bottom pressure on intraseasonal timescales. On these timescales they found the ocean currents even less important, explaining only a quarter of the variance of the atmosphere pressure. However, on interannual timescales they found that the ocean bottom pressure explains five times more than the whole atmosphere and twice as much as ocean currents.

Brzezinski et al. (2009) analyze several continental hydrosphere models with significantly different contributions to the global ERE budget. Combining them with a variety of AAMs and OAMs, they do not find a clear improvement towards observations. However, they find continental mass variations derived from GRACE data improving the ERE budget towards IERS observations. Brzezinski et al. (2009) identify mass inconsistencies among the continental model components and deficient models itself as reason for the absent improvement.

Dobslaw et al. (2010) use a mass consistent modeling set composed of atmosphere, ocean and land components. They analyze the combined effective angular momentum functions, identifying seasonal polar motion excitation that compensate each other. They also indicate that the remaining model errors prevent a further closing of the total angular momentum budget on a seasonal timescale. The data analyzed by Dobslaw et al. (2010) is identical to the operational data used in this study, which now is compared to fully coupled CESM EREs.

Finally, Dickey et al. (2010) indicate the importance of the ocean component (in addition to the atmosphere) from synoptic to interseasonal timescales. Likewise, Brzezinski et al. (2012) notes that the inclusion of the hydrosphere improves the overall ERE budget. They state that the "angular momentum exchange between solid earth and external fluids is capable to explain the whole Chandler wobble."

5.2 Annual Cycle of the EREs

The annual cycle accounts for the major part of the total variance and thus is important for a general evaluation of the synthetic (CESM) data with respect to operational (GFZ) and observed (IERS) data. The operational data is inverse barometrically (IB) corrected, meaning that the atmospheric surface pressure over the ocean is averaged for every time step separately (Wunsch and Stammer, 1997). For consistency reasons the same correction is applied for the synthetic data.

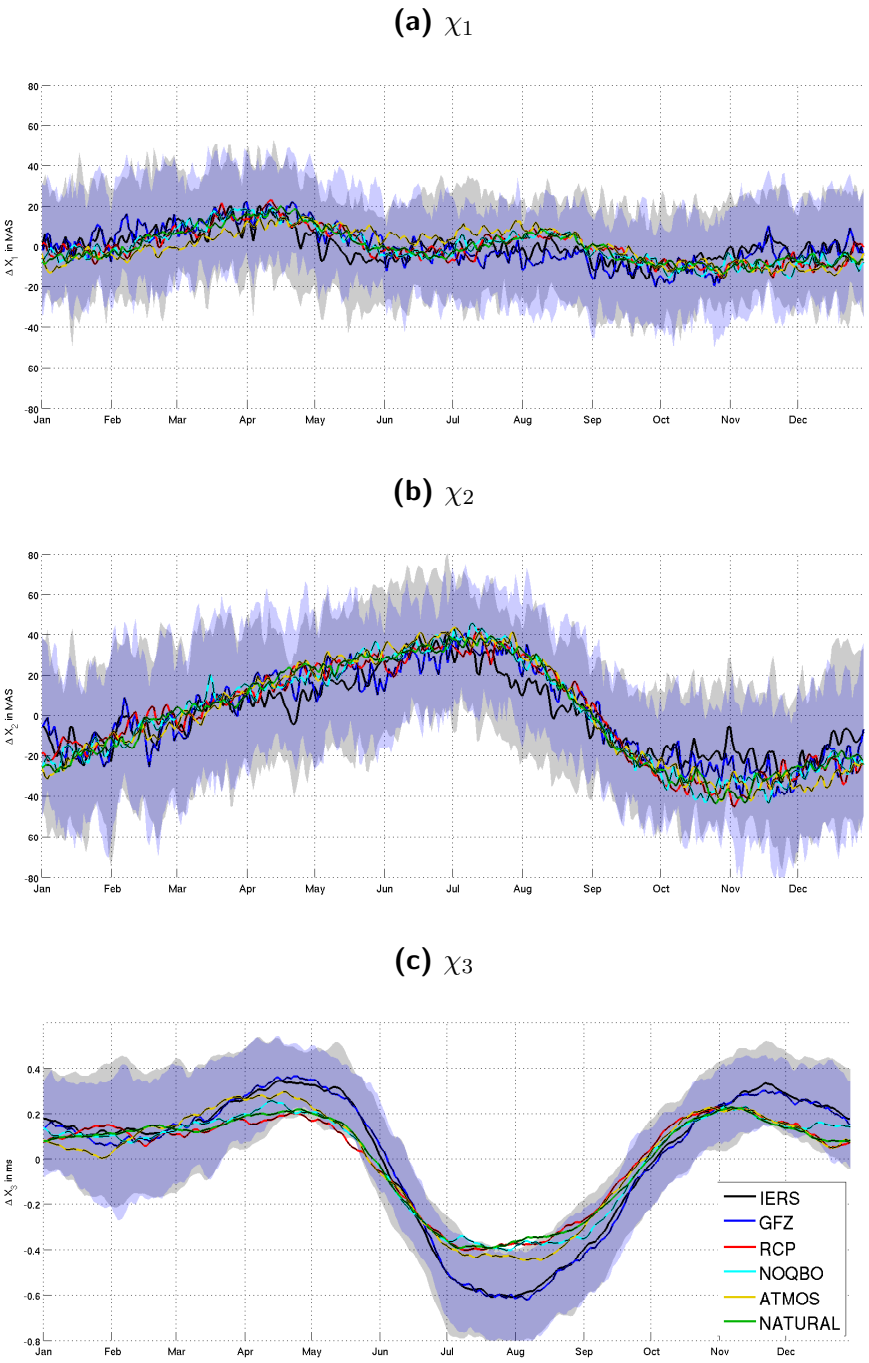

Figure 5.1: Annual cycle of daily observed IERS EREs (black), ERA40 based EREs (blue) and all CESM experiments, for a) χ_1, b) χ_2 and c) χ_3. The shaded region represents one standard deviation and is only given for the IERS and the ERA40 data.

5.2.1 Total Annual Cycle

Figure 5.1 shows the annual cycle of daily data for all three ERE components. The black line represents IERS observations, while the blue line shows the sum of operational atmospheric, oceanic and hydrologic EREs. The associated shaded regions show one standard deviation of

the respective annual cycle. Figure 5.1 shows good agreements between both data sets for all three ERE components, not only for the annual cycle, but also for the variability (shaded regions). The synthetic χ_1 data reveals a similar annual cycle for all CESM experiments. All data sets agree in a distinct peak in April, while the slight peak in August is solely present in the synthetic data. Further analysis will show, that these deviations are mainly caused by the atmospheric mass component and in more detail, the North Pacific atmospheric surface pressure. The lack of a clear annual cycle is clearly related to the IB correction, which states that the ocean compensates variations in the atmospheric pressure.

χ_2 shows an annual cycle for all data sets, peaking in June and July, with a minimum between October and November. CESM reproduces the observations, featuring a slightly broader maximum and minimum. However, the CESM angular momentum stays within one standard deviation of the observed and operational data. Further analysis will show that the χ_2 annual cycle is related to atmospheric pressure variations over the continents, which can not be compensated by the ocean.

Both components ($\chi_{1,2}$) show no significant variation among the different CESM experiments, leaving the introduced natural and anthropogenic variations with no major impact on the annular cycle of polar motion. The same is true for the interactive coupling of the ocean, which appears to have no significant influence on the annual cycle of $\chi_{1,2}$.

The third ERE (χ_3) shows the most distinct annual cycle peaking in April and November, with an absolute minimum in July and August and a minor minimum in January and February. CESM captures the main features, but reveals weaker amplitudes. The synthetic data shows a 0.2 ms weaker absolute minimum, while the secondary minimum compares in amplitude to the observations. Both peaks are weaker as well, the first one is in phase with observations, and the second one about a month earlier. Rosen and Salstein (1983) and Anderson and Rosen (1983) already indicate that the annual cycle of χ_3 is mainly related to asymmetric subtropical jet strength between the southern and the northern hemispheres. The southern hemispheric subtropical jet is stronger and more persistent than the northern one. The less pronounced synthetic annual cycle indicates a weaker modeled asymmetry between the northern and southern hemispheric jets. Besides the differences in amplitude there is an offset in the peak in boreal fall. This indicates that the modeled northern hemispheric jet builds up too fast and reaches its maximum about one month too early.

The most significant deviation among the CESM experiments is modeled by ATMOS, where the χ_3 component is in better agreement with the observation in March and April, but also in August. On the other hand it disagrees more in January and the beginning of February. Further investigations will show, that this is mainly related to the absence of the annual cycle of the ocean mass component IO_3, which is negative in March and April and positive in August (I_3 amplitude 0.05 ms, cf. Figure 5.6 c and d).

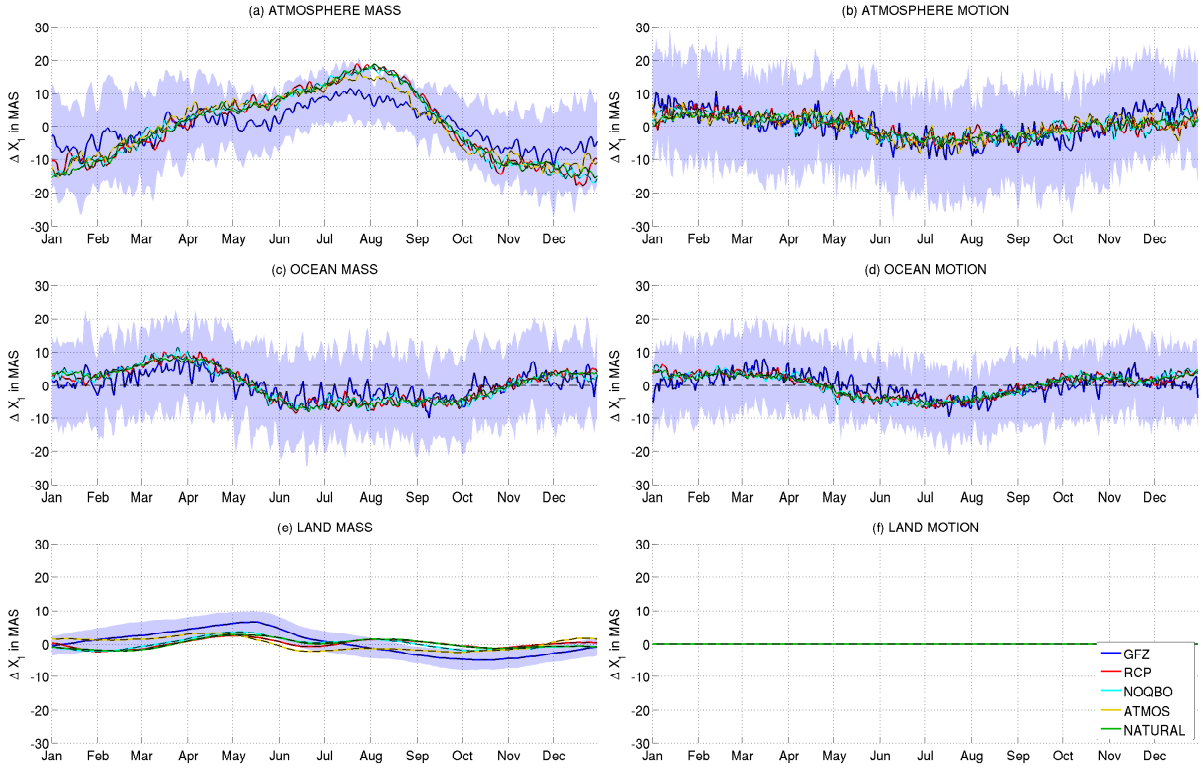

Figure 5.2: Contribution to the annual cycle of χ_1 as shown in Figure 5.1, separated into mass (left column) and motion (right column) for atmosphere (top line), ocean (middle line) and land (bottom line). The blue line represents the reference system consisting of ERAI data (atmosphere), OMCT (ocean) and LSDM (land), both forced with the ERAI data. The shaded region represents one standard deviation of the annual cycle.

5.2.2 Annual Cycle of the Subcomponents

This section discusses the influence of the mass and motion terms of the atmosphere, ocean and land components on the total EREs. This will indicate the sources of deviations of the total modeled signal to the total observational and operational data (cf. Figure 5.1), allowing to evaluate the overall performance of the respective subsystems. The IERS observations provide only information on the total EREs and thus cannot be considered in the upcoming comparison.

Figure 5.2 shows the separation of χ_1 into components of the atmosphere (top), ocean (middle) and land (bottom) for the mass (left column) and motion (right column) terms. The blue line represents again the annual cycle of the operational EREs, including one standard deviation marked by the shaded region. Plotted on top are the annual cycles for all CESM experiments.

Clearly, the atmospheric mass component (Figure 5.2a) shows the largest disagreement between the operational and the synthetic data. Comparing this to the total χ_1 signal (Figure 5.1a) reveals that the misfit to the observations during July and August is mainly introduced by

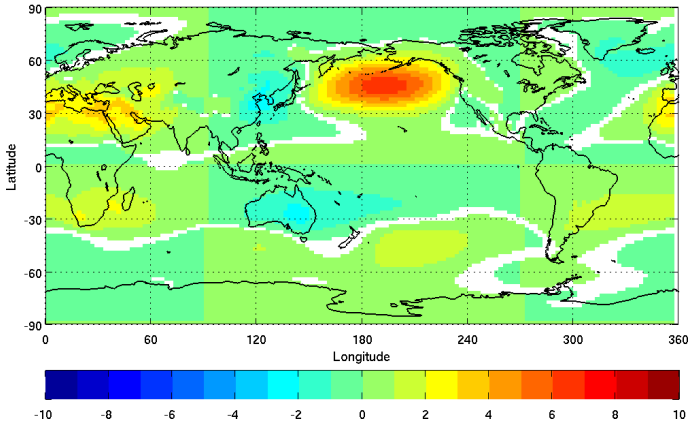

Figure 5.3: Normalized $IA_1(\phi, \lambda, t)$ CMDs for $IA_1^{max}(t)$ minus $IA_1^{min}(t)$ conditions. The chessboard pattern results from IA_1 weighting function (cf. Figure 2.1. Statistical significance of the colored values is 99%.

the atmospheric mass variation. Only the ATMOS experiment shows a distinguished pattern among all CESM experiments. Keeping in mind that the first mass component (I_1, cf. Figure 2.1) is heavily weighted over the ocean, which is IB corrected, opens the question of total uncorrected atmospheric signal. The uncompensated (non-IB corrected) atmospheric signal reveals about twice the amplitude of the annual cycle. Figure 5.3 shows the $IA_1(\phi, \lambda, t)$ map (cf. section 2.1.3) for $IA_1^{max}(t)$ minus $IA_1^{min}(t)$ conditions for the non-IB corrected atmospheric mass component, normalized by the field standard deviation. Thus it shows the normalized $IA_1(\phi, \lambda, t)$ CMDs allowing to identify the regions which are most influential for $IA_1(t)$. Figure 5.3 clearly shows that the North Pacific region is dominating the $IA_1(t)$ time series. As described in section 7.1 the atmospheric mass component $IA_i(t)$ is computed solely based on the surface pressure and the ERP weighting functions (cf. Figure 2.1).

The modeled atmospheric motion components (hA_1, Figure 5.1b) feature only a weak annual cycle, which is in good agreement with the operational data, showing only slight and insignificant deviations from the end of November to the beginning of January. Due to the χ_1 wind pattern (cf. Figure 2.1) it is hard to associate this deviation to a certain region.

The annual cycle of both ocean components (IO_1,hO_1) agrees with the operational data, showing only minor deviations. Further, there is virtually no difference between the different CESM experiments, suggesting no anthropogenic nor QBO effects on the integrated ocean component of χ_1. It is interesting to note, that the operational ocean signal (OMCT) features more variations on a daily to submonthly scale. One would expect that these features average out over the decades, which is not the case. Especially the time between June and September features a regular pattern which reminds of tides. However, all tidal forcings are turned off for the OMCT experiment leaving only the possibility of atmospheric induced tides on the ocean signal. Based on personal communication with Henryk Dobslaw this is unlikely, especially since the amplitude of this signal is well within the range of one sigma, or in other words it is

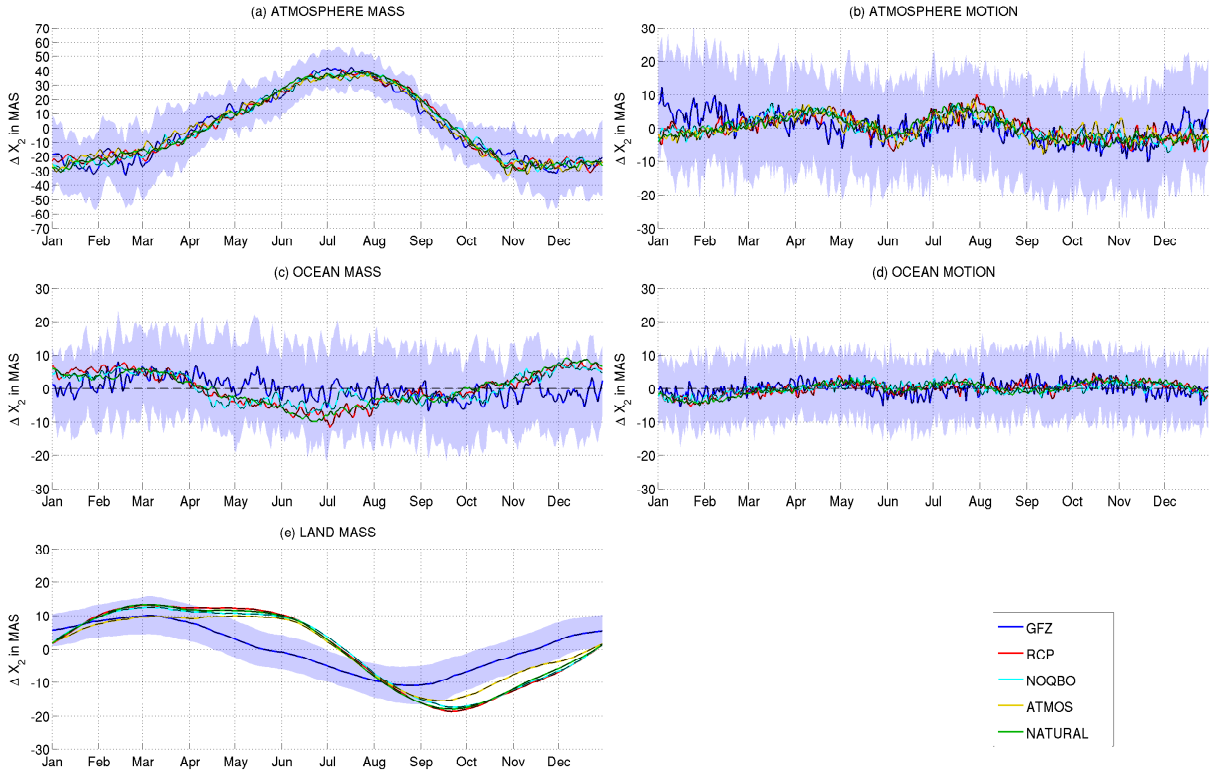

Figure 5.4: Same as Figure 5.2, but for χ_2.

insignificant. Performing a FFT analysis of the respective time series, reveals no particularly high power on a submonthly timescale.

The annual cycle of the ERE land component (IL_1, Figure 5.2e) shows clear deviations between operational and synthetic data. This is likely related to variations in the precipitation minus evaporation (PmE) over land and the capability of the soil to contain and discharge water. Despite the recent improvements of the precipitation and evaporation modeling in the context of coupled climate models, there is still room for further progress especially regarding the precipitation patterns (Gent et al., 2011; Meehl et al., 2011b; Deser et al., 2011). Since the operational IL_i time series are based on precipitation and evaporation from ERA-Interim data, they are more reliable than the modeled components. Consequently the differences between the synthetic and operational IL_1 is not suitable for evaluating the land component, but can rather be understood as an additional measure of the atmospheric component, namely the capability of a realistic precipitation modeling over the continents. The land motion component is smaller by the order of at least three (Dobslaw et al., 2010), and thus can be neglected.

Summarizing, the most significant part of the modeled χ_1 component is related to atmospheric mass variations, which is clearly dominated by the surface pressure in the North Pacific region, which in turn is compensated by the IB correction, leaving hardly any annual cycle. Figure 3.3 shows that the modeled surface pressure variations in the North Pacific exaggerate

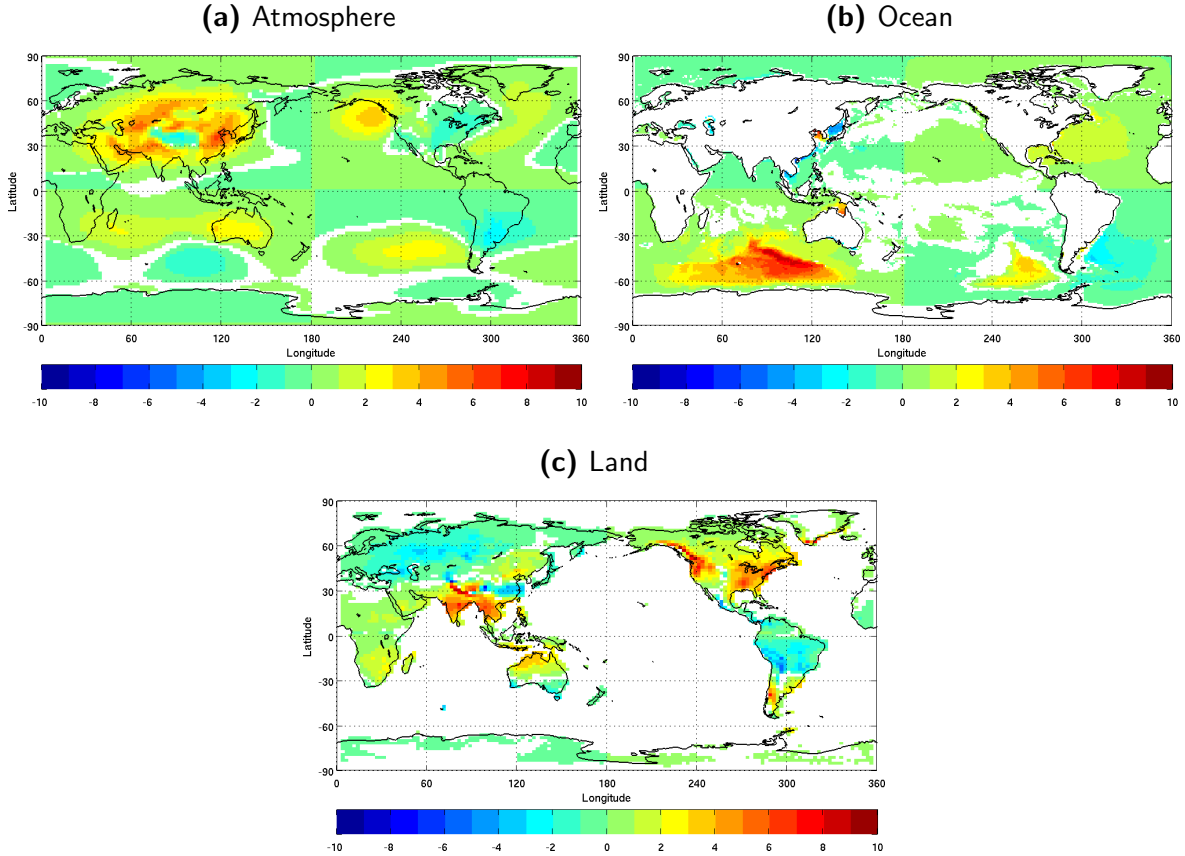

Figure 5.5: Same as 5.3, but now for IA_2,IO_2 and IL_2.

the ERA-Interim the MERRA data, while the variations in the north Atlantic are modeled too weak. This sectorial imbalance translates directly into the modeled χ_1 signal for the non-IB corrected atmosphere. However, it is compensated by the ocean, leaving hardly any annual cycle at all.

Analyzing the separated χ_2 signal (Figure 5.4), which is more heavily weighted over the continents, reveals a good agreement between the atmosphere mass components of the synthetic and the operational data. The amplitude as well as the phase are in good agreement for the IB corrected atmospheric mass signal. Analyzing the ERE maps (Figure 5.5) shows that the main χ_2 related atmosphere mass variations (IA_2) are located over the whole Asian continent except the Himalaya. There are other significant atmospheric mass features on a global scale, however, they cancel out, leaving the surface pressure over Asia explaining most of the variance. The total standard deviation of the surface pressure is modeled rather good over the continents (cf. Figure 3.3), however that does not mean that the surface pressure is modeled correctly on a global scale. For example, it is possible that the Asian pressure variations are modeled slightly too strong, while the pressure variations over North America are modeled slightly too weak, canceling out on a global scale. Investigating the non-IB corrected

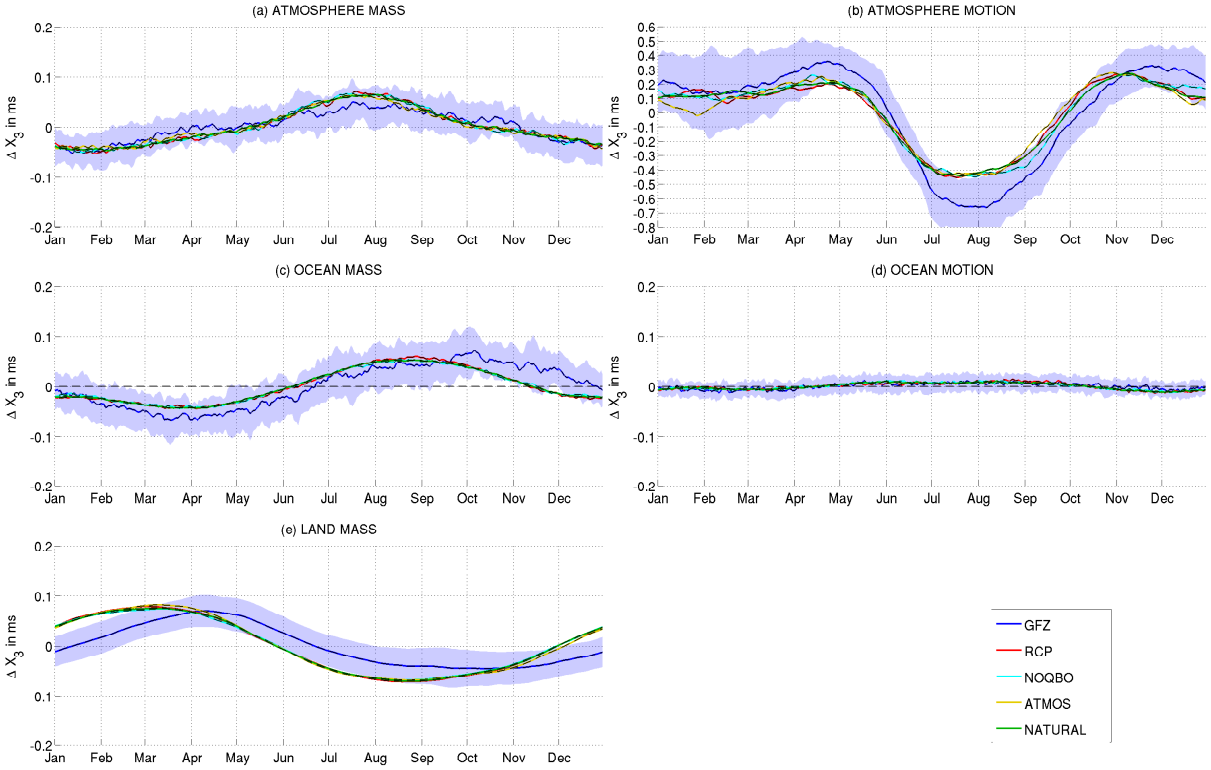

Figure 5.6: Same as Figure 5.2, but for χ_3.

atmospheric mass signal reveals a shift of the annual cycle peak, whcih mus be related to pressure variations over the ocean.

The CESM ocean mass components (IO_2, Figure 5.4c) show a clear annual cycle, which is not present in the operational data. These variations are dominated by the southern Indian ocean (cf. Figure 5.5b). The oceanic motion component shows no significant annual cycle neither for the operational nor for the CESM data and it is also not possible to identify special regions influencing the second oceanic motion component (hO_2).

The mass variations on land (IL_2, Figure 5.4e) show a strong annual cycle for both, the synthetic and the operational data. However, the operational data shows again a smooth sinusoidal pattern, while the CESM data shows a stronger and more diverse annual cycle. CESM computes significant χ_2 related hydrological mass variations on all continents besides Antarctica (Figure 5.5c). Experiment ATMOS features a slightly different annual cycle than the other experiments, which is clearly related to hydrological mass variations in southeast Asian and India. Meehl et al. (2011a) find a realistic connection between ENSO and the Asian-Australian monsoon modeled by CESM. Consequently is the absence of ENSO altering the monsoon, which translates into variations of IL_2. Further these results allow the conclusion that ENSO strengthens the monsoon related precipitation of southeast Asia and India, leading to a more pronounced IL_2 cycle for the fully coupled modeling settings.

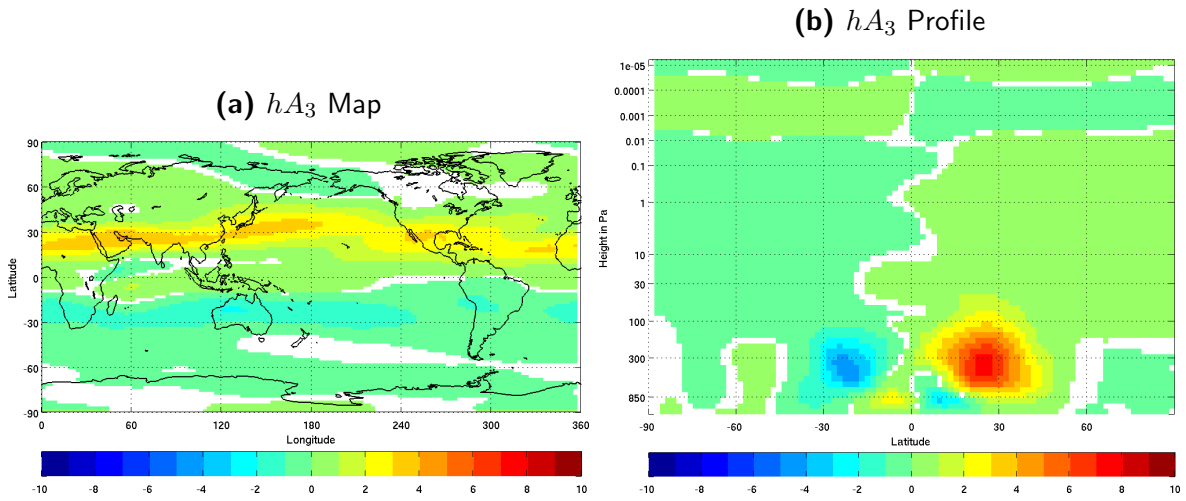

Figure 5.7: Same as 5.3, but now for hA_3: (a) vertically integrated showing the influential regions on a map; and (b) zonally integrated, showing the influential regions in the atmospheric profile.

Walter (2008) compares the excitation of the polar motion for several continental hydrosphere models (including the predecessor of the here used LSDM version) which are forced with different reanalysis data sets. The author finds strong variations of the annual cycle among the models and even for the same model forced with different reanalysis data sets. In general, the LSDM showed more variability than the other models. Walter (2008) relate the amplitude of the IL_i signal to the precipitation over land, however they find the phase shift of the annual cycle related to models capability of discharging water. Thus Figure 5.4e shows comparable global precipitation amplitudes, but CESM models the water discharge of the continents slower than the LSDM.

Figure 5.6 shows the separated χ_3 signal. Clearly the atmosphere motion (hA_3) accounts for most of the annual variance. Here, CESM underestimates the amplitude, indicating that the asymmetry between the northern and southern hemispheric jet is modeled too weak (Rosen and Salstein, 1983; Anderson and Rosen, 1983). The contributing regions for the hA_3 signal are presented in Figure 5.7a, which shows the influential regions of a vertically integrated atmosphere. For a better understanding, Figure 5.7b shows the influential regions of the zonally averaged atmosphere or in other words, the average vertical structure of the hA_3 contributions. Figure 5.7 shows that the northern hemispheric jet accounts for the major part of the annual cycle, while the southern hemisphere shows not such a strong annual cycle. Therefore one can assume that especially the annual cycle of the southern hemispheric jet is modeled too weak. Whether this means that the southern jet is too weak during austral winter or too strong during austral summer can not be assessed. Solely the fact that the variations between both states is too weak can be deduced.

The annual cycle of the atmospheric mass component (Figure 5.6a) is slightly overestimate by all CESM experiments. Analyzing the important regions (Figure 5.8a) shows positive values

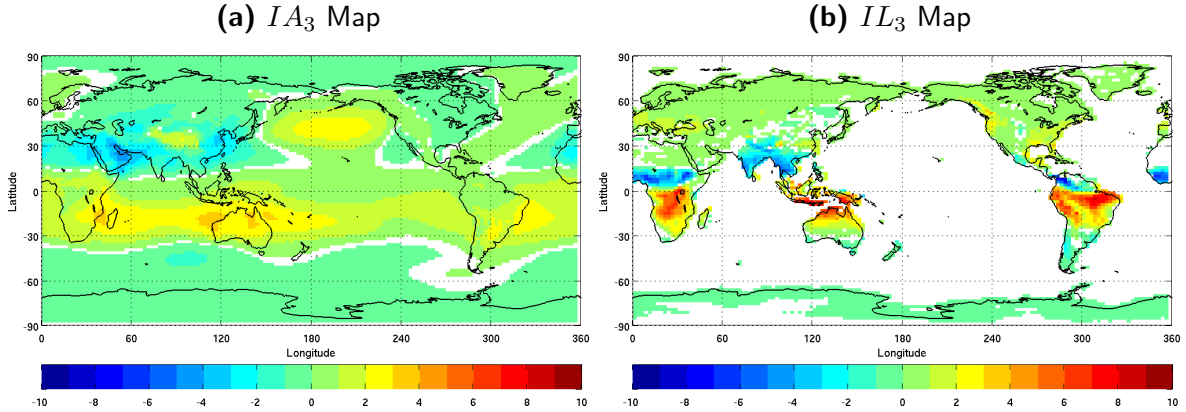

Figure 5.8: Same as 5.3, but now for IA_3 and IL_3.

in the southern tropics and subtropics including especially strong values over north Australia as well as southeast Africa. Northern Africa, as well as the Arabian peninsula and parts of southeast Asia show negative values. Again the North Pacific region appears important featuring a large scale positive influence, which is compensated by the IB correction. However, since IA_3 is influenced by surface pressure variations all over the world, this connection is not as clear as for example for IA_1 (cf. Figure 5.3).

The ocean components show a significant annual cycle only for the mass variations. Here the synthetic and the operational data show good agreements, with slight deviations from October to December. These features cannot be attributed to a certain region, but are rather the result of ocean mass variations on a global scale, with slightly more influence of the subtropical oceans.

The annual cycle of the continental hydrosphere (Figure 5.6e) shows again similar amplitudes for the synthetic and the operational data indicating similar amounts of total precipitation. However, there is a clear phase shift indicating again deviations in the modeled continental water discharge. It also indicates an actual offset in the time when the raining season starts. Figure 5.8b shows that all tropical and subtropical land areas influence IL_3.

5.3 Interannual ERE variations

After analyzing the observed, operational and synthetic annual cycle of the EREs, this section now investigates the interannual variability. The visualized data are monthly mean values, which are detrended and high pass filtered with a half power point at seven years. The annual cycle (as shown in Figure 5.1) is removed. In order to quantify the total ERE related mass and motion variability for each subsystem, the standard deviation for the whole IB corrected time series is plotted in Figure 5.9. The color code is in agreement with previous figures, visualizing results for the operational (GFZ) EREs and for all synthetic (CESM) EREs.

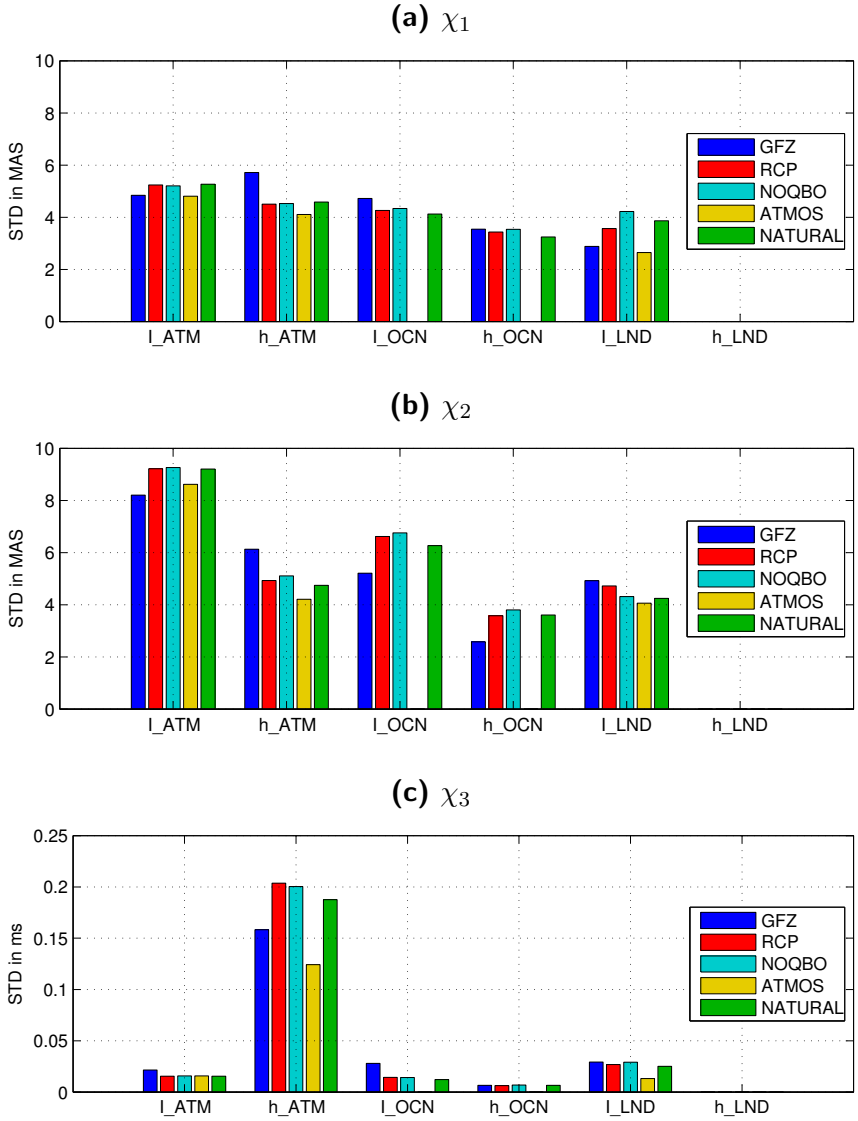

Figure 5.9: Standard deviation of the deseasonalized interannual angular momentum functions for ERA-Interim data and all four CESM experiments.

5.3.1 Interannual χ_1 excitations

Figure 5.9a shows the interannual standard deviation of all χ_1 subcomponents. The modeled interannual variations agree with the operational data for the IB corrected mass terms. For the non-IB corrected atmospheric mass we find the interannual standard deviations of the χ_1 component increased by the factor of 3-4, which is in line with the overestimation of non-IB corrected annual cycle and can again clearly be attributed to a sectorial imbalance of the surface pressure between the north Atlantic and the North Pacific ocean. Figure 5.14a clearly shows that the modeled interannual IA_3 variations are highly related to the North Pacific surface pressure, which is filtered by the IB correction and thus not present in Figure 5.9a. The atmospheric motion component is slightly underestimated by CESM and shows almost no

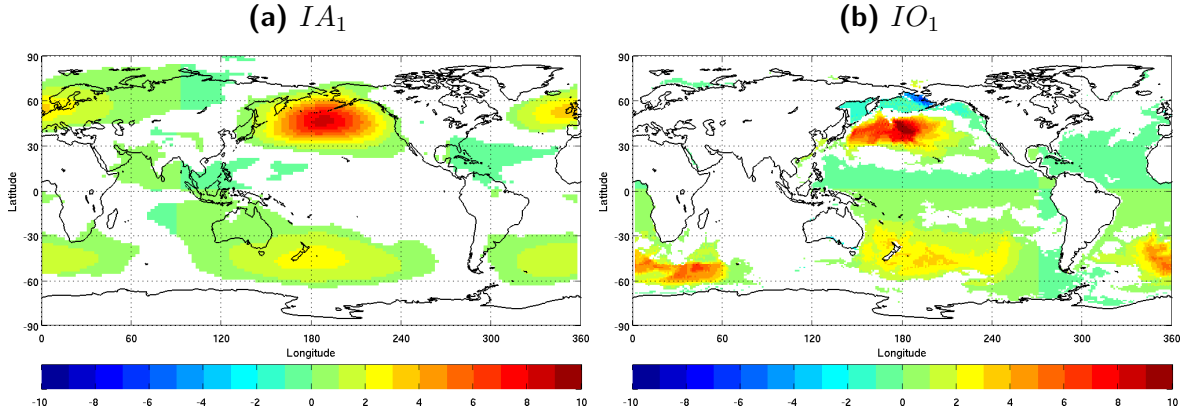

Figure 5.10: Same as 5.3, but now for deseasonalized IA_1 and IO_1.

interexperimental variations in hA_1. However, there are significant differences in the modeled interannual wind fields, which cancel out due to the ERE weighting functions (cf. Figure 2.1) for hA_1 and hA_2. Nevertheless, they are clearly visible and discussed for hA_3.

There is a good agreement between the operational and the modeled ocean variations, showing only little differences among all CESM experiments. The major part of the ocean mass signal (IO_1) is related to variations in the North Pacific (cf. Figure 5.10b). In the upcoming chapter 6 this oceanic mass variation is investigated in more detail, including a thorough comparison to GRACE observations. Mass variations in the south Atlantic and south Pacific ocean show minor influences on IO_1.

The total interannual variability of the continental hydrology (IH_1) features deviations throughout all CESM experiments. There is a slight increase of the variability for the NOQBO experiment and a clear reduction in the ATMOS data. The reason for this can not be attributed to certain regions. The IL_3 maps (not shown) indicate interannual hydrology variations in Australia, which is slightly weaker in experiment ATMOS. This is likely related to ENSO, which is known to influence interannual precipitation variations in that region. However, then one would also expect mass variations in South America, which cannot be identified in any CESM experiment. The absence of the QBO nudging slightly increases continental hydrosphere variations especially in subtropical north Africa. This possibly indicates a connection between the QBO and the Intertropical Convergence Zone (ITCZ) over Africa. To the knowledge of the author there is currently no study available discussing this topic for reference.

Summarizing, the interannual variability of the χ_1 subcomponents shows that the operational data suggests similar contributions from the atmosphere, ocean and land, which agrees with the CESM simulations.

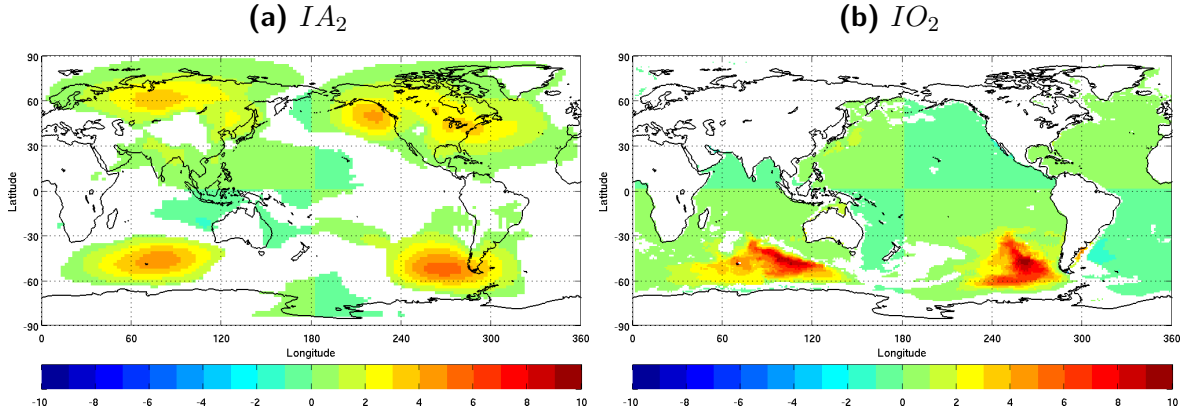

Figure 5.11: Same as 5.3, but now for deseasonalized IA_2 and IO_2.

5.3.2 Interannual χ_2 excitations

The interannual variations of the second component χ_2 show a more diverse picture among the operational and synthetic data. CESM slightly exaggerates variations in the atmosphere mass component (IA_2), which is predominantly related to a surface pressure quadrupole (Figure 5.11), similar to the mass weighting function (cf. Figure 2.1a). Interesting here is the fact, that the southern Indian ocean is modeled in phase with the North American pressure signal and that the Asian signal is in phase with the south east Pacific pressure system. Moreover, these two pairs are complementary to each other, meaning that positive IA_2 variations feature positive pressure anomalies in North America and the southern Indian ocean and additionally negative pressure anomalies in Asia and the south east Pacific region. The atmosphere motion component (hA_2) is again related to the subtropical jets and hard to interpret due to the weighting functions. However there are variations among the CESM experiments which are discussed in the context of hA_3.

Variations in the ocean mass components (IO_2) are clearly attributed to mass anomalies in the southern Indian and southeast Pacific ocean (Figure 5.11b), which are directly related to the prevailing winds and the wind stress curl (Boening et al., 2011; Bergmann and Dobslaw, 2012). CESM appears to model stronger interannual ocean mass variations in this region, which could be related to variations in the wind forcing or a different model behavior. Variations in the ocean motion component (hO_2) cannot be attributed to a specific current. However, the southern hemisphere appears to play a more vital role indicating relations to the ACC.

The modeled continental hydrology shows slightly smaller interannual variations compared to the operational data. The strongest contributions to IH_2 can be related to southeast Asia and the eastern part of North America (not shown). All in all, Figure 5.9 a and b show that CESM captures most of the global interannual polar motion variations for all subcomponents.

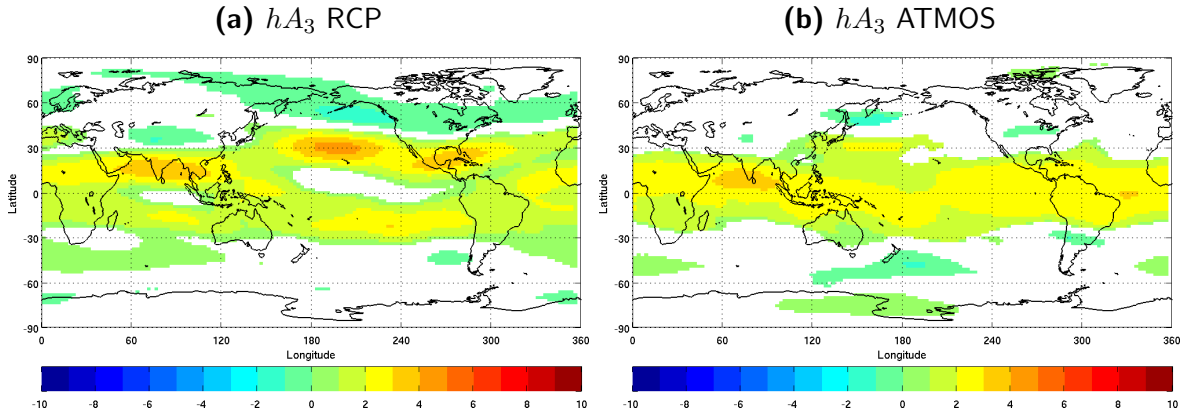

Figure 5.12: Same as 5.3, but now for deseasonalized hA_3 for experiments RCP and ATMOS.

5.3.3 Interannual χ_3 excitations

The interannual variations of the third ERE component is dominated by atmospheric motion (hA_3, cf. Figure 5.9c). This is true for the synthetic and the operational data and agrees with the contributions to the annual cycle. However, in contrast to the underestimated synthetic annual cycle, CESM models stronger interannual variations for all, but the ATMOS experiment. Comparing the ERE maps throughout the CESM experiments (Figure 5.12) shows surprising differences. The first three experiments (NATURAL, RCP, NOQBO) show similar patterns: interannual hA_3 variations are dominated by the subtropical jets on a global scale. Exemplarily for all three experiments Figure 5.12a shows the influential regions only for experiment RCP. Experiment ATMOS (Figure 5.12b) shows a completely different pattern, especially over the Pacific and the Atlantic sector. There are no distinguished interannual subtropical jet variations.

Figure 5.13 provides further insight by showing the profile of the zonal mean ERE contributions to hA_3. These figures represent the zonal mean zonal wind weighted with respect to the mass and again normalized by the field standard deviation. Experiments NATURAL (not shown) and RCP (Figure 5.13a) agree over the whole atmospheric profile. For both scenarios the interannual hA_3 variation can be attributed to the subtropical jets and the QBO. For both experiments the northern hemisphere shows stronger variations. Figure 5.13b shows the influential profile for experiment NOQBO. Clearly and as expected the interannual variations in the equatorial stratosphere vanishes in the region of the QBO nudging, leaving all interannual variations related to the subtropical jets. Experiment ATMOS (Figure 5.13c) shows the influence of the QBO again, but features virtually no interannual variations of the jets. Nevertheless, there is a clear jet (cf. Figure 5.7), but it shows no interannual variation when a climatological ocean is used as forcing. This means that interannual ocean processes (such as ENSO) are likely to influence or even trigger interannual jet variations. It is known that ENSO alters the position of the jets, especially in the Pacific (Chen et al., 1996; Carleton, 2003). For

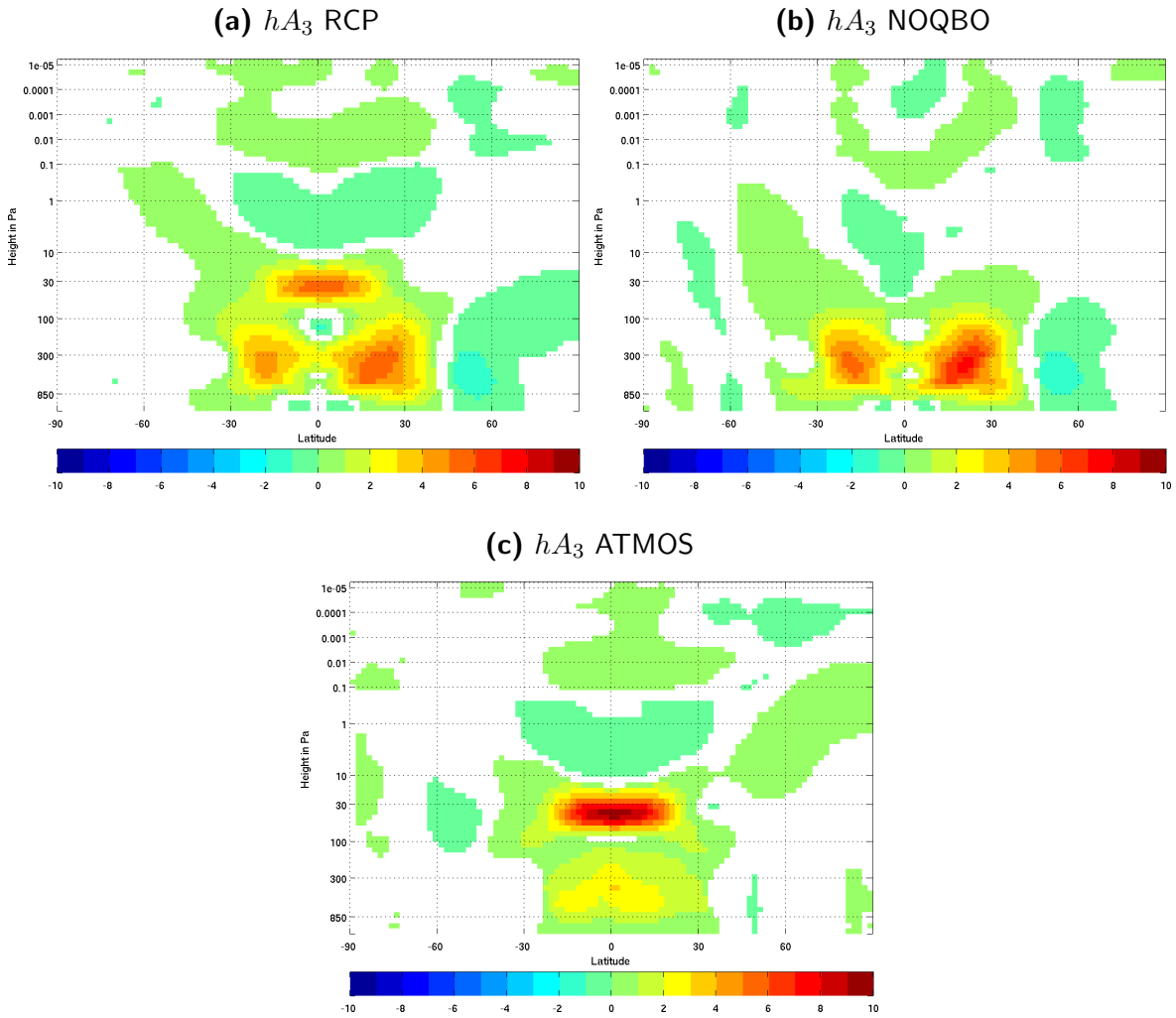

Figure 5.13: Same as 5.12, but now for the profile of hA_3.

example during the El Niño phase the northern jet moves equator ward in the Pacific. Consequently experiment ATMOS should feature a different interannual jet variation compared to the other experiments. However, the fact that the interannual jet variation disappears using a climatological ocean as boundary condition, is new.

Further, the operational data shows similar variations for all mass components (IA_3, IO_3, IH_3), which is not met by the CESM results. Atmospheric and continental hydrosphere variations are of about the same magnitude, but the ocean mass variations are significantly lower in the synthetic data. The atmospheric mass variations compare well for all CESM experiments. This means, that globally integrated lateral mass variations (e.g., from the pole towards the equator) are not affected by the ocean coupling on a global scale. However, if we subdivide into oceanic sectors we clearly see an effect of the ocean coupling which propagates into the polar motion signal. There is no ENSO effect in the χ_3 related atmosphere mass component, because ENSO is characterized by pressure anomalies along the equator (cf. Figure 3.8), which average out for the global integration (cf. Figure 2.1). Nevertheless, it

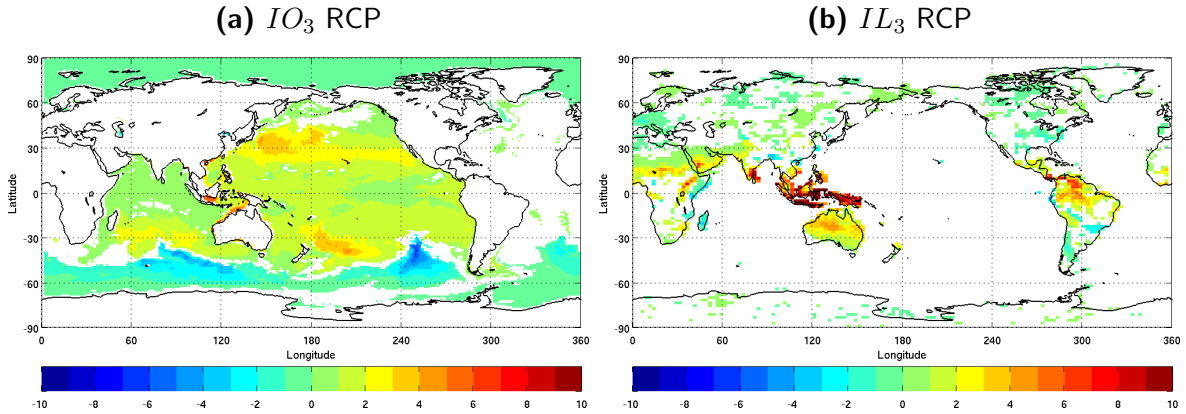

Figure 5.14: Same as 5.3, but now for deseasonalized IO_3 and IL_3.

does affect precipitation and evaporation over the continents leaving experiment ATMOS with significantly smaller interannual variations of the land mass component. The synthetic ocean mass variations are significantly below the operational ones. The reason for this can not be located in a specific region, but represent a global feature. Figure 5.14a shows the influencing regions for IO_3 highlighting no specific region as dominant. Ocean motion hardly affects the angular momentum budget for any data set, meaning that variations in the eastward and westward ocean currents average out on a global scale.

Summarizing, this section compares the interannual angular momentum budget between operational and synthetic data. In general, the ocean and land components agree well. Regarding the atmosphere we find strong and significant sectorial differences related to the surface pressure (cf. Figure 5.10a). We find CESM overestimating the northern Pacific region, while the north Atlantic features significantly smaller variations. This sectorial imbalance is filtered by the IB correction, leaving the total χ_1 signal on a realistic level. The second CESM component χ_2 is dominated by the atmospheric mass, which is now influenced by both hemispheres (cf. Figure 5.11a). The synthetic total lateral mass variation (from the poles towards the equator - χ_3) agrees well with the operational data. The most significant variation among all CESM experiments is the absence of interannual subtropical jet variability for the ATMOS experiment, which substantially reduces the total variance of hA_3 (cf. Figure 5.13).

The upcoming section will discuss interannual ERE variations upon global scale climate phenomena namely NAM and ENSO. These climate modes are widely discussed throughout the literature, including their effect on modeled and observed EREs. Thus the quality of the herein investigated CESM experiments regarding the capability of modeling NAM and ENSO can be evaluated with respect to other studies. The preceding discussion of annual and interannual variations of the EREs and especially the comparison of the synthetic with the operational data will help to evaluate the NAM and ENSO results.

(a) NATURAL NAM: 1955 - 2099 **(b)** NATURAL ENSO: 1955 - 2099

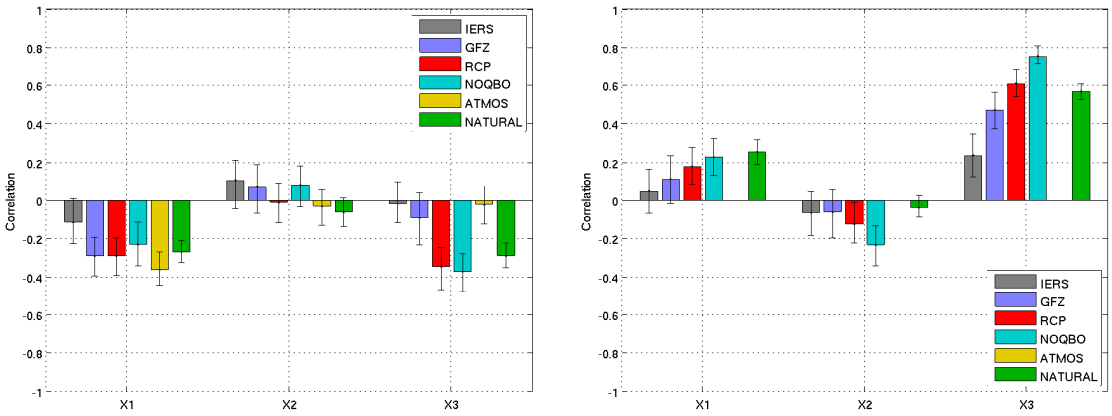

Figure 5.15: Correlation between the EREs ($\chi_{1,2,3}$) and a) the NAM and b) the ENSO index, for monthly mean deseasonalized values. The NAM and ENSO indices used for IERS and operational data are the same[1]. The indices for the CESM experiments are computed individually. The error bars denote 99% significance.

5.4 NAM and ENSO related interannual ERE variation

NAM and ENSO as global scale climate phenomena, are good candidates for a possible influence of the global angular momentum, since both explain a significant amount of interannual climate variability, including mass and motion variations in atmosphere, ocean and on land. While ENSO influences mainly the tropical and subtropical region, we find the NAM confined to the northern hemisphere. This study does not include an investigation of the Southern Annular Mode (SAM), which explains the major part of the interannual southern hemispheric climate variability. Nevertheless, this remains an interesting subject for further studies.

In this section we again use monthly mean values, which are processed as described in chapter 2. Observed NAM and ENSO indices are provided by NOAA[1]. The CESM indices are computed in accordance to the section 3.5.

In order to find a relation between NAM and ENSO time series and the global angular momentum, we compute the correlation between $\chi_{1,2,3}$ and the NAM and ENSO indices for observed (IERS, NOAA), operational (GFZ) and synthetic (CESM) data. The results are presented in Figure 5.15. The color coding is again in agreement with previous figures. The error bars denote the 99% significance level. Note, that the error bar for the NATURAL experiment tends to be smaller than for the other data sets, because it includes the longest time series (145 years).

Figure 5.15 needs to be investigated in the context of Figures 5.16 and 5.18, which show besides the total correlation of NAM and ENSO with $\chi_{1,2,3}$ also the correlations for the

[1] `http://www.esrl.noaa.gov/psd/data/climateindices/list/`

subcomponents. For example, Figure 5.16a shows the total correlation of the NAM index with the operational angular momentum variation χ_i in cyan (the widest bars). These values and error bars are identical with the ones for the operational data in Figure 5.15 (blue bars). The additional information of Figures 5.16 and 5.18 remains in the yellow and blue bars, which allow a direct evaluation of the influence of the subcomponents. The yellow bars represent the correlation between the climate index and the total angular momentum of the subsystems atmosphere (A_i), ocean (O_i) and land (L_i) for the respective ERE component ($\chi_{1,2,3}$). The slim blue bars show the correlation between the climate index and the angular momentum of the mass (I) and the motion (h) components for all subsystems. Summarizing, Figure 5.16 provides an overview of the integrated effects that the NAM implies on the climate system. This includes the total effect (χ_i) as well as a separation into atmosphere, ocean and land and even allows to differentiate between mass and motion effects. Finally the ERE maps (Figures 5.17 and 5.19) provide information about the regions, where NAM and ENSO related mass and motion variations influence the EREs.

5.4.1 NAM

Investigating the ERE correlation with the NAM index (Figure 5.15a) shows a generally good agreement between the IERS observations and GFZ operational data. The observations show small negative and barely significant correlations for χ_1, while the operational data features higher correlation values. Both data sets do not show any significant correlation for the other two components $\chi_{2,3}$. The CESM correlations agrees for χ_1, where we find significant negative correlations around -0.3, which is in good agreement with the operational data. The synthetic χ_2 correlations agree in with the observations as well as the operational data in featuring no significant correlation. Regarding χ_3 we find CESM exaggerating observational and operational data for all experiments but ATMOS.

Figure 5.16 reveals two reasons for the exaggeration of the modeled χ_1 correlation. All CESM experiments feature a slight negative correlation between the atmospheric mass signal (IA_1) and the NAM index, which is not present in the operational data. Additionally, is exaggerated by all CESM experiments altering the total χ_1 component. The net ocean effect is modeled positive, while the operational data suggests a negative influence.

Reviewing Figure 3.4 reveals, why the synthetic data shows no correlation for the atmosphere mass component: the positive pressure anomalies are well balanced between the Pacific and the Atlantic sector and thus the signal averages out according to the weighting functions of the mass 1 signal (cf. Figure 2.1). Besides, does the IB correction filters all presser signal over the ocean. All CESM experiments feature more pressure variations in the Pacific, which on the one hand influences directly the synthetic NAM index and on the other hand directly influences the non-IB corrected χ_1 atmospheric mass signal. Consequently, we find a high correlation

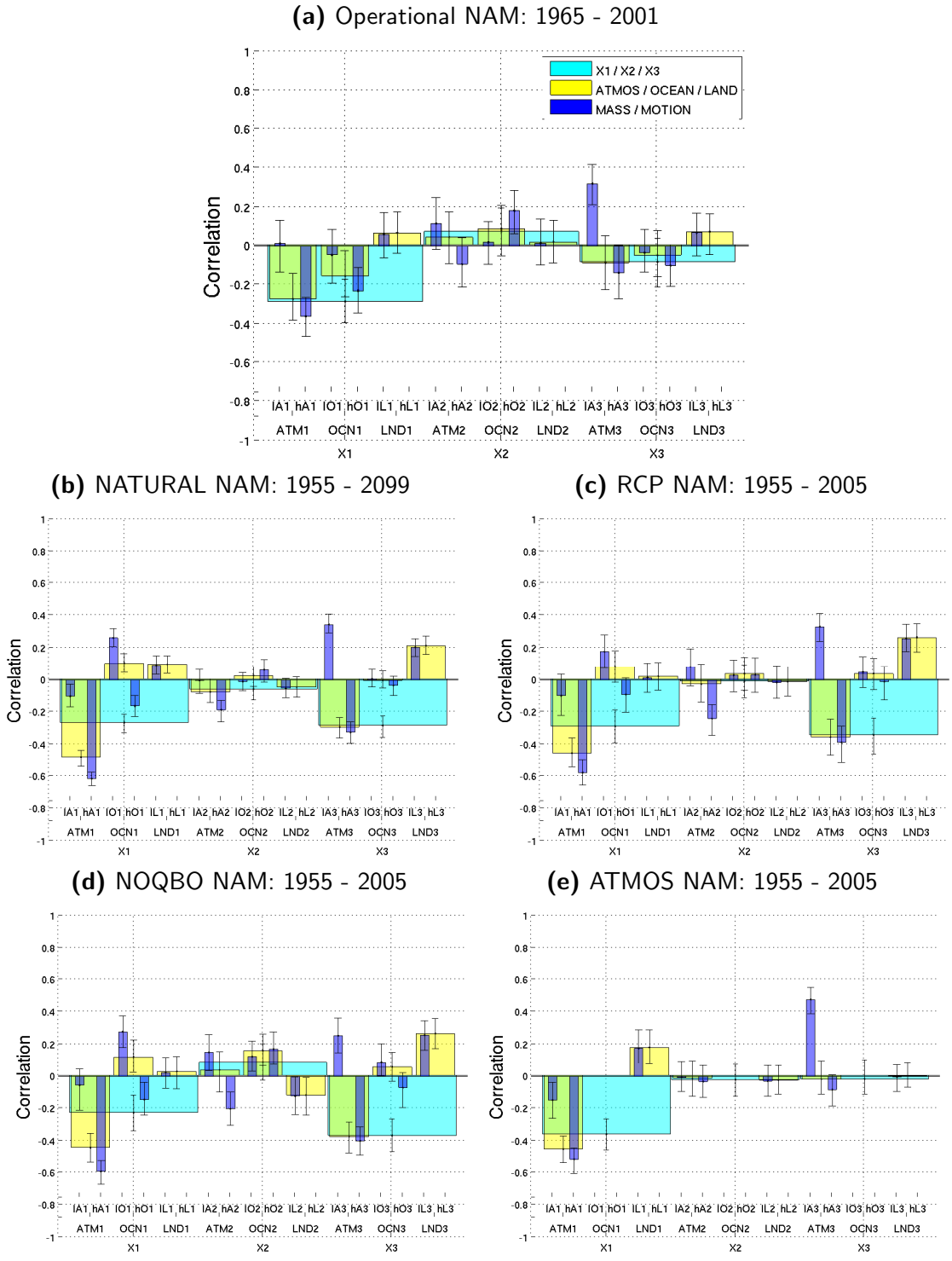

Figure 5.16: Correlation of the NAM index with operational data (a) and all CESM experiments (b-e). The wide cyan bars represent correlations with $\chi_{1,2,3}$ (same as in Figure 5.15 a). The yellow bars represent correlations of the subsystems atmosphere (ATM), ocean (OCN) and land (LND) for all three components $\chi_{1,2,3}$. The slim blue bars split the subsystems into mass (I) and motion (h) components. The error bars mark the 99% confidence interval.

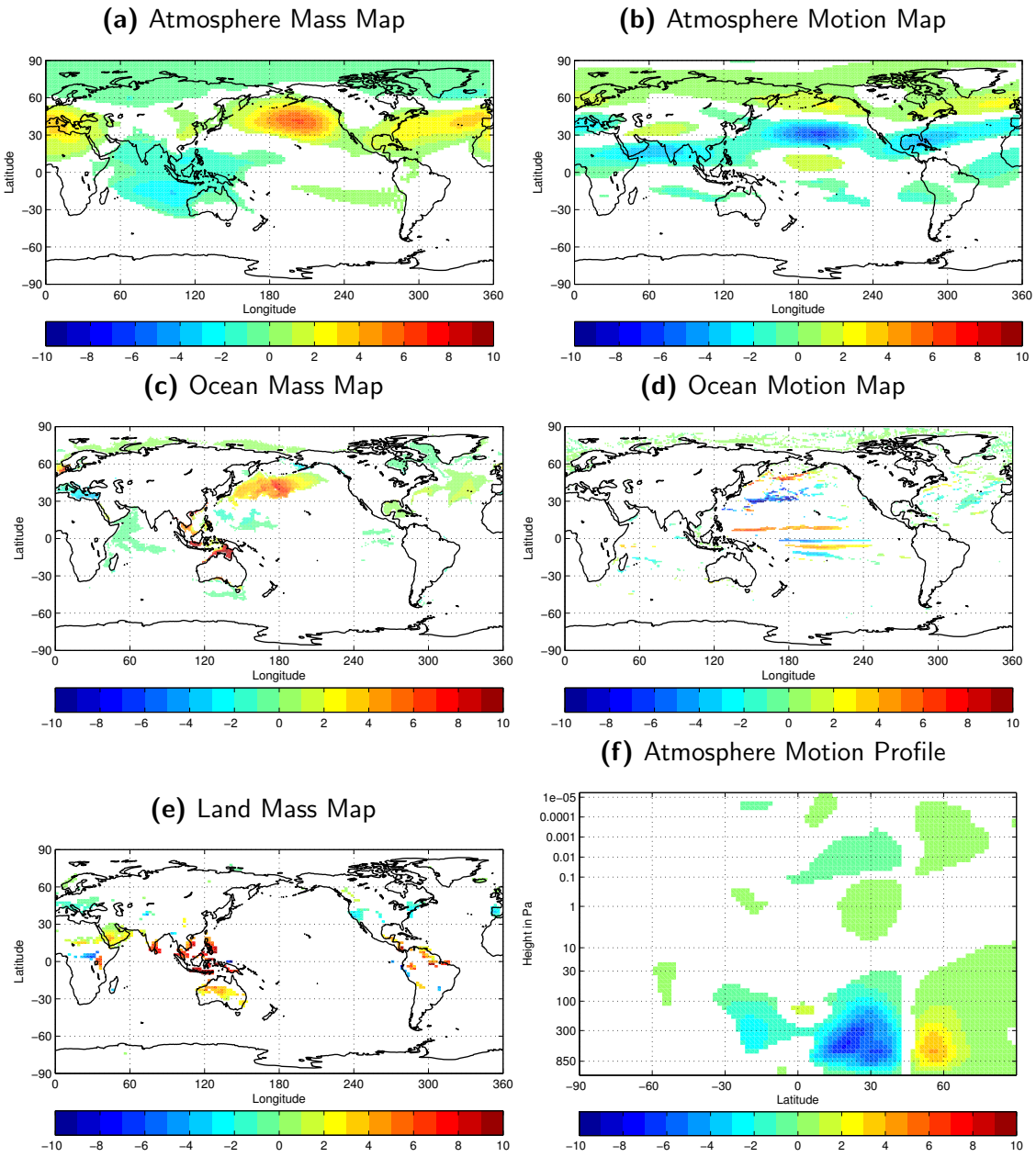

Figure 5.17: $NAM_{max} - NAM_{min}$ composites of the ERE maps (atmosphere, ocean, land) of the third component of experiment RCP. Values are normalized by the field standard deviation. Positive pressure anomalies in the North Pacific (a) are related to easterly winds around 30°(b) causing easterly ocean current anomalies (d) and ocean mass anomalies (c) further north. The wind profile is dominated by the pacific sector.

between both parameters. However, the synthetic and the operational NAM represent mass transport from the north pole towards higher latitudes causing positive correlations with IA_3. The associated weighting function is only lateral dependent neglecting all sectorial differences. The synthetic NAM - IA_3 correlations agree well with the operational data, indicating that the total NAM related lateral mass variations are of the same magnitude.

Figure 5.17 illustrates the NAM composites of the ERE maps for the third component. Analyzing the ERE maps for the first two components would not gain any further insight since the modeled mass variations remains the same (as for the previous analysis) but now also the index - here the NAM - defining the composites stays the same. This means the only differences between the NAM related χ_1, χ_2 and χ_3 maps is the initial weighting function (cf. Figure 2.1). Therefore, it is sufficient to visualize only the effect on χ_3.

Figure 5.17a shows additional to the NAM typical northern hemispheric surface pressure features also negative atmospheric mass anomalies in the equatorial Indian ocean, which is typical for the negative ENSO phase (cf. Figure 3.8). This is a footprint of the unrealistically high relation between ENSO and NAM within the CESM experiments.

The NAM related atmosphere motion signal in Figure 5.16 agrees better with the operational data for all three components (hA_i). Figure 5.17 b and f show the link between the NAM and the zonal winds, which feature easterly anomalies during a positive NAM phase. These anomalies translate directly into negative correlations for the hA_3 component. The Pacific region features stronger wind anomalies compared to the Atlantic sector leading to negative correlations of hA_1. Here CESM again exaggerates the operational values.

The synthetic ocean signal shows significant correlations only for χ_1. The NAM related negative ocean motion correlation is clearly related to the North Pacific current at 30°N (Figure 5.17d). Here, we also find a connection to the equatorial currents and counter current in the Pacific. This represents again an unrealistic high connection between ENSO and NAM within the CESM model.

The oceanic ERE mass map (Figure 5.17c) shows a clear NAM related signal in the North Pacific, which dominates the IO_1 correlation. In chapter 6 these oceanic mass variations are related to the prevailing wind and pressure system. Additionally to the NAM related North Pacific mass signal, we find positive ocean mass anomalies between the Indian and Pacific ocean. This feature is related to increased precipitation in this region, which causes also positive mass anomalies on land (Figure 5.17e), which again is related to La Niña. The ocean orography most likely permits a realistic outflow of the additional ocean mass leaving an unrealistic positive ocean mass signal here. However, a sound physical explanation for these oceanic mass anomalies requires a detail analysis of the mass transport within this region and is not part of this study.

Summarizing, the NAM affects all components, including the atmosphere, ocean and land. In more detail we find a positive pressure anomaly, which coincides with easterly wind anomalies on the south side at around 30°N. The atmosphere triggers an oceanic reaction including westward ocean current anomalies and positive ocean mass variations (cf. Figure 5.17). This scenario is described in more detail in chapter 6.

5.4.2 ENSO

Comparing the total ERE correlations with the ENSO index (Figure 5.15b) shows significant values only for the third component χ_3. Here, the IERS observations show the smallest correlations (≈ 0.25). The operational data shows twice the value, which is even higher for the synthetic data. Experiment NOQBO shows by far the highest correlations. This is clearly related to the fact that χ_3 is dominated by the atmosphere motion (hA_3), which experiences interannual variability related to the subtropical jet and the QBO (cf. Figure 5.13). Without a QBO signal, this hA_3 variation is dominated by the subtropical jet stream alone and thus it is highly related to ENSO.

Despite the insignificant total correlations between the ENSO index and $\chi_{1,2}$, Figure 5.18 reveals significant values for the subcomponents. For example, the atmosphere motion component is always positively correlated with the ENSO index. However, this is balanced by negative atmosphere mass correlations, which cancel out the positive motion values.

One significant disagreement lays within the third ocean mass component, which shows negative values for the synthetic data and slightly positive values for the operational data. Figure 5.19 shows that this is again related to mass anomalies in the oceanic vicinity of Indonesia. The reverse anomalies were already present in Figure 5.17c indicating again a lacking capability of the ocean model to compensate the strong precipitation during a La Niña event in this area. This is again likely related to limitations in the ocean orography.

(a) Operational ENSO: 1965 - 2001

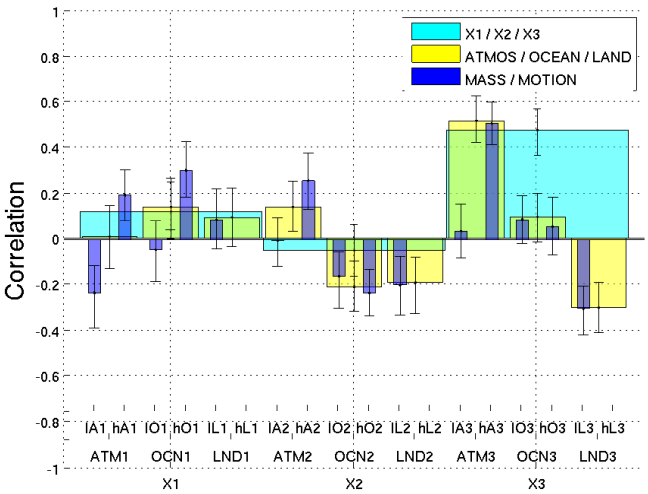

(b) NATURAL ENSO: 1955 - 2099

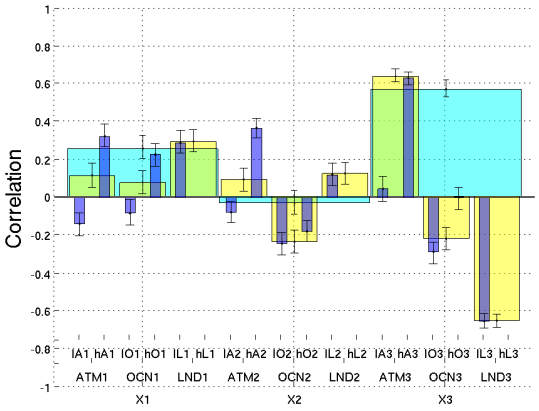

(c) RCP ENSO: 1955 - 2005

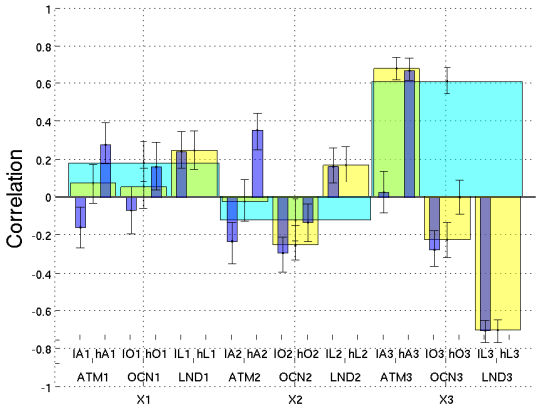

(d) NOQBO ENSO: 1955 - 2005

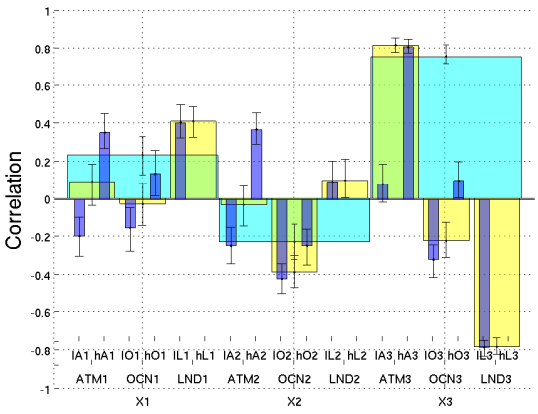

Figure 5.18: Same as Figure 5.16, but here for ENSO.

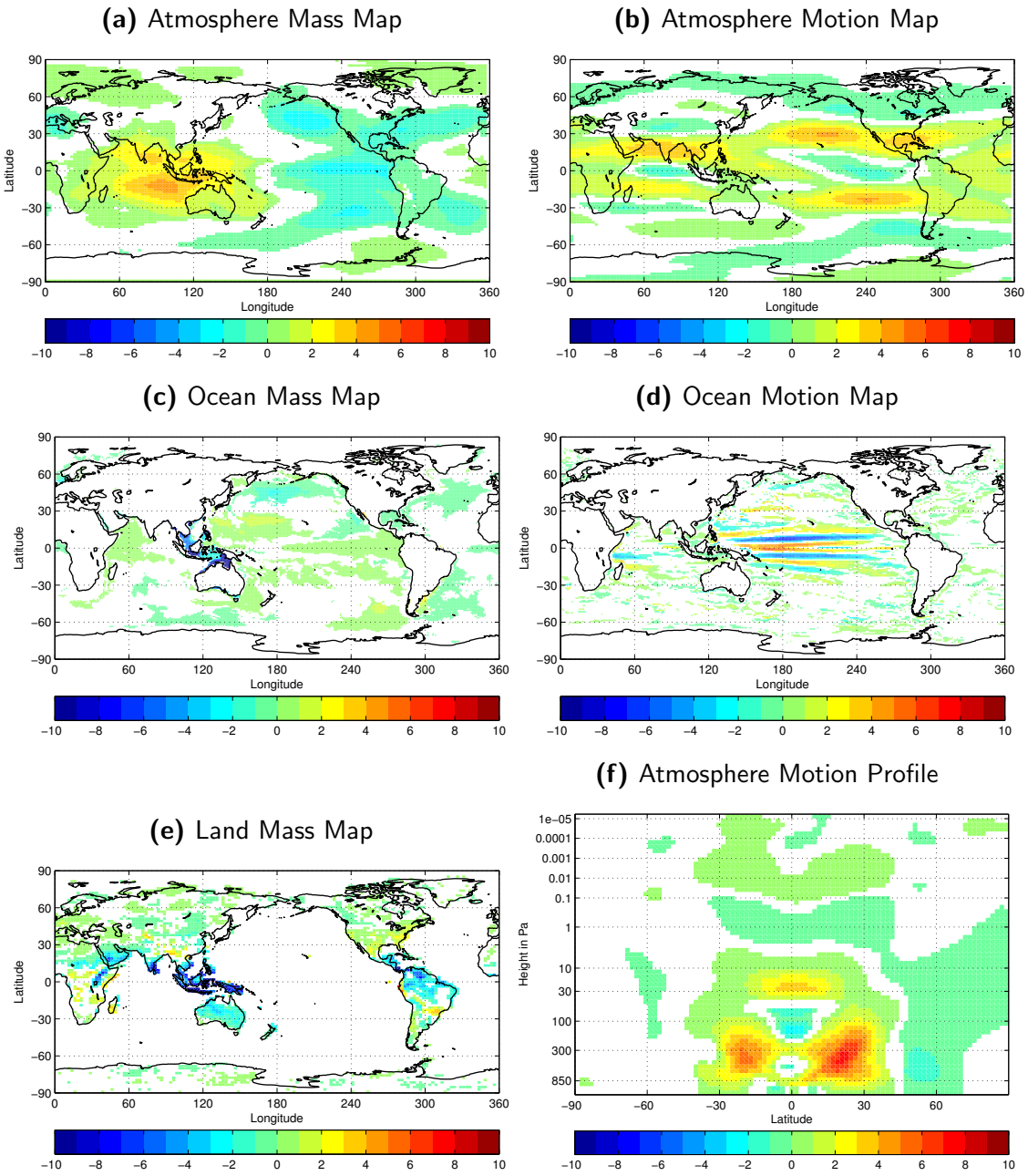

Figure 5.19: Same as Figure 5.17, but now for the composites El Niño minus La Niña.

5.5 Summary

Based on the scientific goals formulated by Schuh et al. (2003), the question was raised whether Earth rotation allows to validate the integrated behavior of a climate system model. To answer this question, this chapter analyzed the Earth Rotational Excitation (ERE) for modeled (CESM), operational (GFZ) and observed (IERS) data. First, the total annual cycle is discussed, showing good agreements between the operational data and observations. This includes the total average annual cycle as well as its variations (cf. Figure 5.1). The modeled EREs agree with the observed and operational annual cycle. The strongest variations are found in the atmosphere mass component over the ocean, which is barometrically corrected and thus does not contribute to the total annual cycle of the EREs. The modeled annual cycle of the oceanic mass component is not present in the operational data and can be attributed to mass variations in the southern Indian ocean (cf. Figure 5.5b). The continental hydrosphere features a similar amplitude of the annual cycle indicating similar amounts of total precipitation, however, the modeled phase and duration of the peak differ, indicating a distinguished water discharge behavior. Finally, the annual cycle of the third component is dominated by the atmospheric motion (cf. Figure 5.6). Here, CESM underestimates the annual cycle indicating a too weak developed asymmetry between the northern and southern hemispheric subtropical jets.

Summarizing, there is no single answer to the initial question. While it is not possible to evaluate a whole climate model upon Earth rotation data alone, the data itself reveals possible problems immediately. For example, the too weak modeled annual cycle of χ_3, points towards uncertainties in the modeling of the atmospheric zonal wind. The combined analysis of the total modeled excitation together with contributions of the subcomponents and the excitation maps allows to further encircle problematic regions, especially when comparing to the operational (GFZ) excitations.

Answering the initial question regarding the separation of natural from anthropogenic variations and attributing this to geodetic observations, we find no evidence of a significant anthropogenic impact on the excitation within our modeling experiments. However, there are significant differences, which can be attributed to natural variations. For example, experiment ATMOS which is forced with a climatological data ocean, features no interannual subtropical jet variations (cf. Figure 5.13). Comparing to observed Earth rotation data, this highlights the importance of interannual ocean modes, for example related to ENSO, for realistic interannual atmospheric variations. The same holds true for nudging the QBO. Realistically modeled Earth rotation excitations depend on the inclusion of both sources of natural variations.

Finally, this chapter investigates the impact of NAM and ENSO on the subsystems and the total excitations. Here, interactions between the atmosphere mass and motion terms are found, for example, for the NAM in the North Pacific (cf. Figure 5.17 a and b). Especially the

atmospheric motion component directly influences the oceanic currents and with it the ocean mass pattern (cf. Figure 5.17 a and b). This answers the introductory question, whether it is possible to identify regions featuring particularly strong coupling, with a clear: yes. The upcoming chapter investigates the coupling effects between atmosphere and ocean in the North Pacific. In order to validate the modeled interactions, geodetic observations of the gravity field as well as atmospheric reanalysis data is used.

Chapter 6

North Pacific Mass Variations

6.1 Introduction

Ocean bottom pressure resembles the cumulated mass above a certain point of the ocean floor. This includes (a) the ocean mass, and (b) the atmospheric mass. Both measures are computed by integrating the ocean water and air density over the height. It is commonly accepted that low-frequency variations in the atmosphere are compensated by the ocean's surface. Accordingly, Wunsch and Stammer (1997) state that atmospheric low (high) pressure fields are inverse barometrically compensated by an increase (decrease) of the underlying Sea Surface Heights (SSHs). Thus, measuring the total mass of a column through the atmosphere and ocean (e.g., via GRACE) would gain no deviations, while measuring the SSHs (e.g., via Topex/Poseidon, hereafter T/P) would reveal a signal.

Atmospheric wind stress determines the transport of large-scale gyre circulation as described by Sverdrup's theory (Sverdrup, 1947). He stated, that the curl of the wind stress is directly related to the underlying ocean mass flux. A short version of its derivation and its implications are described in section 2.2. Time variations in the surface wind stress curl cause transport variations in the ocean gyre that are geostrophically accompanied by ocean bottom pressure variations. In the Northern Hemisphere this means a net ocean mass transport perpendicular to the right of the prevailing wind field. This mass movement causes ocean bottom pressure anomalies as well as SSH variations and can thus be observed via GRACE and T/P.

Based on the results of a primitive equation model, Ponte (1999) found that ocean bottom pressure variations are especially strong in the western part of the subpolar gyres. Bingham and Hughes (2006) report on GRACE observed ocean bottom pressure variations in the North Pacific. These mass variations are observed for over a decade now and several studies indicate the relation to the prevailing winds (Chambers, 2011; Song and Zlotnicki, 2008). Nevertheless, the underlying physical process guiding the oceanic response is discussed in less detail. Sverdrup's theory provides the best established approach but it is not clear, what are the

discrepancies between observations and theory in terms of signal strength. Qiu (2003) finds a substantial part of the NP ocean mass anomalies explained by the Pacific Decadal Oscillation (PDO). Further, Song and Zlotnicki (2008) show the significant ocean mass variations in the NP related to the prevailing Wind Stress Curl (WSC). However, they do not find a relation to the El Niño Southern Oscillation (ENSO). This connection was introduced by Chambers (2011), who found the interannual ocean bottom pressure variation correlated to ENSO.

All studies agree on the relation of the WSC to ocean mass variations. In this context the study of Li and Wettstein (2011) is especially interesting, since they discuss atmospheric jet variability, including the connections to the surface winds. They found that the Atlantic jet position and strength is primarily eddy driven, while the Pacific jet is additionally thermally driven. Thus, the jet and the surface winds of the Pacific sector depend on mid- to high-latitude processes (eddy driven) and on equatorial processes (thermally driven).

Based on the above mentioned studies, this work establishes a connection between the NP ocean mass variation and the prevailing wind fields based on monthly data. Further a connection to modes of global climate variability, such as the Northern Annular Mode NAM and the El Niño Southern Oscillation ENSO is established. We find a comprehensive connection between the NP surface pressure, the associated winds and the induced oceanic mass anomalies. First we analyze the theory upon modeling experiments with the Community Earth System Model - CESM and then project the results on ERA-Interim data in order to reconstruct the observed GRACE observations. We hereby assume that the physical processes modeled by CESM represent realistic physical features. Based on the previous analysis it is clear that the total surface pressure variation in the North Pacific region is overestimated by CESM. However this discrepancy is not relevant for investigating the coupling processes between the atmosphere and the ocean. Solely the magnitude of the signal requires further validation.

6.2 Ocean mass anomalies in CESM

This analysis is performed using the NATURAL experiment, which experiences only natural variations for 145 model years. The other two experiments using an interactively coupled ocean (RCP,NOQBO) produce the same results and are thus not separately presented.

In order to compute the ocean mass anomalies we integrate the ocean density over the whole water column for each grid point. The ocean bottom pressure is detrended and high pass filtered with a cutoff frequency at 7 years. The seasonal cycle is reduced by subtracting the average annual cycle of the whole model period for each grid point. Figure 6.1a shows the standard deviation of the deseasonalized oceanic mass anomalies. In the North Pacific region we find the strongest ocean mass anomalies of up to 3.5 hPa at 177°E and 43°N. This location is marked by a blue x in Figure 6.1a. In the vicinity of this point we find large scale

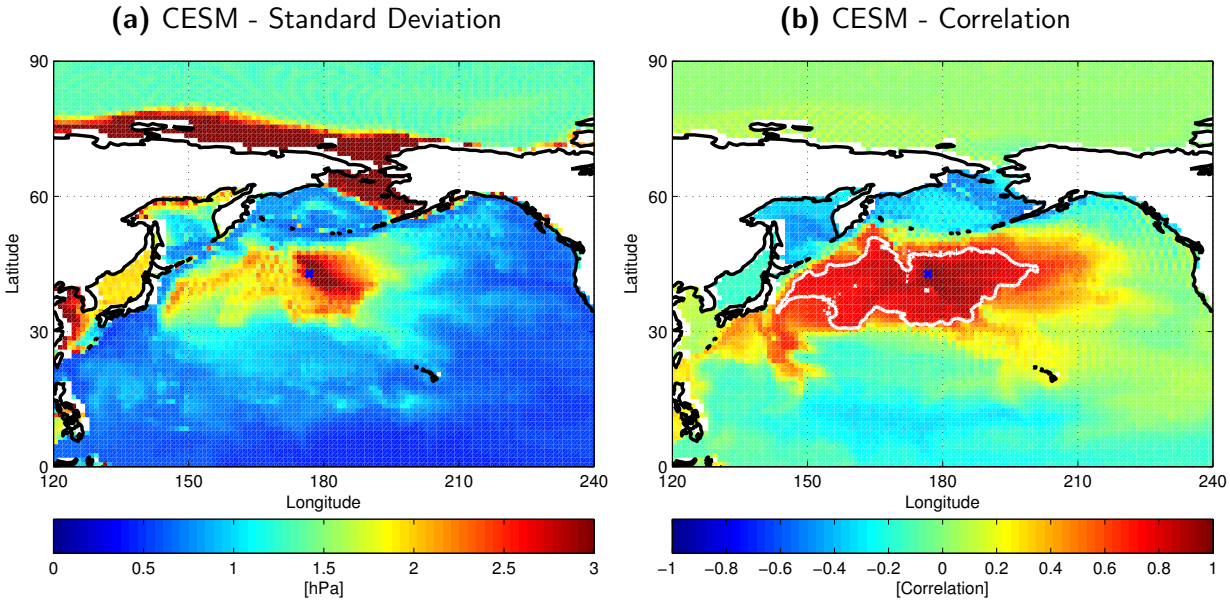

Figure 6.1: Left: Standard deviation of the CESM modeled ocean mass anomalies for 145 years of deseasonalized monthly mean data for the North Pacific region. The blue x is located at the position of the highest standard deviation. Right: the correlation of the same ocean mass anomalies with the point of the highest standard deviation (marked as x). The dashed white line represents a correlation of $r = 0.7$.

mass variations exceeding 2 hPa of standard deviation. These model results are in agreement with observations (cf. Figure 6.6) and other modeling and observation studies (Chambers, 2011; Song and Zlotnicki, 2008).

Figure 6.1b shows the correlation map of the anomalous oceanic mass variations with the location of highest mass variation, as described above (the blue x at 177°E, 43°N). One can clearly see, that the North Pacific mass variation reacts homogeneously as one signal, covering the western and central Pacific between 30°N and 50°N. Thus we can approximate one time series representing the NP mass anomaly by the area weighted average over this region. In more detail, we use the area with a correlation exceeding $r = 0.7$ (white iso line in Figure 6.1) that additionally experiences a standard deviation of at least 1.

Now the first question is, whether we are able to explain this time series with the prevailing winds? In order to quantify the wind driven share of the oceanic mass anomalies, we first investigate the anomalous Mean Sea Level Pressure (MSLP) and the associated surface wind anomalies.

For separating independent pressure and wind patterns we compute the Empirical Orthogonal Functions (EOF) of the MSLP anomalies in the area between 120°and 240°E, north of the equator. We then use the associated principal components and regress them onto the wind fields (separately for zonal and meridional components) in a simple least squares sense. Figure 6.2 shows the four significant EOF patterns of the MSLP anomalies in hPa. The associated

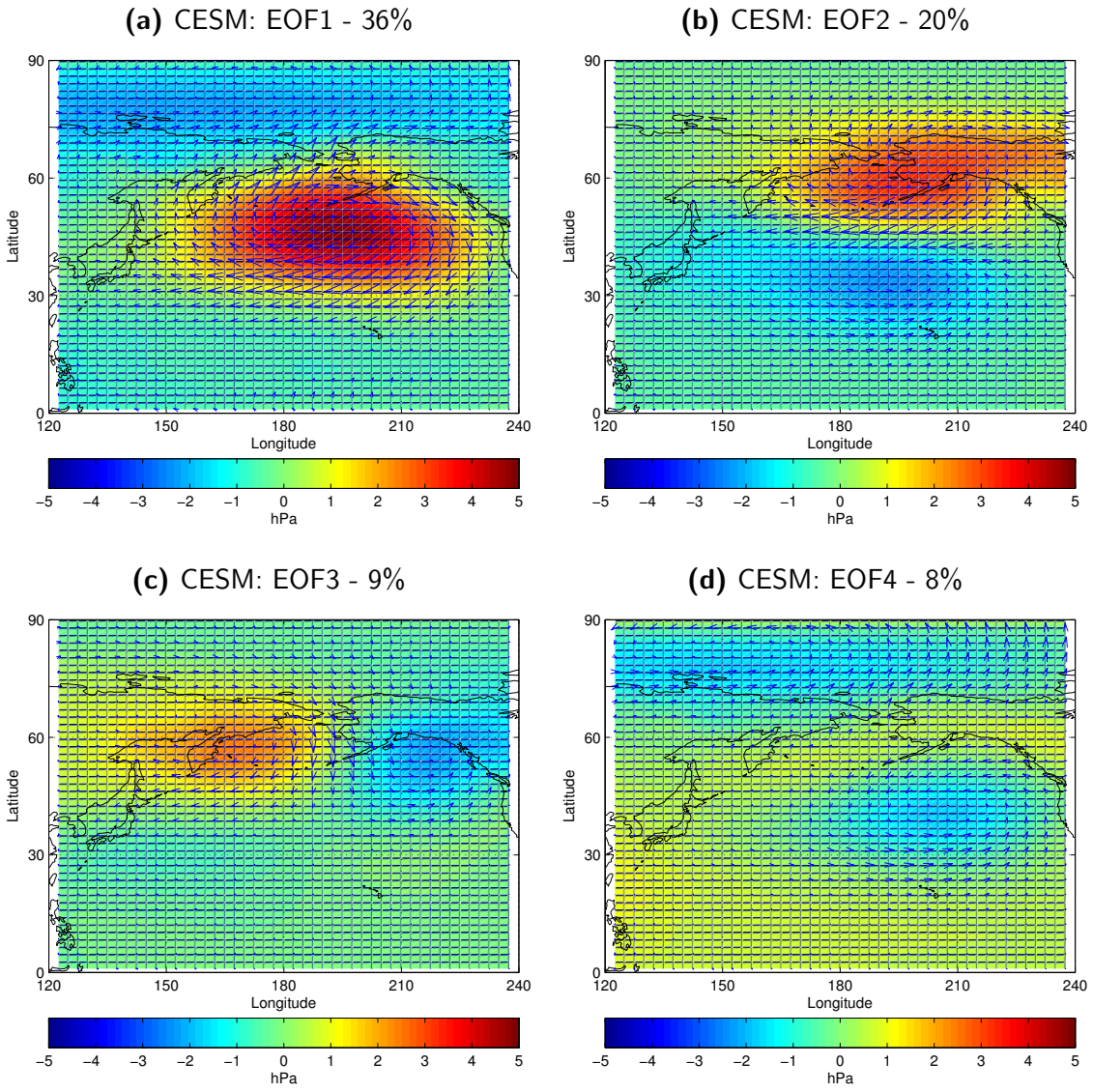

Figure 6.2: First four EOFs and their associated surface wind signal for 145 years of deseasonalized mean sea level pressure as modeled by CESM. The EOFs are computed in the depicted frame from the equator to the pole and from 120°E to 240°E. The colored shading represents the MSLP-EOF amplitude in hPa and the vectors the associated regression result of the surface wind field. All scales are equal and can be compared among each other.

Principal Components are normalized by their standard deviation, leaving the EOF patterns directly comparable in amplitude. The arrows show the associated wind anomalies in the same scale for all four EOFs. Thus all subfigures of Figure 6.2 are directly comparable.

The first EOF of the MSLP (Figure 6.2) explains about 36 % of the variance and exhibits a clear Aleutian related pressure system. Here the positive pressure anomaly is accompanied with negative anomalies in the polar region. This represents a negative NAM for the Pacific sector. Since the NAM is commonly defined as the principal component of the first EOF of the MSLP north of 20°N (Baldwin and Thompson, 2009; Thompson and Wallace, 1998) for the whole NH, we expect a certain degree of resemblance between the Pacific NAM and the total

NH NAM. Thus the correlation between the NAM and the Pacific NAM is high (≈ 0.898). The related wind field shows a clear anticyclonic pattern over the North Pacific, including a strong easterly component at around 30°N (Figure 6.2).

The second EOF shows a lateral bipolar pattern explaining about 20 % of the total variance. The positive maximum is located over Alaska, while the negative maximum is located in the central Pacific around 40°N. The associated wind patterns are cyclonic over Alaska and anticyclonic over the central Pacific. Especially the western part of the low pressure anomaly is prolongated towards Japan, resulting mainly in westerly wind anomalies around 50°N and predominantly easterly anomalies around 25-30°N.

The third EOF shows a meridional bipolar pattern, explaining about 9 % of the total variance. The center of action is further north around 60°N, with positive anomalies at the coastal region of the Kamchatka peninsula and negative anomalies at the south coast of Alaska. In general this EOF is located closer to the coastal areas, barely affecting the open ocean. There is no consistent wind pattern for the central north Pacific. We find easterly anomalies in the western and westerly anomalies in the eastern part of the mid-latitudinal Pacific. Further, there are mainly southerly anomalies in the tropical Pacific.

The fourth EOF is the last significant one, explaining about 8 % of the total variance. It features negative pressure anomalies in the east Pacific and in the Arctic Ocean. The dominant wind pattern is cyclonic, showing distinct westerly anomalies between 25°- 30°N.

Together the first four EOFs explain about 74% of the total MSLP variance in the depicted area. Comparing the four different surface wind fields over the NP yields comparable cyclonic features for EOF two and four with westerly wind anomalies around 30°N. Additionally EOF 2 shows strong easterly wind anomalies around 50°N, which is close to the Aleutian islands and thus close to the coast, where Sverdrup's Theory is not applicable any more. In contrast to EOF 2 and 4, EOF 1 shows a strong anticyclonic wind pattern, including strong easterly wind anomalies around 30°N. The 30°latitude is important, since it marks the southern boundary of the ocean mass anomalies. Assuming a relation to the prevailing winds, would consequently be located here and further north.

We now have the four dominating pressure and wind patterns for the North Pacific and their related time series together with the time series for the North Pacific ocean mass anomalies. In order to verify the initial assumption of wind driven ocean mass anomalies, we now use the four principal components in a multiple linear regression to reconstruct the North Pacific mass anomalies. The principal components are by definition uncorrelated among each other and thus are highly qualified for a multiple linear regression. Additionally, we include other indices e.g.: a constant, a trend, an annual sine and cosine as well as an index representing the QBO and the solar cycle. The first four indices are for statistical reasons, while the last two represent possible external forcings of the North Pacific mass variations in CESM. Especially

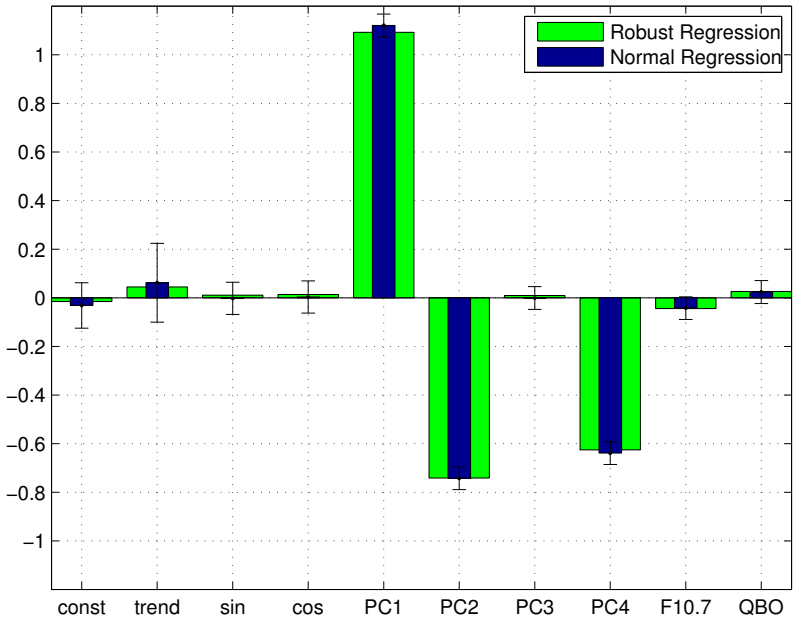

Figure 6.3: Regression coefficients for reconstructing the CESM modeled oceanic mass anomalies from Figure 6.1. The blue bars denote the normal regression results in a least-squares sense, including error bars on the 99 % significance level. The green bars represent the coefficients for the robust multiple linear regression, which excludes outliers.

the last two indices are not by definition independent from the rest, but might experience some correlation. The question why we do not include climate indices representing the NAM, ENSO or any other phenomenon can be answered with the fact that these climate indices are not independent among each other (eg., NAM and ENSO are correlated) or among our PCs (eg., NAM and PC1 are correlated). Thus they would compete against each other trying to explain the same variance, leaving the result hard to interpret. Instead we use only the here suggested indices and relate them later to different climate phenomena.

Figure 6.3 shows the results of the Multiple Linear Regression (MLR). Here the dark blue bars denote the simple least squares solution, including error bars at the 99% significance level. The green bars represent the robust regression result, using a bisquare weighting function, omitting outliers [Holland and Welch, 1977]. Both MLRs yield the same result: The principal components one, two and four are most important for reconstructing the time series of the NP mass variation. Neither regression finds a significant constant, trend or annual cycle. The QBO and the solar cycle indices are of no significance either. Likewise the third principal component appears to have no effect on the oceanic mass variations. Conducting a MLR excluding all non-significant indices yields similar amplitudes for all the remaining three indices. Thus we use the principal components one, two and four for the reconstruction of the oceanic mass variations.

Figure 6.4 shows the reconstruction using the three significant indices (green) and compares them to the time series of the NP mass variation (blue). Obviously, the regression captures all

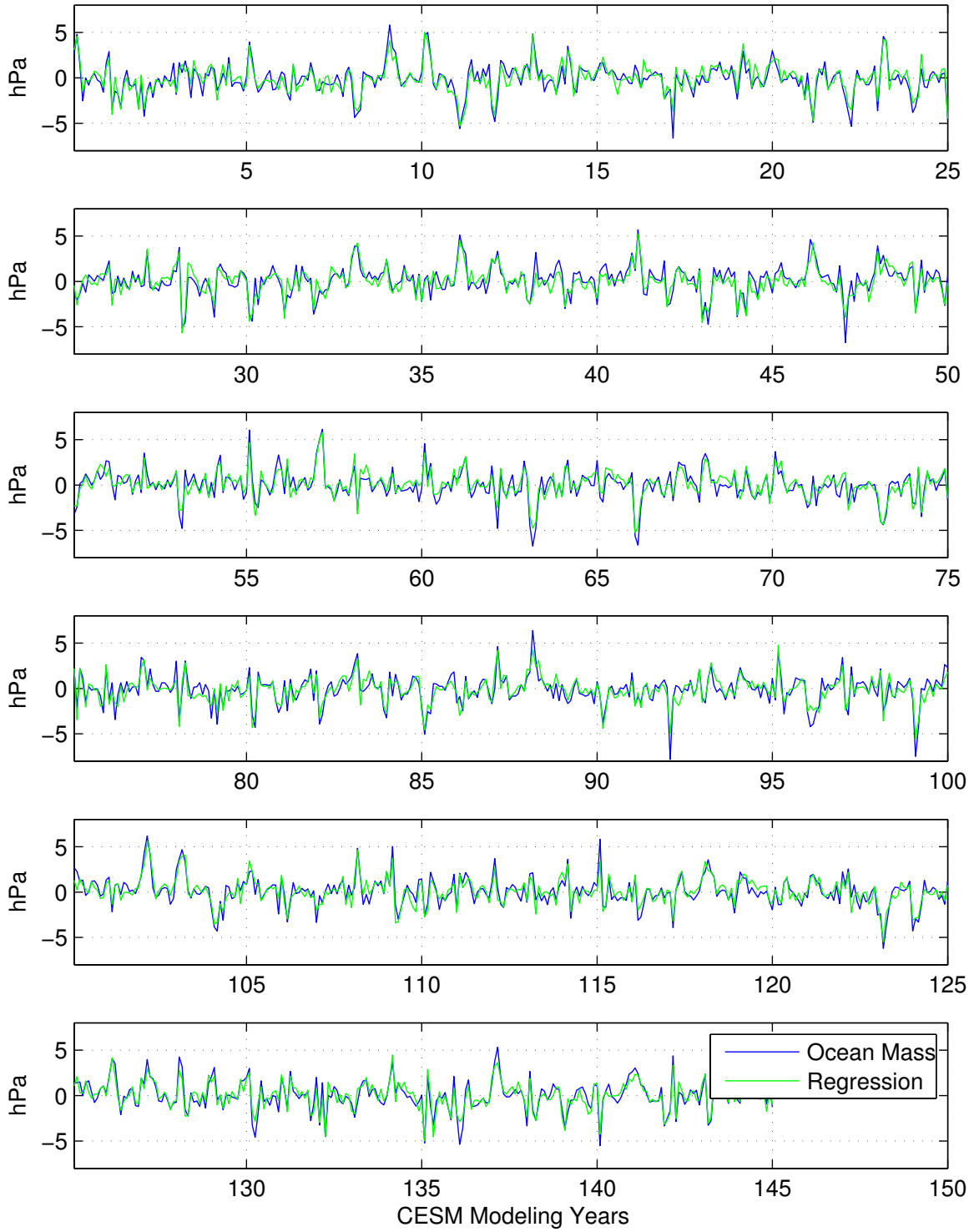

Figure 6.4: The blue line represents the CESM modeled ocean mass anomaly computed from the highlighted area in Figure 6.1 in hPa. The green line shows the regression result using the significant regression factors from Figure 6.3. The correlation between both lines is r = 0.8924.

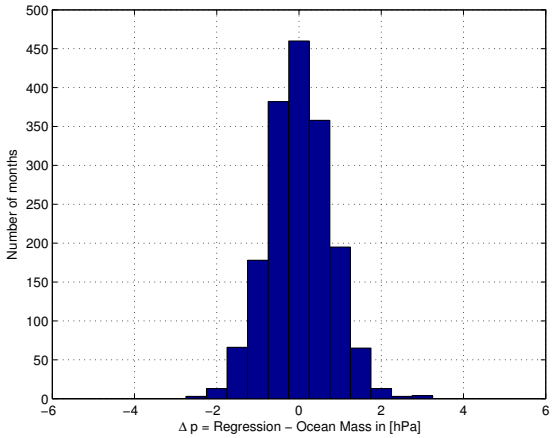

Figure 6.5: Histogram of the residuals between the wind based regression results and the ocean mass anomalies (cf. Figure 6.4). The residuals are normally distributed indicating white noise.

major features including their amplitude for the whole 145 modeling years. Both time series are highly correlated with r=0.8924. This regression result shows a clear relation between the interannual NP mass variation and the prevailing surface pressure and wind fields. Thus the assumption of wind driven barotropic ocean mass anomalies is justified.

For a better understanding of the remaining residual, Figure 6.5 shows the histogram of the ocean mass anomalies (blue line) minus the regression result (green line) for the whole 145 years. The histogram is normally distributed indicating white noise in a Gaussian sense. This means that the wind and pressure based regression results captures most of the physically explainable ocean mass variations.

6.3 Projecting CESM EOFs on ERA-Interim data

In order to validate the CESM results we now employ our findings on observations. Thus we first need to compute a time series for the observed mass anomalies in the NP. Here we use results of the Ocean Model for Circulation and Tides - OMCT that has been forced with ERA-Interim data for 22 years starting in January 1989 and lasting till December 2010. Additionally, we use the fully available 6 years of GRACE observations for the years 2005 to 2010. In more detail we use RL04 and RL05 solutions, provided by the GFZ. For more details on the data see chapter 2. The observations are processed in the same way as the CESM data, reducing the annual cycle and computing the standard deviation for all data sets. The result in hPa is given in Figure 6.6. For better comparison the CESM results are (again) shown together with the OMCT and the two GRACE results.

All four data sets show a similar amplitude of about 3 hPa standard deviation in the NP. The OMCT and GRACE RL04 show a bipolar pattern with two peaks, with an additional one located further west, south of Kamchatka. In the OMCT this peak has the same amplitude

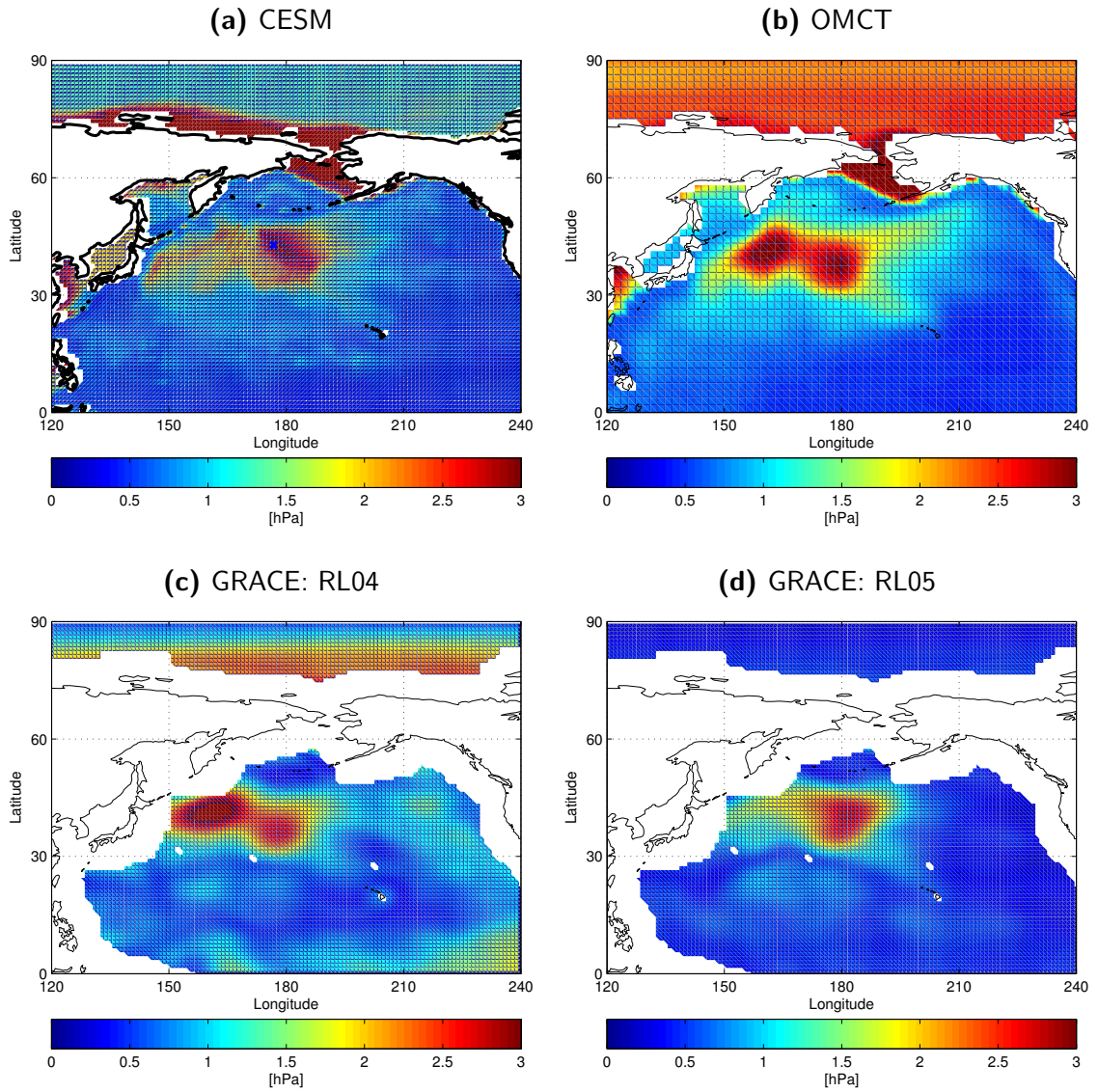

Figure 6.6: Same as Figure 6.1 (a): standard deviation of deseasonalized ocean mass anomalies for (a) CESM, 145 years (top left - same as Figure 6.1), (b) OMCT, 22 years (top right); (c) GRACE RL04, 6 years (bottom left); GRACE RL05, 6 years (bottom right) in hPa.

while the GRACE RL04 peak is bigger than the central Pacific mass anomaly. The GRACE RL05 and the CESM mass anomalies are similar in amplitude, shape and position.

For all four data sets we follow the processing steps of the CESM data, finding the location of the highest standard deviation (for the OMCT and RL04 we take the central Pacific peak) and correlate this with the surrounding mass anomalies. The result is shown in Figure 6.7. Again the iso-line with a correlation of 0.7 is highlighted. We now use these areas to compute a time series for all data sets regarding only locations with an initial standard deviation of at least 1 hPa.

We now have the time series for the NP ocean mass anomalies for all three data sets. Additionally, we need the atmosphere pressure and wind based reconstruction of the mass

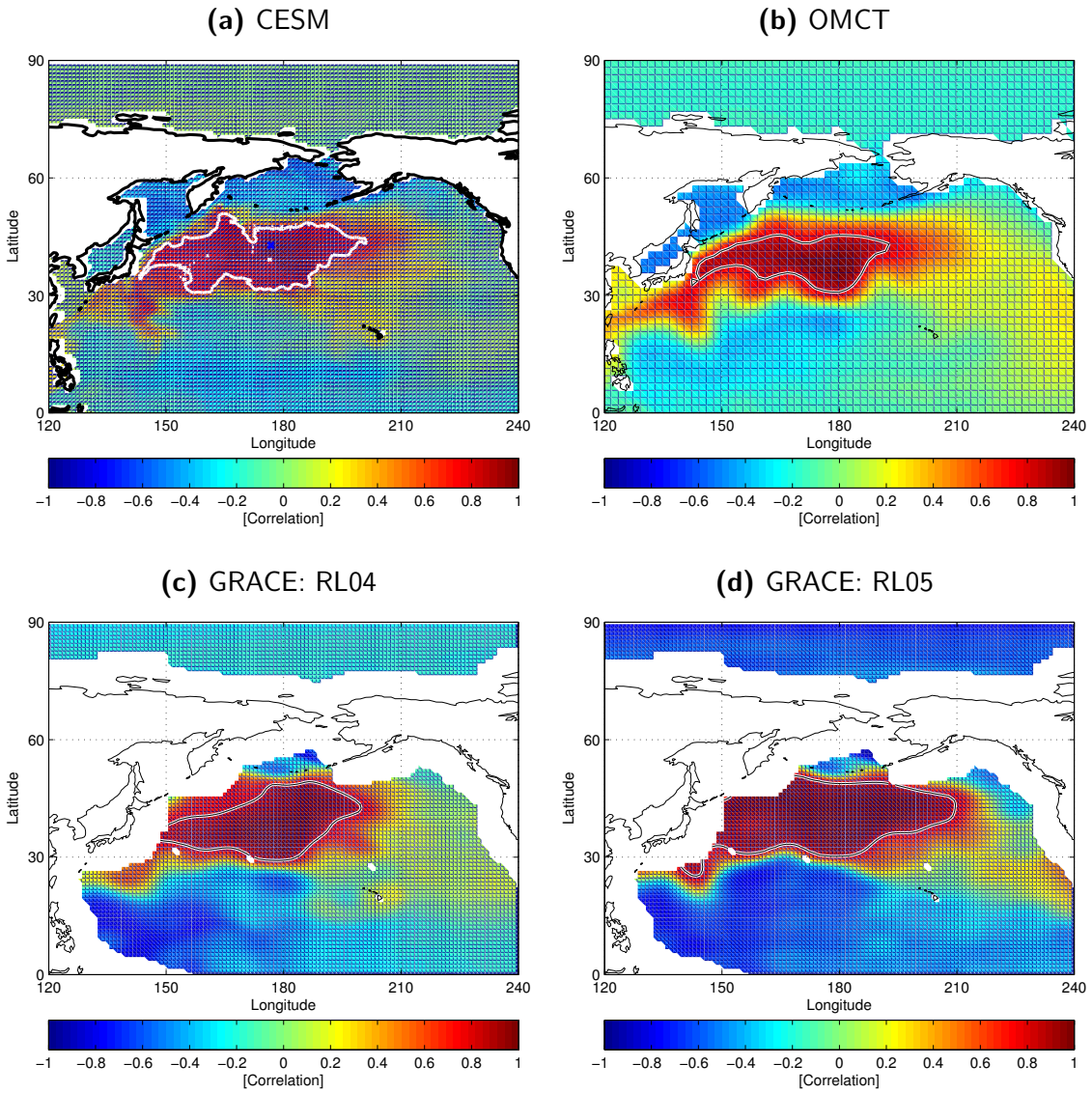

Figure 6.7: Same as Figure 6.1 (b): correlation of the ocean mass anomalies with the point of highest standard deviation for: (a) CESM, 145 years (top left - same as Figure 6.1), (b) OMCT, 22 years (top right); (c) GRACE RL04, 6 years (bottom left); GRACE RL05, 6 years (bottom right).

signal. As a reminder, for the CESM reconstruction we used the PCs of the first four EOFs of the deseasonalized MSLP field, together with a constant, a trend and a cosine and sine function. Significant influence is only contributed by the first, the second and the fourth EOF.

Therefore we take the EOF pattern of these three significant EOFs (cf. Figure 6.2) and project them on deseasonalized ERA-Interim data for the MSLP. For more details on the projection see section 2.4.3 on Empirical Orthogonal Functions. The result of this projection are three time series representing ERA-Interim and CESM based PCs, hereafter called PC_{ERA}^{CESM}. The three PC_{ERA}^{CESM} basically represent the state of the ERA-Interim data with respect to the CESM EOF patterns, for example: how much of CESM based EOF1 pattern is present in the ERA-Interim data at all time steps.

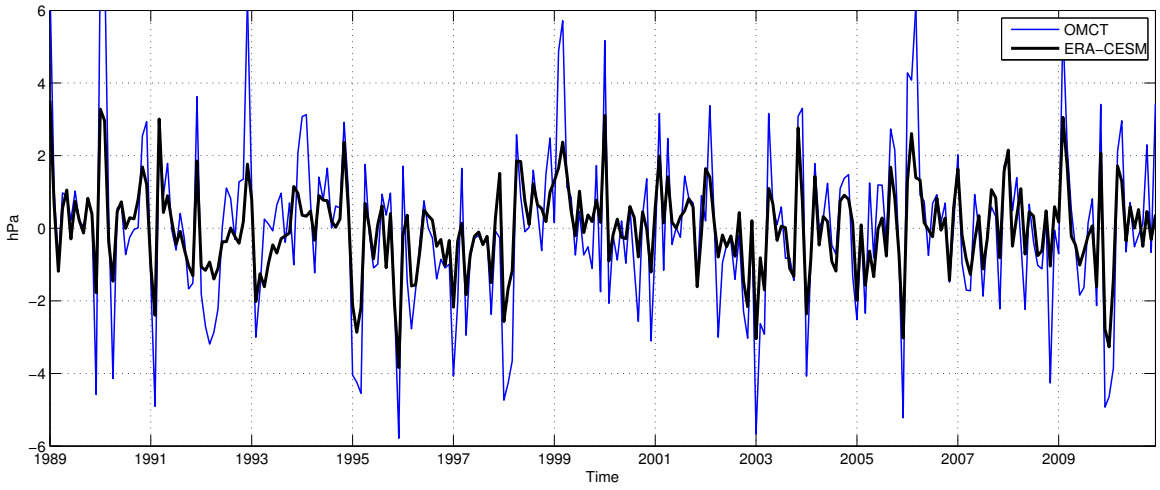

Figure 6.8: The blue line represents the ocean mass anomaly as computed by the ERA-Interim forced OMCT output from 1989 to 2010. The black line represents the regression results projecting the CESM EOFs on the ERA-Interim MSLP regressing the resulting PCs with the significant factors from Figure 6.3. The correlation between both time series is r = 0.87.

We now use these time series (PC_{ERA}^{CESM}) and multiply them with the associated CESM based MLR factors (Figure 6.3) and add them together as has been done for Figure 6.4. The result for 22 years is given in Figure 6.8. Here the blue line represents the computed time series of the OMCT mass anomalies. The black line represents the reconstruction using the PC_{ERA}^{CESM} and the CESM coefficients. There is an apparent agreement between both time series, which is underlined by the correlation of $r = 0.87$. Nevertheless, the regression result is underestimating the OMCT signal. This is especially true for extreme events as for example in the year 1990, 2003 and 2006. The regression result rarely exceeds the OMCT signal. However, the general agreement between both time series is obvious.

Figure 6.8 compares basically the agreement of two modeling results, one is unconstrained and free running (CESM) and the other forced with ERA-Interim data (OMCT). In figure 6.9 we now show additionally the mass anomaly signal of the latest two GRACE observation releases for the years 2005 to 2010. The black and blue lines are exactly the same as in Figure 6.8; while the red and green line represents the mass anomalies as observed by GRACE release 4 and 5, respectively. Again the agreement between all four curves is evident. Major peaks and dips are present in all four time series. However, for extreme events such as in the beginning of 2006 and 2009 we find the regression results in good agreement with the GRACE observations, while the OMCT shows a stronger signal. For negative mass anomalies, for example in late 2005 and between 2009/2010 the GRACE observations agree better with the OMCT results, while the regression shows weaker amplitudes. The correlations between all four time series for the shown 6 years is given in Table 6.1. Note that the correlation between the full OMCT time series and the regression results stays the same ($r = 0.87$) for the shorter

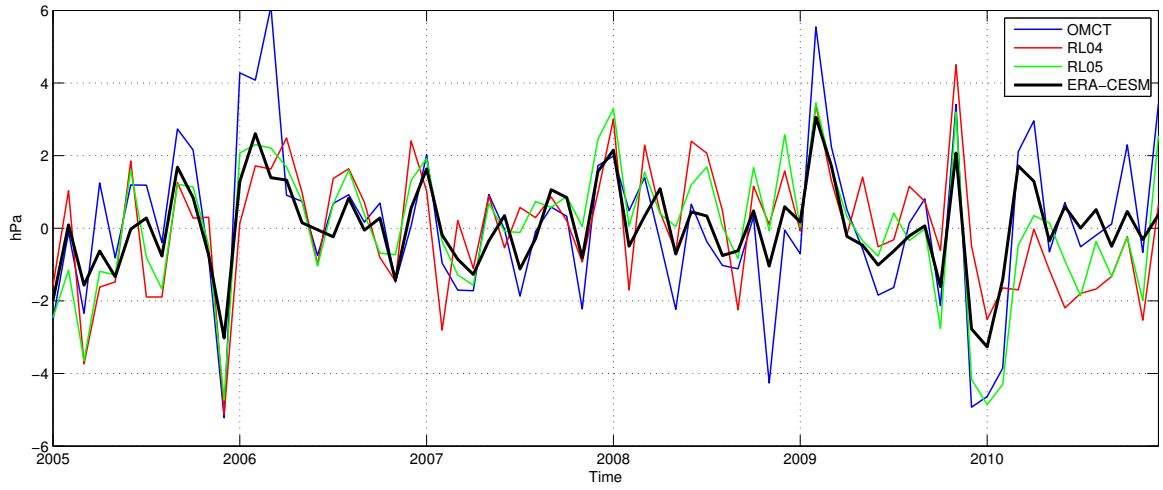

Figure 6.9: Same as Figure 6.8 from 2005 to 2010, additionally including the mass anomalies as observed by GRACE. RL04 (red) and RL05 (green). Correlation between the regression result (black) and (a) RL04: r = 0.64; (b) RL05: r = 0.83; and (c) 6 years OMCT: r = 0.87.

Table 6.1: Correlation between observed mass anomalies and regression results, corresponding to Figure 6.9.

CORR	RL04	RL05	OMCT	REG
RL04	-	0.80	0.56	0.64
RL05		-	0.77	0.83
OMCT			-	0.87

6 year period. It is also worth noticing, that RL04 is highly correlated with RL05 ($r = 0.8$) but that RL05 shows significantly higher correlation with the OMCT (RL04: $r = 0.56$ vs. RL05: $r = 0.77$) and the regression results (RL04: $r = 0.64$ vs. RL05: $r = 0.83$). Knowing that RL05 experiences a significantly lower error than RL04 (Dahle et al., 2012) allows to conclude, that the regression results as well as the OMCT mass anomalies represent indeed a physical signal that is observed by GRACE. Knowing that the RL05 error is still about a factor of eight higher than the predicted GRACE error raises the assumption that with better releases the correlation between the GRACE observed ocean mass anomalies and the modeled (OMCT) and predicted (CESM-ERA) will further increase.

The histograms of the residuals between the regression results (black line) and mass observations (OMCT, RL04, RL05) are shown in Figure 6.10. The residuals for the full time series of the OMCT appears to be normally distributed, with a few positive outliers exceeding 4 hPa. For the shorter period (2005 - 2010) one can see a clear peak, slightly on the negative side between -0.75 and -0.25 hPa. This indicates a general offset between both time series for this specific period. However, the general shape indicates again a normal distribution. The sample size for the 6 years of monthly data is only 72 months, therefore the histogram is under sam-

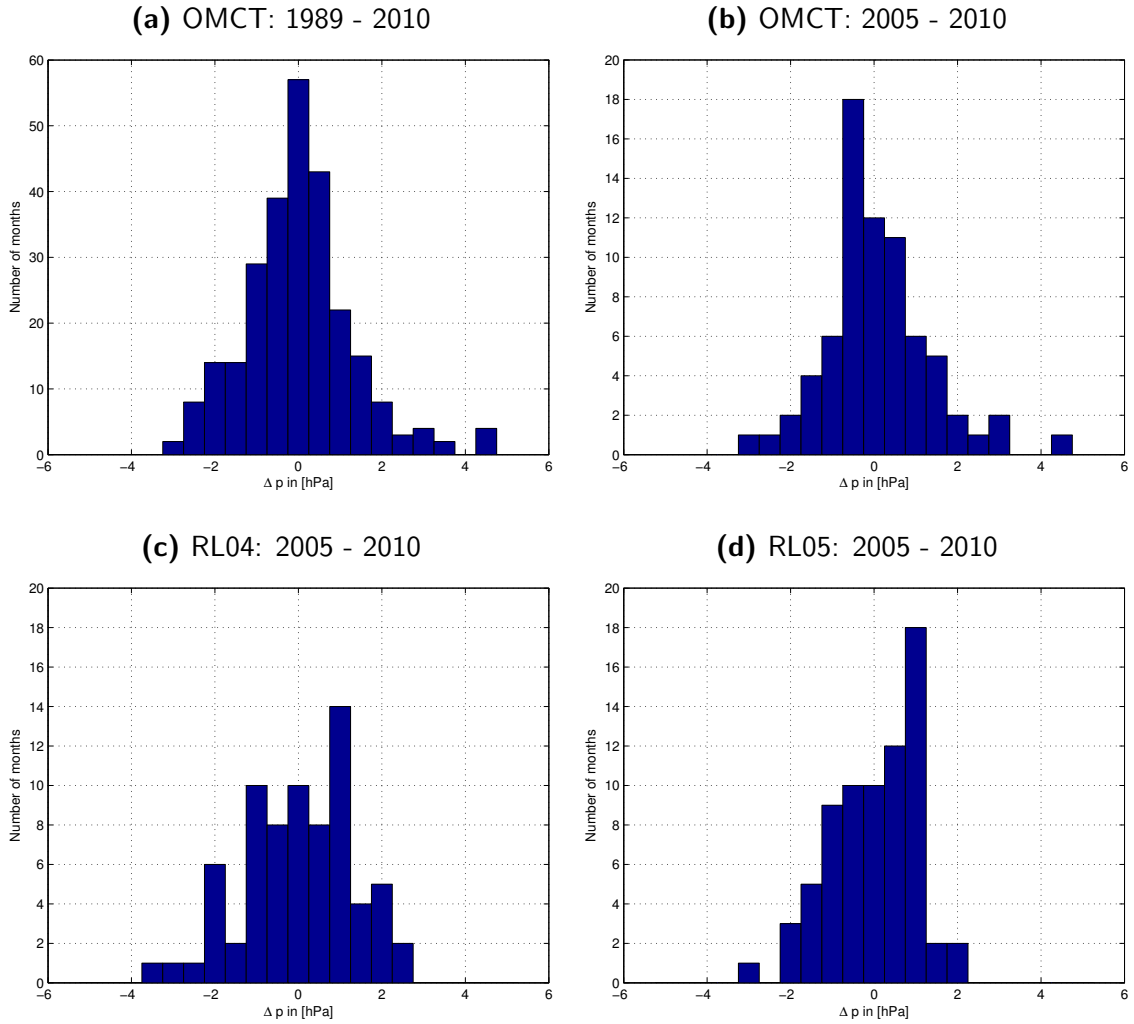

Figure 6.10: Histograms of the residuals related to Figure 6.8 and 6.9: (a) OMCT 22y; (b) OMCT 7y; (c) GRACE RL04; (d) GRACE RL05.

pled for a detailed analysis. Nevertheless, it gives an idea of the error. This is especially true for RL04 and RL05. Here the residuals are generally smaller, showing fewer extreme values. However, especially RL05 shows a clear negative skew, including a clear distinguished peak between 0.75 and 1.25 hPa. Only few samples show higher values, while the distribution is tailing to the left. This indicates a systematic disagreement between RL05 and the regression result. The reason for this can be manifold and may result from both, limitations of the RL05 data and limitations in the regression. Also the way we processed the data may be contributing to the shown residuals. For example we deseasonalize the GRACE data using only 6 years, which makes the data sensitive to low frequency modes of climate variability, such as ENSO and the NAM. Other processing approaches such as annual cycle filtering based on a sinusoidal fitting lead to similar results.

6.4 NAM and ENSO contributions to the North Pacific mass variations

This section investigates the actual effect of large scale climate variations, such as the NAM and ENSO on the North Pacific ocean mass variations. For visualizing these effects, we use the composite mean differences (CMD) between maximum and minimum conditions of the related index. Maximum conditions are defined by an index exceeding one standard deviation, while minimum months show an index of less than minus one standard deviation. The composites include 215 NAM_{max} and 217 NAM_{min} and 267 El Niño (max) and 262 La Nina (min) months. The whole modeling time series consists of 145 years or 1740 months.

The modeled atmosphere is compared to CMDs of ERA-Interim data (1989 - 2010) and the ocean component is compared to release 5 GRACE observations (2005 - 2010). The modeling results are robust for a reduction of the analyzed time series from 145 years to an arbitrary 21 years as the length of the ERA-Interim data. However the significance are clearly higher for the longer time series.

6.4.1 NAM

As described above, the NAM is defined as lateral atmospheric mass variations in the northern hemisphere, that are accompanied by lateral variations of the mid-latitudinal jet. Variations in the jet have the potential to propagate to the surface (Li and Wettstein, 2011) and thus may have a direct influence on the ocean mass variation (Sverdrup, 1947). Consequently, the NAM has the direct potential to affect the North Pacific mass variations.

Figure 6.11 shows the North Pacific CMDs (NAM_{max} minus NAM_{min}) for (a) the CESM atmosphere, (b) CESM ocean, (c) ERA-Interim atmosphere, and (d) GRACE observations of the ocean. The vector fields show the CMDs of the surface winds, while the color code denotes mass variations in hPa. Please note that the color scale differs between atmosphere and ocean.

Comparing the atmospheric CMDs shows a general agreement, including negative surface pressure anomalies in the polar region and positive ones in the North Pacific. CESM models stronger positive and weaker negative anomalies compared to the ERA-Interim data.The positive pressure anomaly in the CESM domain is rather circular, centered south of the Aleutian Islands. In contrast we find the positive ERA-Interim pressure system featuring a clear zonal elongation, peaking from the central to the eastern North Pacific. The anticyclonic wind fields frame the high pressure system for both data sets. The amplitude of the westerly surface wind anomalies is in good agreement, though the zonal wind of the ERA-Interim data is strongest in the eastern Pacific. More details on the NAM, especially with respect to the other CESM experiments, is given in section 3.5.

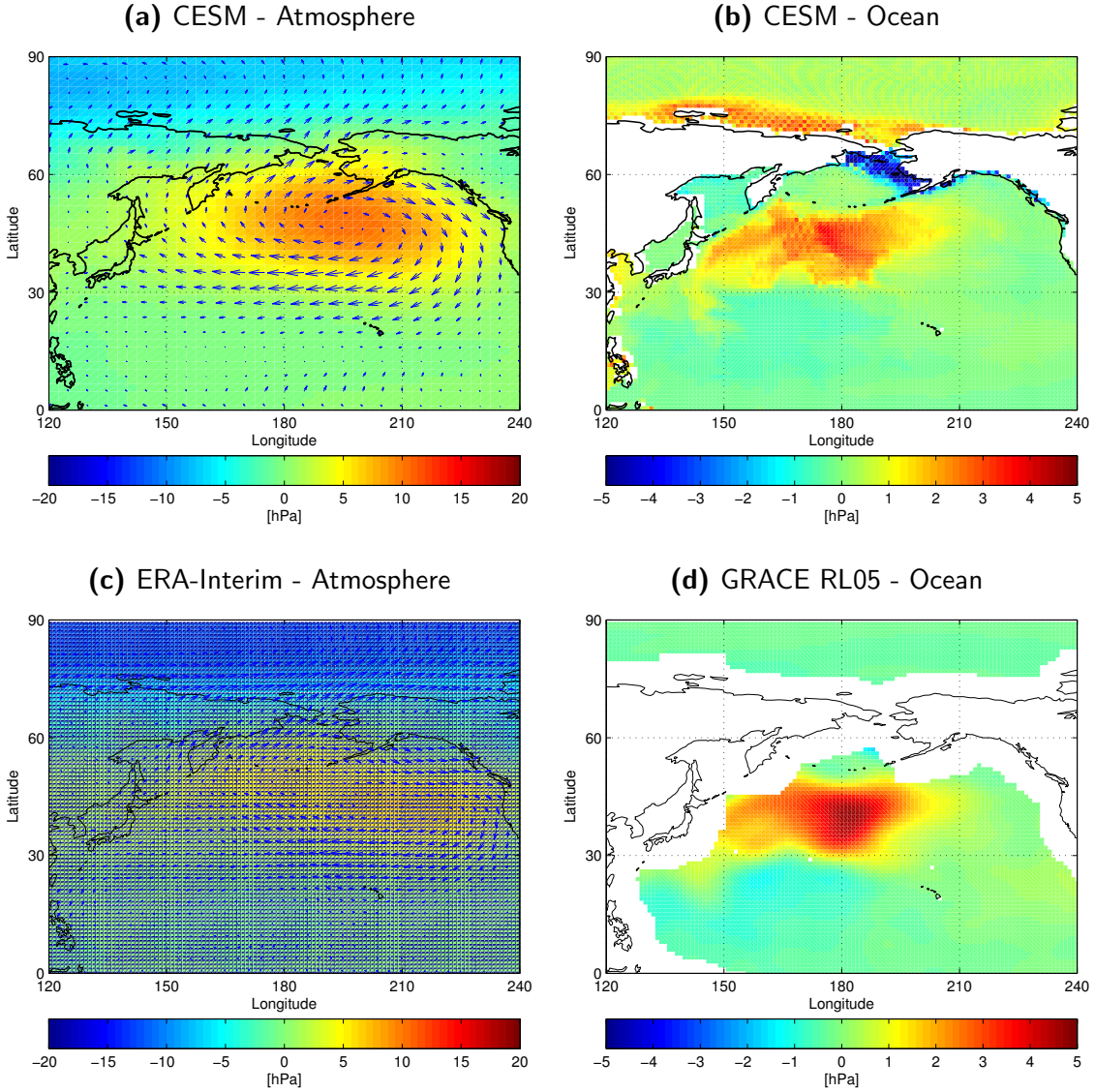

Figure 6.11: Composite Mean Differences of NAM_{MAX} minus NAM_{MIN} for 145 years of NATURAL data. Left: the atmospheric response, color denotes the surface pressure, while the vectors represent surface winds. Right: the oceanic mass anomaly or the ocean response to the shown winds.

We find similarities between the modeled and observed ocean mass anomalies (Figure 6.11 b and d). Both figure agree in shape and amplitude. The major part of the positive signal is located in the western and central Pacific, north of 30°N. Both peak at around 180°E and 40°N. The GRACE observations show a slightly stronger signal of up to 5 hPa, while CESM models values of up to 4 hPa. The negative mass anomalies in the tropical western Pacific are generally weaker than the positive anomalies. Here CESM underestimates the observed values again, however, the shape and location agrees again. Even smaller scale features, such as the positive signals southwest of 30°N and 150°E are in agreement. The values close to the shore line, especially in the polar region, can not be compared due to filtering reasons of the CESM data (cf. section 3.2.1).

Summarizing, Figure 6.11 clearly shows NAM related mass variations in the North Pacific, for both, the modeling domain and observations. Differences are especially present in the atmospheric pressure system. There are two main reasons for the disagreement: (a) malfunctions within model, that prevents realistic modeling; and (b) the induced variations by our experiment setting, that permits natural variations only. Analyzing the NAM related barotropic stream function (BSF) of the CESM ocean, reveals the modeled mass variations as clearly barotrop in nature an thus as wind driven. The BSF is especially effected in the central and western Pacific, around 30°N. This is the region, where the basin scale western boundary currents are strongest. In the eastern part of the ocean basin the gyres are weaker and not as affected by the prevailing wind.

The modeled ocean mass variations are especially present during the northern winter season (December-to-February [DJF]) and continues strong during spring (March-to-May [MAM]). During the summer season (June-to-August [JJA]) we find a weak signal, which starts to build up during fall (September-to-November [SON]).

6.4.2 ENSO

Figure 6.12 shows the modeled and observed CMDs for the atmosphere and the ocean in the same way and scale as for the NAM (cf. Figure 6.11). The atmospheric surface pressure features a low pressure system in the northeast Pacific.

Regarding the ENSO related ocean mass signal, we also find a high agreement between the observations and the model. A clear negative signal is present in the northern central and western Pacific, while a positive signal is present in the subtropics, but not in the tropical Pacific. What differs here is the amplitude; while GRACE observes mass anomalies within the range of +1.3 / -2.5 hPa, CESM output shows anomalies within the range of +1 / -1.5 hPa. Nevertheless, we find great agreements between both data sets.

The effects of ENSO onto the North Pacific mass variations are intensely discussed by Chambers (2011). In our composite analysis (ENSO+ minus ENSO-) we find a typical Aleutian Low response of up to minus 5 hPa (Figure 6.12). This means that during an average El Niño event the Aleutian Low is about 5 hPa below an average La Nina event. This fits well to the findings of Niebauer (1988) who states that the Aleutian Low is about 2 hPa below average during El Niño (winter) and about 3 hPa above average during La Nina.

The net ENSO effect on the atmospheric surface winds around 30°N are westerly winds (Figure 6.12) or a weakening of the climatological wind field. Associated to this change in the wind regime are changes in barotropic stream function, which causes opposing mass anomalies compared to the NAM related signal. This includes negative ocean mass anomalies in the central North Pacific, with an observed amplitude of up to 2 hPa. CESM produces

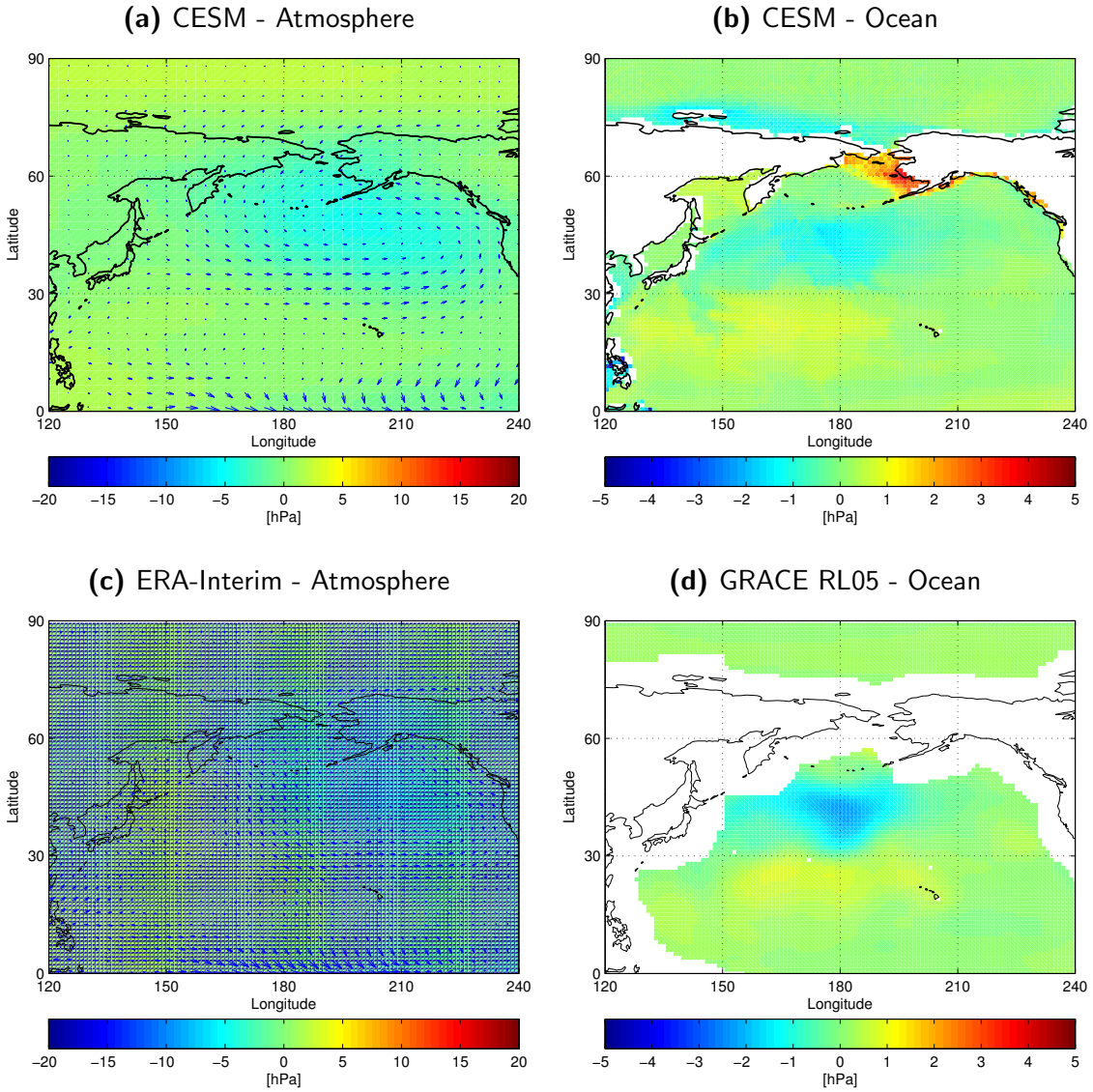

Figure 6.12: Same as Figure 6.11, but now for ENSO.

a similar feature, but only half the amplitude. Both data sets show slightly positive mass anomalies south of 30°N.

As for the NAM composite, the ENSO signal is especially strong during boreal winter, when the Aleutian Low is especially strong and active. Then the pressure anomalies exceed minus 10 hPa and the associated oceanic mass anomalies reach -2.5 and 1.5 hPa, respectively. Negative ocean mass anomalies are also present during MAM, while the positive features occur also during JJA.

6.5 Summary

This chapter discussed oceanic mass variations and their connection to the prevailing wind and pressure system in the North Pacific. First, we defined a time series representing the modeled ocean mass variations by averaging over the region of the most variable ocean bottom pressure (cf. Figure 6.1). In a regression analysis this time series was reconstructed using the PCs of the first four EOF patterns of the North Pacific MSLP together with a constant, a trend and an annual cycle as well as the QBO and the solar cycle. The regression identified three significant pressure and with it three significant wind patterns (cf. Figure 6.2 and 6.3), allowing to reconstruct the modeled ocean mass signal solely based on prevailing winds (cf. Figure 6.4).

In order to verify these modeling results with geodetic observations, a time series of the observed ocean mass anomalies based on GRACE observations was reconstructed (cf. Figure 6.7). The same was done for modeled ocean mass variations, computed with the OMCT, which was forced with ERA-Interim data. The wind time series were reconstructed by projecting the significant CESM MSLP pattern on the ERA-Interim reanalysis MSLP. The estimated ERA-Interim and CESM based North Pacific mass anomalies are in good agreement with the independent GRACE RL05 observations of the ocean mass variation, featuring a correlation of 0.83 (cf. Figure 6.9). Further analyses related to ENSO and NAM showed that it is not a specific climate mode or index that explains the ocean mass variations, but solely the surface winds. As long as a certain climate mode, regardless if NAM, ENSO or any other, alters the wind field, it will leave a footprint in the ocean mass signal.

For the North Pacific, this strengthens the proposed physical relation between the ocean mass and the prevailing wind stress (Sverdrup, 1947), meaning that the wind contains information about the ocean mass. This implies that over the ocean GRACE observations could be further refined by including e.g. reanalysis winds into the GRACE processing. But also the reverse is true. GRACE observations contain information about the prevailing winds and thus can be assimilated into, for example, reanalysis data. As indicated in the introduction, until recently, this result was unexpected (Ilk et al., 2005). However, the here presented evidence supports the physical relation between surface winds and ocean mass in the North Pacific.

Chapter 7

Summary

This work analyses mass and motion variations and their interactions within the atmosphere, ocean and on land, using a climate system model and geodetic observations including the Earth rotation and the gravity field. This work offers two main contributions. First, the Earth rotational excitations of the coupled climate model are compared to geodetic observations of the Earth rotation, including a detailed analysis of the influences of the modeled subcomponents and the identification of the most influential regions. This analysis show the potential and weaknesses of the Earth rotational excitations for the validation of a coupled climate model. The second main contribution is located in the North Pacific, where strong coupling effects between the atmosphere and ocean are found. Here, surface winds can be used to estimate ocean mass variations within the modeling and observational domain. This relation implies that in the North Pacific, wind observations can be used to refine gravity observations and additionally that gravity observations can be used to constrain the surface wind field.

As a pre-study, Chapter 4 analyses the need for coupled climate models by comparing the influence of different atmospheric modes of natural climate variability (i.e. solar cycle and QBO) and then investigates their influence on a stand-alone ocean model (cf. OMCT, section 3.2.2). The major outcome is that a realistic QBO nudging improves the stratosphere-troposphere coupling particularly on the southern hemisphere, allowing the stratospheric solar cycle response to propagate through the troposphere down to the surface (cf. Figure 4.2), where it significantly influences the ocean (cf. Figure 4.5). This indicates the importance of the middle atmosphere including a realistically nudged QBO for the whole atmosphere and the ocean. This pre-study showed that modes of natural climate variations (solar cycle) can propagate from one subsystem to the other. This indicates the potential benefit of global coupled climate models in the context of studying modes of natural climate variations.

Such a consistently coupled climate model including subcomponents that represent the atmosphere, ocean, land and cryosphere, is NCAR's Community Earth System Model (CESM). In the context of this work, CESM was successfully implemented at the Deutsches Klimarechen-

zentrum (DKRZ) in Hamburg. The implementation was tested by comparing two decades of a reference experiment to the associated reference data, provided by NCAR. Finally, four experiments (cf. section 3.3) were designed and carried out, including (1) NATURAL, representing solely natural variations, omitting anthropogenic influences; (2) NOQBO, the same experiment, just without QBO nudging; (3) ATMOS, the same as NATURAL using a climatological data ocean; and (4) RCP, the same as NATURAL but now including anthropogenic forcings such as greenhouse gases and ozone depleting substances.

In the introduction, the question whether and to what extent the Earth rotation can be used to validate the integrated behavior of a coupled climate system model is raised based on the scientific goals formulated by Schuh et al. (2003).

Chapter 5 analyses the modeled Earth rotational excitations on annual and interannual timescales and compares these results to very precise global observations (IERS, cf. section 2.3.1) and operational excitation functions for the atmosphere, ocean and land (Dobslaw et al. (2010), cf. section 2.3.2). The analysis of all three data sets renders the total annual cycle of the operational data in agreement with the observed IERS data for all three rotational axes (cf. Figure 5.1). The operational atmospheric excitation is computed based on ERA-Interim data, while the ocean and land components are based on stand-alone models (OMCT and LSDM, cf. section 2.3.2), which are forced with ERA-Interim data.

In contrast, the CESM experiments are fully independent of any observational data. The modeled annual cycle of the polar motion exaggerates the observations (cf. Figure 5.1a and b), which can be related to an overestimation of the atmospheric mass signal (cf. Figures 5.2 and 5.4). Analyzing the excitation maps (cf. Figures 5.3 and 5.5) reveals too strong modeled atmospheric pressure variations in the North Pacific, which particularly alters χ_1. The polar motion excitation of the ocean component is in agreement with the operational data (cf. Figure 5.2 and 5.4). However, the second oceanic mass component features a slight annual cycle, which can be attributed to ocean bottom pressure variations in the southern Indian ocean (cf. Figure 5.4b). The annual cycle of the polar motion excitation of the hydrosphere shows similar amplitudes but also deviations in the annual cycle (cf. Figure 5.2,5.4 and 5.5). These deviations cannot be attributed to a specific region but indicate variations of the continental precipitation as well as the discharge behavior of the land model component.

Regarding the modeled χ_3 excitation, we find the CESM model underestimating that annual cycle (cf. Figure 5.1). This is mainly related to the atmospheric motion component (cf. Figure 5.6), which is dominated by the subtropical jets (cf. Figure 5.7). The annual cycle of χ_3 is mainly related to the asymmetric subtropical jet strength between the northern and southern hemisphere (Rosen and Salstein, 1983; Anderson and Rosen, 1983). Thus, the deviations of the modeled χ_3 component indicate an inaccurately modeled temporal behavior of the subtropical jets.

Further, chapter 5 analyses interannual variations of the excitation functions, revealing significant deviations among the CESM experiments, especially regarding the atmospheric motion component. Experiments NATURAL and RCP show interannual χ_3 variations mainly related to the subtropical jets and the QBO nudging zone, indicating no anthropogenic influence. Deviating from these results, we find experiment NOQBO with no interannual zonal wind variations in the QBO nudging zone. In contrast to all three simulations, experiment ATMOS, which was forced with a climatological data ocean, features virtually no interannual variations of the subtropical jets (cf. Figure 5.13). Solely the QBO nudging introduces interannually zonal wind variations. This clearly indicates the importance of a realistic ocean component for the realistic modeling of interannual atmospheric variations. This answers the introductory question regarding the separation of natural from anthropogenic variations in the context of chapter 5 clearly: There is no evidence of a significant anthropogenic impact influencing the Earth rotation. However, natural variations, related for example to the QBO or the ocean component, significantly alter especially interannual excitations (cf. Figure 5.13).

Further, chapter 5 shows the modeled NAM and ENSO related excitations for the atmosphere, ocean and land components. Particularly, the NAM related excitations indicate mass and motion related interaction for the atmosphere and ocean component in the North Pacific (cf. Figure 5.17). This answers the introductory question regarding the identification of regions of particularly strong coupling with a clear yes.

The above summarized Earth rotational excitation analysis of chapter 5 gives no clear answer to the introductory question whether the integrated behavior of a coupled climate model can be evaluated upon Earth rotation data. While a full evaluation is certainly not possible, we find the excitation functions together with the excitation maps capable of identifying problematic components and in some cases even problematic regions.

Based on the findings of chapter 5, the North Pacific could be identified as a region of especially high dynamical coupling between the atmosphere and the ocean within the CESM model. Sverdrup's Theory (cf. section 2.2) relates the oceanic mass anomalies to the prevailing winds. In order to test this relation, the principal components of the significant EOFs (cf. section 2.4.3) of the modeled North Pacific pressure system were used in a multiple linear regression model in order to estimate the oceanic mass variations. Within chapter 6 three significant pressure and with it three significant wind patterns were identified, all featuring zonal surface wind anomalies in the North Pacific around 30°N (cf. Figure 6.2 and 6.3). Here, wind anomalies towards the west have a positive effect on the ocean mass anomaly, while wind anomalies towards the east yield negative mass variations. The wind based reconstruction of the oceanic mass signal shows a correlation of r=0.89 to the actual modeled ocean mass signal.

In order to verify these findings, the significant CESM EOF patterns were projected on ERA-Interim pressure fields. Using the same multiple linear regression, including the CESM based regression factors, the real ocean mass signal was reconstructed. Comparing the wind based regression result to the independent GRACE based ocean mass variations, shows a correlation of r=0.83 for the latest GRACE release RL05. Further investigations of the North Pacific mass anomalies with respect to NAM and ENSO show that it is not a specific climate mode or index that explains the ocean mass variations, but solely the surface winds. As long as a certain climate mode, regardless if NAM, ENSO or any other, alters the surface winds in the North Pacific around 30°N, it will leave a footprint in the ocean mass signal.

Summarizing, chapter 6 supports the proposed physical relation between ocean mass variations and the prevailing wind stress (Sverdrup, 1947) implying two things: First, reanalysis wind and pressure patterns contain information about the ocean mass variations and thus can be used to further refine the gravity field observations. Secondly, gravity field observations (e.g. by GRACE) equally contain information about the prevailing wind and pressure system, meaning that gravity observations could be assimilated into atmospheric models. Until recently this result was unexpected (Ilk et al., 2005), however, it clearly indicates the beneficial potential that can be gained by an alliance between the climate model and the geodetic community.

7.1 Outlook

In order to support the findings regarding the atmosphere ocean coupling in the North Pacific, the herein presented analysis will be extended to ten years as soon as the GRACE RL05 data becomes available. A manuscript compiling the extended findings of chapter 6 will be submitted for publication.

The herein discussed coupling effects between the atmosphere and ocean are also modeled and observed on the southern hemisphere, particularly in the southern Indian and southern Pacific ocean. Thus, repeating the analyses of chapter 6 would further encourage an effort to assimilate gravity field observations (e.g. from GRACE) into atmospheric models, constraining especially the atmospheric surface wind and pressure components. Additionally, the assimilation of reanalysis winds could be used to further refine the gravity field observations.

The analysis of the modeled Earth rotational excitation as presented in chapter 5 shows significant deviations of the interannual zonal wind variations, especially regarding the subtropical jets. Further analyses of the herein presented model experiments will focus on the physical explanation of these deviations.

The continuing development of the coupled Earth system models will lead to an inclusion of components representing the Earth's interior, i.e. the crust, mantle and core. This will allow

a more comprehensive investigation of physical phenomena, such as post-glacial rebound or self-attraction and loading, particularly in the context of global climate studies. A model that includes all these effects would significantly improve the understanding of geodetic observations, for example by closing the gap between the short term hydrological and the long term Earth's interior related Earth rotational excitations.

Bibliography

Alexander, M. A., I. Bladé, M. Newman, J. R. Lanzante, N.-C. Lau, and J. D. Scott, 2002: The Atmospheric Bridge: The Influence of ENSO Teleconnections on Air-Sea Interaction over the Global Oceans. *Journal of Climate*, **15 (16)**, 2205–2231, doi:10.1175/1520-0442(2002)015⟨2205:TABTIO⟩2.0.CO;2.

Allen, R. J. and C. S. Zender, 2011: Forcing of the Arctic Oscillation by Eurasian Snow Cover. *Journal of Climate*, **24 (24)**, 6528–6539, doi:10.1175/2011JCLI4157.1.

Anderson, J. R. and R. D. Rosen, 1983: The Latitude-Height Structure of 40-50 Day Variations in Atmospheric Angular Momentum. *Journal of the Atmospheric Sciences*, **40 (6)**, 1584–1591, doi:10.1175/1520-0469(1983)040⟨1584:TLHSOD⟩2.0.CO;2.

Bailey, D., M. Holland, E. Hunke, B. Lipscomb, B. Briegleb, C. Bitz, and J. Schramm, 2012: Community Ice CodE (CICE) User ' s Guide Released with CESM1 . 0. Tech. rep., National Center for Atmospheric Research, 23 pp., Boulder, Colorado, USA.

Baldwin, M. P. and D. W. J. Thompson, 2009: A critical comparison of stratosphere-troposphere coupling indices. *Quarterly Journal of the Royal Meteorological Society*, **135 (644)**, 1661–1672.

Baldwin, M. P., et al., 2001: The quasi-biennial oscillation. *Reviews of Geophysics*, **39 (2)**, 179–229, doi:10.1029/1999RG000073.

Barnes, R. T. H., R. Hide, A. A. White, and C. A. Wilson, 1983: Atmospheric Angular Momentum Fluctuations, Length-of-Day Changes and Polar Motion. *Proceedings of the Royal Society A: Mathematical, Physical and Engineering Sciences*, **387 (1792)**, 31–73, doi:10.1098/rspa.1983.0050.

Bergmann, I. and H. Dobslaw, 2012: Short-term transport variability of the Antarctic Circumpolar Current from satellite gravity observations. *Journal of Geophysical Research*, **117 (C5)**, C05 044, doi:10.1029/2012JC007872.

Bingham, R. J. and C. W. Hughes, 2006: Observing seasonal bottom pressure variability in the North Pacific with GRACE. *Geophysical Research Letters*, **33 (8)**, L08 607, doi: 10.1029/2005GL025489.

Bizouard, C. and D. Gambis, 2008: The combined solution C04 for Earth Orientation Parameters consistent with International Terrestrial Reference Frame 2008. Tech. rep., Observatoire de Paris, SYRTE, 1–8 pp.

Bizouard, C. and L. Seoane, 2009: Atmospheric and oceanic forcing of the rapid polar motion. *Journal of Geodesy*, **84 (1)**, 19–30, doi:10.1007/s00190-009-0341-2.

Bjornsson, H. and S. A. Venegas, 1997: A manual for EOF and SVD analyses of climate data. Tech. rep., McGill University, 52 pp., Montréal.

Boening, C., T. Lee, and V. Zlotnicki, 2011: A record-high ocean bottom pressure in the South Pacific observed by GRACE. *Geophysical Research Letters*, **38 (4)**, doi:10.1029/2010GL046013.

Brzezinski, A., H. Dobslaw, R. Dill, and M. Thomas, 2012: Geophysical Excitation of the Chandler Wobble Revisited. *Geodesy for Planet Earth*, S. Kenyon, M. C. Pacino, and U. Marti, Eds., Springer Berlin Heidelberg, International Association of Geodesy Symposia, Vol. 136, 499–505, doi:10.1007/978-3-642-20338-1_60.

Brzezinski, A., J. Nastula, and B. Kolaczek, 2009: Seasonal excitation of polar motion estimated from recent geophysical models and observations. *Journal of Geodynamics*, **48 (3-5)**, 235–240, doi:10.1016/j.jog.2009.09.021.

Camp, C. D. and K. K. Tung, 2007: Surface warming by the solar cycle as revealed by the composite mean difference projection. *Geophysical Research Letters*, **34 (14)**, doi: 10.1029/2007GL030207.

Carleton, A. M., 2003: Atmospheric teleconnections involving the Southern Ocean. *Journal of Geophysical Research: Oceans*, **108 (C4)**, doi:10.1029/2000JC000379.

Chambers, D. P., 2006: Evaluation of new GRACE time-variable gravity data over the ocean. *Geophysical Research Letters*, **33 (17)**, L17 603, doi:10.1029/2006GL027296.

Chambers, D. P., 2011: *Ocean Sci.*, **7 (5)**, 685–692, doi:10.5194/os-7-685-2011.

Chambers, D. P. and J. A. Bonin, 2012: Evaluation of Release-05 GRACE time-variable gravity coefficients over the ocean. *Ocean Sci.*, **8 (5)**, 859–868, doi:10.5194/os-8-859-2012.

Chambers, D. P. and J. K. Willis, 2010: A Global Evaluation of Ocean Bottom Pressure from GRACE, OMCT, and Steric-Corrected Altimetry. *Journal of Atmospheric and Oceanic Technology*, **27 (8)**, 1395–1402, doi:10.1175/2010JTECHO738.1.

Chang, P., et al., 2006: Climate Fluctuations of Tropical Coupled Systems-The Role of Ocean Dynamics. *Journal of Climate*, **19 (20)**, 5122–5174, doi:10.1175/JCLI3903.1.

Chao, B. F., 1989: Length-of-Day Variations Caused by El Niño-Southern Oscillation and Quasi-Biennial Oscillation. *Science*, **243 (4893)**, 923–925.

Chen, B., S. Smith, and D. Bromwich, 1996: Evolution of the tropospheric split jet over the South Pacific Ocean during the 1986-89 ENSO cycle. *Monthly weather review*, **124 (8)**, 1711–1731.

Chen, W. and W. Shen, 2010: New estimates of the inertia tensor and rotation of the triaxial nonrigid Earth. *Journal of Geophysical Research*, **115 (B12)**, B12 419, doi:10.1029/2009JB007094.

Cohen, J. and D. Entekhabi, 1999: Eurasian snow cover variability and northern hemisphere climate predictability. *Geophysical Research Letters*, **26 (3)**, 345–348, doi:10.1029/1998GL900321.

Collins, W. D., et al., 2006: The Community Climate System Model Version 3 (CCSM3). *Journal of Climate*, **19 (11)**, 2122–2143, doi:10.1175/JCLI3761.1.

Dahle, C., F. Flechtner, C. Gruber, D. König, R. König, G. Michalak, and K.-H. Neumayer, 2012: GFZ GRACE Level-2 Processing Standards Document for Level-2 Product Release 0005. Tech. rep., Potsdam. doi:10.2312/GFZ.b103-12020.

Dahlen, F. A., 1976: The Passive Influence of the Oceans upon the Rotation of the Earth. *Geophysical Journal of the Royal Astronomical Society*, **46 (2)**, 363–406, doi:10.1111/j.1365-246X.1976.tb04163.x.

Danabasoglu, G., S. C. Bates, B. P. Briegleb, S. R. Jayne, M. Jochum, W. G. Large, S. Peacock, and S. G. Yeager, 2011: The CCSM4 Ocean Component. *Journal of Climate*, **25 (5)**, 1361–1389, doi:10.1175/JCLI-D-11-00091.1.

Deser, C., R. A. Tomas, and S. Peng, 2007: The Transient Atmospheric Circulation Response to North Atlantic SST and Sea Ice Anomalies. *Journal of Climate*, **20 (18)**, 4751–4767, doi:10.1175/JCLI4278.1.

Deser, C., et al., 2011: ENSO and Pacific Decadal Variability in the Community Climate System Model Version 4. *Journal of Climate*, **25 (8)**, 2622–2651, doi:10.1175/JCLI-D-11-00301.1.

Dickey, J. O., S. L. Marcus, and O. de Viron, 2010: Closure in the Earth's angular momentum budget observed from subseasonal periods down to four days: No core effects needed. *Geophysical Research Letters*, **37 (3)**, L03 307, doi:10.1029/2009GL041118.

Dill, R. and H. Dobslaw, 2010: Short-term polar motion forecasts from earth system modeling data. *Journal of Geodesy*, **84 (9)**, 529–536, doi:10.1007/s00190-010-0391-5.

Dobslaw, H., R. Dill, A. Grötzsch, A. Brzezinski, and M. Thomas, 2010: Seasonal polar motion excitation from numerical models of atmosphere, ocean, and continental hydrosphere. *Journal of Geophysical Research*, **115 (B10)**, B10 406, doi:10.1029/2009JB007127.

Drijfhout, S., C. Heinze, M. Latif, and E. Maier-Reimer, 1996: Mean Circulation and Internal Variability in an Ocean Primitive Equation Model. *Journal of Physical Oceanography*, **26 (4)**, 559–580, doi:10.1175/1520-0485(1996)026⟨0559:MCAIVI⟩2.0.CO;2.

Edwards, P. N., 2011: History of climate modeling. *Wiley Interdisciplinary Reviews: Climate Change*, **2 (1)**, 128–139, doi:10.1002/wcc.95.

Efron, B., 1979: Bootstrap methods: Another look at the jackknife. *Annals of Statistics*, **7 (1)**, 1–26, doi:10.1214/aos/1176344552.

Efron, B. and R. Tibshirani, 1993: *An Introduction to the Bootstrap*. Chapman & Hall/CRC, New York, 436 pp.

Eubanks, T. M., 1993: Variations in the orientation of the Earth. *Contributions of Space Geodesy to Geodynamics: Earth Dynamics*, AGU, Washington, DC, Geodynics Series, Vol. 24, 1–54, doi:10.1029/GD024p0001.

Feynman, R. P., 1982: Simulating physics with computers. *International Journal of Theoretical Physics*, **21 (6-7)**, 467–488, doi:10.1007/BF02650179.

Flechtner, F., 2007: GFZ Level-2 Processing Standards Document. Tech. rep., GFZ Potsdam, 19 pp., Potsdam.

Garcia, R. R., D. R. Marsh, D. E. Kinnison, B. A. Boville, and F. Sassi, 2007: Simulation of secular trends in the middle atmosphere, 1950-2003. *Journal of Geophysical Research*, **112 (D9)**, D09 301, doi:10.1029/2006JD007485.

Gent, P. R., et al., 2011: The Community Climate System Model Version 4. *Journal of Climate*, **24 (19)**, 4973–4991, doi:10.1175/2011JCLI4083.1.

Gerber, E. P., et al., 2010: Stratosphere-troposphere coupling and annular mode variability in chemistry-climate models. *Journal of Geophysical Research*, **115**, D00M06, doi:10.1029/2009JD013770.

Gray, L. J., et al., 2010: SOLAR INFLUENCES ON CLIMATE. *Review of Geophysics*, **48 (4)**, RG4001, doi:10.1029/2009RG000282.

Gross, R., 2007: Earth Rotation Variations - long period. *Treatise on Geophysics*, T.A. Herring, Ed., Amsterdam, Vol. 3, 3d ed., chap. Geodesy, 239 – 294.

Gross, R. S., I. Fukumori, and D. Menemenlis, 2003: Atmospheric and oceanic excitation of the Earth's wobbles during 1980-2000. *Journal of Geophysical Research*, **108 (B8)**, 2370, doi:10.1029/2002JB002143.

Groten, E., 2004: Fundamental Parameters and Current (2004) Best Estimates of the Parameters of Common Relevance to Astronomy, Geodesy, and Geodynamics. *Journal of Geodesy 77, 10-11, The Geodesist's Handbook, p. 724 - 731, April 2004.*

Hare, S., 1996: Low frequency climate variability and salmon production. Ph.d. dissertation, University of Washington, Seattle.

Harrison, D. E. and N. K. Larkin, 1998: El Nino-Southern Oscillation sea surface temperature and wind anomalies, 1946-1993. *Review of Geophysics*, **36 (3)**, 353–399, doi:10.1029/98RG00715.

Holton, J. R. and H.-C. Tan, 1980: The Influence of the Equatorial Quasi-Biennial Oscillation on the Global Circulation at 50 mb. *Journal of the Atmospheric Sciences*, **37 (10)**, 2200–2208, doi:10.1175/1520-0469(1980)037⟨2200:TIOTEQ⟩2.0.CO;2.

Holton, J. R. and H.-C. Tan, 1982: The Quasi-Biennial Northern Hemisphere Oscillation in the Lower Stratosphere. *Journal of the Meteorological Society of Japan*, 140–148.

Huang, B. and V. M. Mehta, 2005: Response of the Pacific and Atlantic oceans to interannual variations in net atmospheric freshwater. *Journal of Geophysical Research*, **110 (C8)**, C08 008, doi:10.1029/2004JC002830.

Hunke, E. C. and W. H. Lipscomb, 2010: CICE : the Los Alamos Sea Ice Model Documentation and Software User ' s Manual LA-CC-06-012. Tech. rep., Los Alamos National Laboratory, Los Alamos NM.

Ilk, K., et al., 2005: *Mass Transport and Mass Distribution in the Earth System - Contribution of the New Generation of Satellite Gravity and Altimetry Missions to Geosciences*. 2d ed., München, Potsdam, 160 pp.

Jaiser, R., K. Dethloff, D. Handorf, a. Rinke, and J. Cohen, 2012: Impact of sea ice cover changes on the Northern Hemisphere atmospheric winter circulation. *Tellus A*, **64**, 1–11, doi:10.3402/tellusa.v64i0.11595.

Kerr, R. A., 1999: A New Force in High-Latitude Climate. *Science*, **284 (5412)**, 241–242, doi:10.1126/science.284.5412.241.

Kinnison, D. E., et al., 2007: Sensitivity of chemical tracers to meteorological parameters in the MOZART-3 chemical transport model. *Journal of Geophysical Research*, **112 (D20)**, D20 302, doi:10.1029/2006JD007879.

Kodera, K. and Y. Kuroda, 2002: Dynamical response to the solar cycle. *Journal of Geophysical Research*, **107 (D24)**, 4749, doi:10.1029/2002JD002224.

Kuehne, J. and C. R. Wilson, 1991: Terrestrial water storage and polar motion. *Journal of Geophysical Research*, **96 (B3)**, 4337, doi:10.1029/90JB02573.

Kuroda, Y. and K. Kodera, 2005: Solar cycle modulation of the Southern Annular Mode. *Geophysical Research Letters*, **32 (13)**, L13 802, doi:10.1029/2005GL022516.

Kusche, J., 2007: Approximate decorrelation and non-isotropic smoothing of time-variable GRACE-type gravity field models. *Journal of Geodesy*, **81 (11)**, 733–749, doi:10.1007/s00190-007-0143-3.

Kusche, J., V. Klemann, and W. Bosch, 2012: Mass distribution and mass transport in the Earth system. *Journal of Geodynamics*, **59-60 (0)**, 1–8, doi:http://dx.doi.org/10.1016/j.jog.2012.03.003.

Labitzke, K., 1987: Sunspots, the QBO, and the stratospheric temperature in the north polar region. *Geophysical Research Letters*, **14 (5)**, 535–537, doi:10.1029/GL014i005p00535.

Labitzke, K. and H. Van Loon, 1988: Associations between the 11-year solar cycle, the QBO and the atmosphere. Part I: the troposphere and stratosphere in the northern hemisphere in winter. *Journal of Atmospheric and Terrestrial Physics*, **50 (3)**, 197–206.

Labitzke, K., et al., 2002: The global signal of the 11-year solar cycle in the stratosphere: observations and models. *Journal of Atmospheric and Solar-Terrestrial Physics*, **64 (2)**, 203–210, doi:http://dx.doi.org/10.1016/S1364-6826(01)00084-0.

Lambeck, K., 1980: *The Earth's Variable Rotation: Geophysical Causes and Consequences.* Cambridge Monographs on Mechanics And Applied Mathematics, Cambridge University Press, New York.

Lawrence, D., et al., 2011: Parameterization Improvements and Functional and Structural Advances in Version 4 of the Community Land Model. *Journal of Advances in Modeling Earth Systems; Vol. 3, 2011.*

Li, C. and J. J. Wettstein, 2011: Thermally Driven and Eddy-Driven Jet Variability in Reanalysis*. *Journal of Climate*, **25 (5)**, 1587–1596, doi:10.1175/JCLI-D-11-00145.1.

Lombard, A., et al., 2007: Estimation of steric sea level variations from combined GRACE and Jason-1 data. *Earth and Planetary Science Letters*, **254 (1-2)**, 194–202, doi:http://dx.doi.org/10.1016/j.epsl.2006.11.035.

Mantua, N. and S. Hare, 2002: The Pacific Decadal Oscillation. *Journal of Oceanography*, **58 (1)**, 35–44, doi:10.1023/A:1015820616384.

Marsh, D. R. and R. R. Garcia, 2007: Attribution of decadal variability in lower-stratospheric tropical ozone. *Geophysical Research Letters*, **34 (21)**, L21 807, doi:10.1029/2007GL030935.

Matthes, K., R. R. Garcia, Y. Kuroda, K. Kodera, D. R. Marsh, and K. Labitzke, 2012: Role of the QBO in Modulating the Influence of the 11-Year Solar Cycle on the Atmosphere Using Time-Varying Forcings. *submitted to Journal of Geophysical Research*, 1–36.

Matthes, K., D. R. Marsh, R. R. Garcia, D. E. Kinnison, F. Sassi, and S. Walters, 2010: Role of the QBO in modulating the influence of the 11 year solar cycle on the atmosphere using constant forcings. *Journal of Geophysical Research*, **115 (D18)**, D18 110, doi:10.1029/2009JD013020.

Meehl, G. A., J. M. Arblaster, J. M. Caron, H. Annamalai, M. Jochum, A. Chakraborty, and R. Murtugudde, 2011a: Monsoon Regimes and Processes in CCSM4. Part I: The Asian-Australian Monsoon. *Journal of Climate*, **25 (8)**, 2583–2608, doi:10.1175/JCLI-D-11-00184.1.

Meehl, G. A., J. M. Arblaster, K. Matthes, F. Sassi, and H. van Loon, 2009: Amplifying the Pacific Climate System Response to a Small 11-Year Solar Cycle Forcing. *Science (New York, N.Y.)*, **325 (5944)**, 1114–8, doi:10.1126/science.1172872.

Meehl, G. A., et al., 2011b: Climate System Response to External Forcings and Climate Change Projections in CCSM4. *Journal of Climate*, **25 (11)**, 3661–3683, doi:10.1175/JCLI-D-11-00240.1.

Meehl, G. A., et al., 2012: Climate System Response to External Forcings and Climate Change Projections in CCSM4. *Journal of Climate*, **25 (11)**, 3661–3683, doi: 10.1175/JCLI-D-11-00240.1.

Moritz, H. and I. I. Mueller, 1988: *Earth rotation: theory and observation*. Ungar, New York.

Munk, W. H. and G. J. F. MacDonald, 1960: *The Rotation of the Earth. A geophysical discussion.* Cambridge University Press, Cambridge, New York., 323 pp.

Neale, R. B., C.-c. Chen, P. H. Lauritzen, D. L. Williamson, A. J. Conley, A. K. Smith, M. Mills, and H. Morrison, 2010: Description of the NCAR Community Atmosphere Model (CAM 5 . 0), Tech. Rep. NCAR/TN-486+STR. Tech. rep., National Center for Atmospheric Research, 283 pp., Boulder, Colorado, USA.

Neef, L. and K. Matthes, 2012: Comparison of Earth rotation excitation in data-constrained and unconstrained atmosphere models. *Journal of Geophysical Research*, **117 (D2)**, D02 107, doi:10.1029/2011JD016555.

Neelin, J. D., D. S. Battisti, A. C. Hirst, F.-F. Jin, Y. Wakata, T. Yamagata, and S. E. Zebiak, 1998: ENSO theory. *Journal of Geophysical Research*, **103 (C7)**, 14 261–14 290, doi:10.1029/97JC03424.

Okumura, Y. M. and C. Deser, 2010: Asymmetry in the Duration of El Niño and La Niña. *Journal of Climate*, **23 (21)**, 5826–5843, doi:10.1175/2010JCLI3592.1.

Petit, G. and B. Luzum, 2010: IERS Conventions (2010).

Petrick, C., K. Matthes, H. Dobslaw, and M. Thomas, 2012: Impact of the solar cycle and the QBO on the atmosphere and the ocean. *Journal of Geophysical Research*, **117 (D17)**, D17 111, doi:10.1029/2011JD017390.

Ponte, R. M., 1999: A preliminary model study of the large-scale seasonal cycle in bottom pressure over the global ocean. *Journal of Geophysical Research*, **104 (C1)**, 1289–1300, doi:10.1029/1998JC900028.

Ponte, R. M., D. Stammer, and J. Marshall, 1998: Oceanic signals in observed motions of the Earth's pole of rotation. **391 (6666)**, 476–479, doi:10.1038/35126.

Preisendorfer, R. W. and C. D. Mobley, 1988: *Principal Component Analysis in Meteorology and Oceanography*. Elsevier, Amsterdam, 425 pp.

Qiu, B., 2003: Kuroshio Extension Variability and Forcing of the Pacific Decadal Oscillations: Responses and Potential Feedback. *Journal of Physical Oceanography*, **33 (12)**, 2465–2482, doi:10.1175/1520-0485(2003)033⟨2465:KEVAFO⟩2.0.CO;2.

Randall, D., et al., 2007: *Cilmate Models and Their Evaluation. In: Climate Change 2007: The Physical Science Basis. Contribution of Working Group I to the Fourth Assessment Report of the Intergovernmental Panel on Climate Change*. Cambridge University Press, Cambridge, United Kingdom and New York, NY, USA.

Rau, D. and I. Rogozhina, 2013: Modeling surface response of the Greenland Ice Sheet to interglacial climate. *submitted to The Cryosphere*.

Rigor, I. G., J. M. Wallace, and R. L. Colony, 2002: Response of Sea Ice to the Arctic Oscillation. *Journal of Climate*, **15 (18)**, 2648–2663, doi:10.1175/1520-0442(2002)015⟨2648:ROSITT⟩2.0.CO;2.

Rind, D., J. Lean, J. Lerner, P. Lonergan, and A. Leboissitier, 2008: Exploring the stratospheric/tropospheric response to solar forcing. *Journal of Geophysical Research*, **113 (D24)**, 1–25, doi:10.1029/2008JD010114.

Robertson, A. W., C. R. Mechoso, and Y.-J. Kim, 2000: The Influence of Atlantic Sea Surface Temperature Anomalies on the North Atlantic Oscillation*. *Journal of Climate*, **13 (1)**, 122–138, doi:10.1175/1520-0442(2000)013⟨0122:TIOASS⟩2.0.CO;2.

Rosen, R. D. and D. A. Salstein, 1983: Variations in atmospheric angular momentum on global and regional scales and the length of day. *Journal of Geophysical Research: Oceans*, **88 (C9)**, 5451–5470, doi:10.1029/JC088iC09p05451.

Rosen, R. D., D. A. Salstein, T. M. Eubanks, J. O. Dickey, and J. A. Steppe, 1984: An El Niño Signal in Atmospheric Angular Momentum and Earth Rotation. *Science*, **225 (4660)**, 411–414.

Roy, I. and J. D. Haigh, 2010: Solar cycle signals in sea level pressure and sea surface temperature. *Atmospheric Chemistry and Physics Discussions*, **9 (6)**, 25 839–25 852, doi:10.5194/acpd-9-25839-2009.

Salstein, D. A. and R. D. Rosen, 1989: Regional Contributions to the Atmospheric Excitation of Rapid Polar Motions. *Journal of Geophysical Research*, **94 (D7)**, 9971–9978, doi:10.1029/JD094iD07p09971.

Sasgen, I., H. Dobslaw, Z. Martinec, and M. Thomas, 2010: Satellite gravimetry observation of Antarctic snow accumulation related to ENSO. *Earth and Planetary Science Letters*, **299 (3-4)**, 352–358, doi:http://dx.doi.org/10.1016/j.epsl.2010.09.015.

Sasgen, I., V. Klemann, and Z. Martinec, 2012: Towards the inversion of GRACE gravity fields for present-day ice-mass changes and glacial-isostatic adjustment in North America and

Greenland. *Journal of Geodynamics*, **59-60 (0)**, 49–63, doi:http://dx.doi.org/10.1016/j.jog.2012.03.004.

Schuh, H., et al., 2003: *Erdrotation und globale dynamische Prozesse*. Verlag des Bundesamts für Kartographie und Geodäsie, Frankfurt am Main, 122 pp.

Smith, M. L. and F. A. Dahlen, 1981: The period and Q of the Chandler wobble. *Geophysical Journal International*, **64 (1)**, 223–281, doi:10.1111/j.1365-246X.1981.tb02667.x.

Smith, R., et al., 2010: The Parallel Ocean Program (POP) reference manual. Tech. rep., Los Alamos National Laboratory Tech. Rep. LAUR-10-01853,, 140 pp.

Song, Y. T. and V. Zlotnicki, 2008: Subpolar ocean bottom pressure oscillation and its links to the tropical ENSO. *International Journal of Remote Sensing*, **29 (21)**, 6091–6107, doi:10.1080/01431160802175538.

SPARC CCMVal, 2010: SPARC Report on the Evaluation of Chemistry-Climate Models, V. Eyring, T. G. Shepherd, D. W. Waugh (Eds.), SPARC Report No. 5, WCRP-132, WMO/TD-No. 1526.

Stewart, R. H., 2008: *Introduction To Physical Oceanography*. Stewart, Robert H, URL `http://oceanworld.tamu.edu/home/course_book.htm`.

Sverdrup, H. U., 1947: Wind-Driven Currents in a Baroclinic Ocean; with Application to the Equatorial Currents of the Eastern Pacific. *Proceedings of the National Academy of Sciences*, **33 (11)**, 318–326.

Tapley, B. D., S. Bettadpur, J. C. Ries, P. F. Thompson, and M. M. Watkins, 2004a: GRACE Measurements of Mass Variability in the Earth System. *Science*, **305 (5683)**, 503–505, doi:10.1126/science.1099192.

Tapley, B. D., S. Bettadpur, M. Watkins, and C. Reigber, 2004b: The gravity recovery and climate experiment: Mission overview and early results. *Geophysical Research Letters*, **31 (9)**, L09 607, doi:10.1029/2004GL019920.

Taylor, K. E., R. J. Stouffer, and G. A. Meehl, 2009: A Summary of the CMIP5 Experiment Design. 1–33, URL `http://cmip-pcmdi.llnl.gov/cmip5/experiment_design.html`.

Taylor, K. E., R. J. Stouffer, and G. A. Meehl, 2012: An Overview of CMIP5 and the Experiment Design. *Bulletin of the American Meteorological Society*, **93 (4)**, 485–498, doi:10.1175/BAMS-D-11-00094.1.

Thomas, M., J. Sündermann, and E. Maier-Reimer, 2001: Consideration of ocean tides in an OGCM and impacts on subseasonal to decadal polar motion excitation. *Geophysical Research Letters*, **28 (12)**, 2457–2460.

Thompson, D. W. J. and J. M. Wallace, 1998: The Arctic oscillation signature in the wintertime geopotential height and temperature fields. *Geophysical Research Letters*, **25 (9)**, 1297–1300, doi:10.1029/98GL00950.

Thompson, D. W. J. and J. M. Wallace, 2000: Annular Modes in the Extratropical Circulation. Part I: Month-to-Month Variability. *Journal of Climate*, **13 (5)**, 1000–1016, doi:10.1175/1520-0442(2000)013⟨1000:AMITEC⟩2.0.CO;2.

Thompson, D. W. J., J. M. Wallace, and G. C. Hegerl, 2000: Annular Modes in the Extratropical Circulation. Part II: Trends. *Journal of Climate*, **13 (5)**, 1018–1036, doi:10.1175/1520-0442(2000)013⟨1018:AMITEC⟩2.0.CO;2.

Tisserand, F. F., 1891: *Traité de Mécanique Céleste*. Vol. ii ed., Gauthier-Villars, Paris.

Trenberth, K. E., G. W. Branstator, D. Karoly, A. Kumar, N.-C. Lau, and C. Ropelewski, 1998: Progress during TOGA in understanding and modeling global teleconnections associated with tropical sea surface temperatures. *Journal of Geophysical Research*, **103 (C7)**, 14 291–14 324, doi:10.1029/97JC01444.

Trenberth, K. E. and C. J. Guillemot, 1994: The total mass of the atmosphere. *Journal of Geophysical Research: Atmospheres*, **99 (D11)**, 23 079–23 088, doi:10.1029/94JD02043.

van Loon, H. and G. A. Meehl, 2011: The average influence of decadal solar forcing on the atmosphere in the South Pacific region. *Geophysical Research Letters*, **38 (12)**, L12 804, doi:10.1029/2011GL047794.

Vondrák, J. and B. Richter, 2004: International Earth Rotation and Reference Systems Service (IERS) web: www.iers.org. *Journal of Geodesy*, **77 (10-11)**, 585–678, doi:10.1007/s00190-003-0370-1.

Wahr, J. M., 1982: The effects of the atmosphere and oceans on the Earth's wobble ? I. Theory. *Geophysical Journal International*, **70 (2)**, 349–372, doi:10.1111/j.1365-246X.1982.tb04972.x.

Wahr, J. M., 1983: The effects of the atmosphere and oceans on the Earth's wobble and on the seasonal variations in the length of day - II. Results. *Geophysical Journal of the Royal Astronomical Society*, **74 (2)**, 451–487.

Wahr, J. M., M. Molenaar, and F. Bryan, 1998: Time variability of the Earth's gravity field: Hydrological and oceanic effects and their possible detection using GRACE. *Journal of Geophysical Research*, **103 (B12)**, 30 205–30 229, doi:10.1029/98JB02844.

Wallace, J. M., 2000: North atlantic oscillatiodannular mode: Two paradigms-one phenomenon. *Quarterly Journal of the Royal Meteorological Society*, **126 (564)**, 791–805, doi:10.1002/qj.49712656402.

Walter, C., 2008: Simulationen hydrologischer Massenvariationen und deren Einfluss auf die Erdrotation. Ph.D. thesis, TU Dresden.

Werth, S., 2010: Calibration of the global hydrological model WGHM with water mass variations from GRACE gravity data. Dissertation, Universität Potsdam, 139 pp.

White, W. B., J. Lean, D. R. Cayan, and M. D. Dettinger, 1997: Response of global upper ocean temperature to changing solar irradiance. *Journal of Geophysical Research*, **102 (C2)**, 3255–3266, doi:10.1029/96JC03549.

Wilson, C. R. and R. O. Vicente, 1990: Maximum likelihood estimates of polar motion parameters. *Variations in Earth Rotation*, AGU, Washington, DC, Geophys. Monogr. Ser., Vol. 59, 151–155, doi:10.1029/GM059p0151.

Wolff, J.-O., E. Maier-Reimer, and S. Legutke, 1997: Technical Report No . 13 The Hamburg Ocean Primitive Equation Model HOPE. Tech. Rep. 13.

Wolter, K. and M. S. Timlin, 1998: Measuring the strength of ENSO events: How does 1997/98 rank? *Weather*, **53 (9)**, 315–324.

Wunsch, C. and D. Stammer, 1997: Atmospheric loading and the oceanic "inverted barometer" effect. *Review of Geophysics*, **35 (1)**, 79–107, doi:10.1029/96RG03037.

Yoder, C. F., 1995: Astrometric and geodetic properties of Earth and the solar system. *Global Earth Physics: A Handbook of Physical Constants*, AGU, Washington, DC, AGU Ref. Shelf, Vol. 1, 1–31, doi:10.1029/RF001p0001.

Appendix

Variables and Geodetic Parameters

Table 7.1: Coordinates, Variables and Geophysical Parameters

Coordinates	
r	Positioning vector, for example function of ϕ, λ and height
ϕ	Latitude
λ	Longitude
t	Time

Variables	Description
$\chi(t)_i$	Excitation function, in mas ($i = [1, 2]$) and ms ($i = [3]$);
$\delta I(t)_{i3}$	Small variation of the tensor of inertia of the Earth, in $[kgm^2]$
$h(t)_i$	Changes in the relative angular momentum, in $[kgm^2/s]$
$W_i^I(\mathbf{r})$	Weighting function of the mass component
$W_i^u(\mathbf{r})$	Weighting function of the zonal motion component
$W_i^v(\mathbf{r})$	Weighting function of the meridional motion component
$M(\mathbf{r}, t)$	Mass component
$u(\mathbf{r}, t)$	Zonal velocity, positive towards the east
$v(\mathbf{r}, t)$	Meridional velocity, positive towards the north

Parameter	Value	Description
R	$6371.0km$	Mean Earth Radius
Ω	$7.292115 * 10^{-5} rad/s$	Mean Earth Angular Velocity
A	$8.0101 * 10^{37} kgm^2$	(1,1) Component Earth Inertia
C	$8.0365 * 10^{37} kgm^2$	(3,3) Component Earth Inertia
C_m	$9.1401 * 10^{36} kgm^2$	(3,3) Component Earth Mantle Inertia
α_1	1.610	all α_i describe rotational deformation,
α_2	0.684	loading and decoupling of the core.
α_3	1.125	The definition is given in Dobslaw et al. (2010)
α_4	0.750	and Gross (2007).

Computing the Earth Excitation in CESM

This section describes, which specific variables from the CESM output, are used in order to compute the excitation functions. In more detail, the description will focus on the modeled mass ($M(\mathbf{r},t)$) and motion ($u(\mathbf{r},t), v(\mathbf{r},t)$) components. Table 7.2 gives an overview of all relevant variables, followed by description of the actual computation process. For theoretical background see Chapter 2.

Table 7.2: CESM output variables as used for ERE computation.

ATMOSPHERE	
PS	Surface pressure
U,V	Wind components
hyai, hybi	Hybrid coefficient at layer interface

OCEAN	
RHO	Water density
SSH	Sea Surface Height
UVEL,VVEL	Current velocity along the curvilinear grid
ANGLET	Angle between curvilinear grid and spherical grid
TAREA	Area of a curvilinear grid cell
dz	Thickness of model layer

LAND	
SNOWICE	Snow in the form of ice
SNOWLIQ	Snow in the form of water
SOILICE	Ice water in soil
SOILLIQ	Liquid water in soil

AAM - Atmosphere Angular Momentum The pressure at the grid box interfaces p_i is computed using the surface pressure PS and hybrid coefficients at layer interface hyai and hybi according to $p_i = PS * hybi + 10e5 * hyai$. The mass of a grid box is the pressure difference between the top and bottom interface times the area of the grid box divided by the gravitational acceleration g.

The motion components are directly given as U and V in $[m/s]$ in spherical coordinates.

OAM - Ocean Angular Momentum The mass components are computed multiplying the density (RHO) of each grid cell times the thickness of grid cell layer (dz) times the area of the grid cell (TAREA). The height of the top grid layer dz(1) is adjusted with the Sea Surface Heights (SSH).

The motion components (UVEL, VVEL) are given tangential to curvilinear grid. Thus these components need to be rotated into spherical coordinates according to: $u =$

$UVEL \times \cos(ANGLET) - VVEL \times \sin(ANGLET)$ and $v = UVEL \times \sin(ANGLET) + VVEL \times \cos(ANGLET)$.

HAM - Hydrosphere Angular Momentum The continental mass is computed using the liquid (SOILLIQ) and the frozen (SOILICE) water content of the soil. Additionally prevailing surface masses in the form of snow (SNOWICE,SNOWLIQ) are considered.

The motion components are not computed, since they are found to be at least one magnitude smaller and thus are negligible (Dobslaw et al., 2010).

Abbreviations

Abbreviation	Description
AAM	Atmosphere Angular Momentum
AM	Annular Mode
AO	Arctic Oscillation
CAM	Community Atmosphere Model
CESM	Community Earth System Model
CCM	Chemistry-Climate Model
CCMVal	Chemistry-Climate Model Validation Activity
CLM	Community Land Model
CICE	Community Ice CodE
CMD	Composite Mean Differences
DKRZ	Deutsches KlimaRechenZentrum
ECMWF	European Centre for Medium-Range Weather Forecasts
ENSO	El Niño Southern Oscillation
ERA	ECMWF Reanalysis
ERE	Earth Rotational Excitation
EOF	Empirical Orthogonal Functions
EOP	Earth Orientation Parameter
GFZ	German Research Centre for Geosciences
GHG	Greenhouse Gas
GRACE	Gravity Recovery and Climate Experiment
hA, hO, hL	Motion component of the Atmosphere, Ocean and Land
HAM	Hydrospheric Angular Momentum
HOPE	Hamburg Ocean Primitive Equation model
IA, IO, IL	Mass component of the Atmosphere, Ocean and Land
ICRF	International Celestial Reference Frame
IPCC	Intergovernmental Panel on Climate Change
ITRF	International Terrestrial Reference System
ITRS	International Earth Rotation and Reference System Service
LOD	Length of Day
LSDM	Land Surface Discharge Model
MAI	Multi-Variate ENSO Index
MERRA	Modern Era Retrospective Analysis for Research and Applications
MLR	Multiple Linear Regression
MOZART	Model for Ozone and Related Chemical Tracers

MSLP	Mean Sea Level Pressure
NAM	Northern Annular Mode
NAO	North Atlantic Oscillation
NCAR	National Center for Atmospheric Research
NH	Northern Hemisphere
NP	North Pacific
OAM	Oceanic Angular Momentum
ODS	Ozone Depleting Substances
OGCM	Ocean General Circulation Model
OMCT	Ocean Model for Circulation and Tides
PC	Principal Component
PmE	Precipitation minus Evaporation
POP	Parallel Ocean Program
QBO	Quasi-Biennial Oscillation
RTM	River Transport Model
SAM	Southern Annular Mode
SC	Solar Cycle
SH	Southern Hemisphere
SPARC	Stratospheric Processes And their Role in Climate
SSH	Sea Surface Height
SST	Sea Surface Temperature
WACCM	Whole Atmosphere Community Climate Model
WSC	Wind Stress Curl

Acknowledgments

Ein besonderer Dank gilt meiner Familie, die mich in allen meiner Entscheidungen unterstützten. Insbesondere Anne stand mir stets mit viel Gefühl und noch mehr Geduld zur Seite. Ein großes Dankeschön geht an Maria, die meine Zeit am GFZ mit ihrer Gesellschaft, vielerlei Keksen und wunderbaren Aussichten bereichert hat. Maria war auch zu allen Tages- und Nachtzeiten bereit alle meine Textbausteine Korrektur zu lesen.

Katja Matthes gab mir die Möglichkeit im Rahmen der NATHAN Gruppe diese Arbeit anzufertigen. Für die Begutachtung, konstruktiver Kritik, sowie navigatorischer Unterstützung im wissenschaftlichen Kontext, möchte ich Ihr und Maik Thomas danken. Des Weiteren hat Henryk Dobslaw diese Arbeit mit vielen Hinweisen und fachspezifischen Diskussionen unterstützt.

Mein besonderer Dank gilt auch den anderen Mitgliedern der NATHAN Gruppe, allen voran Felicitas, die mir nicht nur fachlich hervorragend zur Seite stand, sondern es zusätzlich vermochte, meinen Blick mit einem Lächeln auf das Wesentliche zu lenken. Lisa, Christian, Wuke und Christofpher möchte ich für die vielen Diskussionen, Anregungen und Unterstützungen danken.

Bedanken möchte ich mich bei Julian Kuhlmann, für die angenehme Arbeitsatmosphäre, tatkräftige Unterstützung in allen Lagen und vor allem für die vielen Diskussionen über den Sinn und Unsinn vieler ausgesprochen sinnloser Sachen; die natürlich alle super wichtig sind!

Grüßen möchte ich an dieser Stelle alle Kollegen der Sektion 1.3; die aufgeschlossene und interessierte Atmosphäre, sowie die sehr unterhaltsamen Kaffeerunden haben zum hervorragenden Arbeitsklima beigetragen.

Ein besonderer Dank geht an Widynski & Roick, für eine Vielzahl an Herrausforderungen, die ganze Sektionen zusammenschweißen.

Selbständigkeitserklärung

Hiermit versichere ich, die vorliegende Arbeit ausschließlich unter Verwendung der angegebenen Quellen und Hilfsmittel, selbständig und ohne fremde Hilfe, ausschließlich für dieses Promotionsverfahren verfasst zu haben.

Berlin, 9. April 2013 Christof Petrick